Subsurface Damage Detection Using a Novel Fiber Optic Sensing Technique

by

Niell Elvin

Submitted to the Department of Civil and Environmental Engineering in partial fulfillment of the requirements for the degree of

Doctor of Philosophy
in
Intelligent Materials, Systems and Structures

at the

MASSACHUSETTS INSTITUTE OF TECHNOLOGY

September 1998

Author .....
Civil and Environmental Engineering
21 August 1998

Certified by .....
Christopher Leung
Associate Professor of Civil and Environmental Engineering
Thesis Supervisor

Accepted by .....
Joseph M. Sussman
Chairman, Departmental Committee on Graduate Studies

Subsurface Damage Detection Using a Novel Fiber Optic Sensing Technique

by

Niell G. Elvin

Submitted to the Department of Civil and Environmental Engineering on August 21, 1998, in partial fulfillment of the requirements for the degree of Doctor of Philosophy in Intelligent Materials, Systems and Structures

Abstract

The detection of subsurface damage is important in ensuring the safety and timely repair of structures. Existing methods for non-destructive evaluation of structural elements tend to be either expensive or unreliable for monitoring large scale systems. The novel fiber optic based technique developed in this research overcomes many of the limitations of traditional non-destructive evaluation methods by providing an interferometric sensing technique coupled with a simple mechanical test. The method is based on monitoring the phase change in an integral interferometric fiber optic sensor caused by moving a mechanical load over the damaged structure. The method has been shown to unambiguously detect both the position and size of damage. The theoretical and experimental validation of the proposed method is presented for the case of open cracks in which the faces are not allowed to come into contact. The effect of damage position and damage size on sensor performance for two typical structural elements is also presented. A closed loop fiber-optic interferometer with modulated load is shown to overcome the traditional problems of environmental drift such as material creep, temperature and ambient noise. This interferometric technique is also shown to be one of the few fiber-optic based techniques that have adequate sensitivity for integral damage detection.

Many traditional non-destructive evaluation methods tend to be insensitive in detecting closed cracks. Thus the closed crack problem represents a special challenge for structural damage monitoring. A fast iterative based boundary element method has been developed to solve this problem. This method is used to show the theoretical feasibility of detecting closed cracks with the developed novel sensing method.

Thesis Supervisor: Christopher Leung
Title: Associate Professor, Civil and Environmental Engineering

Acknowledgment

Many people have contributed to my PhD work during my stay at MIT. The guidance and encouragement provided by my advisor Professor Leung is greatly appreciated. The interesting and thoughtful discussions with Professor Ezekiel (who took the role of my acting advisor in Professor Leung's absence) is also greatly valued.

At an early stage in my research, the Quantum Optics and Photonics Group (past and present) took me in and helped me with the difficult experimental work, contributed thoughts, ideas and equipment - not to mention their great sense of humor which made many long days bearable. To everyone at the lab - thanks !

The financial support of the INEEL who sponsored this research is greatly appreciated.

TABLE OF CONTENTS

1. INTRODUCTION 9
- 1.1 Motivation 9
- 1.2 Outline of Thesis 10

2. EXISTING DAMAGE DETECTION METHODS 11
- 2.1 Introduction 11
- 2.2 Non-Fiber Optic Based NDE Techniques 11
- 2.3 Fiber Optic Based NDE Techniques 13
- 2.4 Modal Analysis NDE 14
- 2.5 A Note on Closed Crack NDE 14

3. INTERFEROMETRIC INTEGRATED STRAIN SENSING 17
- 3.1 The Description of the Technique 17
- 3.2 Interferometric Measurement 18
- 3.3 Measurement of Large Phase Changes 18
- 3.4 Measurement of Small Phase Changes 19
- 3.5 Open Loop and Closed Loop Operation 22
- 3.6 Photon-Shot Noise Resolution Limit 23
- 3.7 Opto-Mechanical Considerations 24
- 3.8 Some Practical Issues Concerning Ideal Sensor Performance 26
- 3.9 Possible Areas of Application 28

4. THE THEORETICAL FEASIBILITY OF OPEN CRACK DETECTION 29
- 4.1 Introduction 29
- 4.2 Theoretical Mechanical Considerations for Open Crack Detection 29
- 4.3 Sensor Performance for Undamaged Members 29
- 4.4 Open Crack Modeling Using the Finite Element Method 31
- 4.5 Results for Open Damage 35
- 4.6 Discussion of Results for Open Damage 44

5. THE THEORETICAL FEASIBILITY OF DETECTING CLOSED CRACKS 47
5.1 Introduction 47
5.2 Background to existing methods of solving crack closure problems 47
5.3 Theoretical Formulation 49
5.4 Some Practical Aspects of Using the Iterative Boundary Element Method 55
5.5 Example Problems 56
5.6 Discussion of the Iterative Boundary Element Method 63
5.7 Some Aspects of Sensing Closed Cracks 64
5.8 Results for Closed Crack Sensing 66
5.9 Effect of Crack Opening Mechanisms 71
5.10 Implication to Closed Damage Detection in Practice 75
5.11 Conclusions 76

6. EXPERIMENTAL VERIFICATION 77
6.1 Introduction 77
6.2 Detailed Experimental Layout Description 77
6.3 Sensor Output with Zero Applied Load 78
6.4 Load Application and Sensor Performance 80
6.5 Mechanical System Description 82
6.6 Experimental Results 84
6.7 Discussion on the Results for Open Damage 90

7. COMPARISON OF POINT SENSING VERSUS PROPOSED METHOD FOR DAMAGE DETECTION 91

8. PRACTICAL ASPECTS OF OPTICL FIBER, SUBSURFACE DAMAGE DETECTION 95
8.1 Parametric Study of Method Sensitivity 95
8.2 Mechanical Load Application 95
8.3 Conclusion 98

9. CONCLUSION AND SUMMARY 99
9.1 Summary 99
9.2 Original Contributions 99
9.3 Future Work 100

A. APPENDIX A 103
B. APPENDIX B 105
RERERENCES 107

Chapter 1

INTRODUCTION

1.1 Motivation

The accurate prediction of the size and location of damage in critical structural components is important in insuring their repair. The timely inspection and renovation of damaged structures has also long been known to prevent structural failure and the associated loss of life and property.

Though many non-destructive evaluation (NDE) techniques have been shown to work in a laboratory setting (Hung-1986, Kaczmarek - 1995, Lahiri et al.-1992, Zhang et al. - 1992) there are currently no effective NDE methods that are suitable for robust and rapid field test damage assessment. The failure of most techniques in the field is due largely to either (a) human error in applying or misinterpretation of the results, (b) the uncontrolled environment, (c) parts of the tested structure being inaccessible, and (d) the insensitivity of the NDE method to the type of damage being assessed. Moreover, many of the existing techniques are labor intensive, expensive and time consuming.

The detection of damage is especially critical in lightweight composites such as those used in military and aerospace applications due to a myriad of reasons including, (a) for performance considerations, strength safety factors in aerospace composites tend to be less conservative, making these structures more prone to damage that may lead to final failure, (b) extensive use of advanced composite materials is relatively recent and an experience database on the initiation and growth of damage still needs to be established, (c) final failure of composite systems is typically caused by the interactions of many different modes of damage - the evolution of damage that causes final failure is not well understood.

NDE of other structures in civil engineering works such as bridges and dams has also recently become a topical issue due to the expense and the unreliable nature of existing inspection methods. Currently it is estimated that (a) 182,000 out of 576,000 bridges in the US are deficient (Livingston, 1998), (b) 130 000 km out of 6.3 million km or roadway is badly in need of repair (Livingston, 1998), and (c) 2100 out of 75 000 dams are considered unsafe (ASCE key alert - 1997). The need for inexpensive and reliable assessment of the integrity of these structures has become a key priority for the improved service life of current and future structures.

This thesis deals specifically with the detection of subsurface damage, that is damage that is not visible from the surface of the structure and thus needs special NDE techniques. The detection of subsurface damage is especially critical in many structural applications, including but not limited to (a) impact induced delamination damage in advanced compos-

ite structures, (2) reinforcement corrosion induced spalling in concrete structures, and (3) fretting fatigue and spalling under riding surfaces. The fatigue growth of subsurface damage can finally lead to failure of the structural component and thus has been the focus of many NDE techniques as is discussed in Chapter 2

1.2 Outline of Thesis

The detection of subsurface damage using a novel fiber-optic based sensing technique will be presented in this thesis. Chapter 2 presents a general overview of existing NDE techniques, including non-fiber optic based and fiber optic based techniques. Chapter 3 discusses the background to the proposed method, including a detailed over-view of integrated strain measurement using a fiber-optic interferometric technique. Chapter 4 concentrates on proving the theoretical feasibility of using this novel method for detecting open damage zones (i.e. damage zones in which the faces of the crack are not allowed to come into contact with each other). Chapter 5 presents a newly developed boundary element method for the rapid solution of closed crack problems. Chapter 5 also discusses the theoretical feasibility of using the novel fiber optic sensing method for assessment of closed damage. Chapter 6 presents the detailed experimental layout of the optical and mechanical systems, and compares the experimental results with the theoretical results for two structures (a) a simply supported beam, and (b) a beam on elastic foundation. Chapter 7 compares the novel technique with traditional point sensing techniques and highlights some of the advantages of the new method. Chapter 8 discusses some of the practical issues related to subsurface fiber-optic damage detection. Chapter 9 highlights the key findings and contributions of the thesis and provides some recommendations for future research.

Chapter 2

EXISTING SUBSURFACE DAMAGE DETECTION METHODS

2.1 Introduction

This chapter discusses some of the existing Non-Destructive Evaluation (NDE) techniques for subsurface damage detection. Although a myriad of NDE methods exist, and a detailed discussion of all the techniques is beyond the scope of this thesis, a brief discussion of the most commonly used NDE techniques will be presented in this section. This chapter is divided into 3 sections. Section 2.2 deals with non-fiber optic based techniques. Section 2.3 deals with fiber-optic based techniques. Section 2.4 deals with damage detection techniques based on modal analysis. The relative advantages and disadvantages of the various techniques will also be discussed.

2.2 Non-Fiber Optic Based NDE Techniques

This section discusses some of the more popular non-fiber optic based NDE techniques for subsurface damage detection, including (a) ultrasonic techniques, (b) radiographic methods, (c) thermography and (d) holographic techniques. Although many other NDE techniques exist such as eddy current techniques and magnetic flux leakage techniques, these NDE methods tend to be specific to particular materials (such as electrically conductive materials or ferromagnetic materials) and since they do not provide a generally applicable method, they will not be discussed in this thesis.

2.2.1 *Ultrasonic Techniques*

Ultrasonic NDE methods are the most commonly used NDE methods for evaluating subsurface damage (Bray and Stanley, 1997). The two most common ultrasonic methods are the "through-transmission method" and the "impact-echo" method. In the through transmission method, a transducer generates a pulsed ultrasonic wave on one side of the tested structure. The time of flight to reach a receiver on the opposite side of the structure is then recorded. Knowing the distance between the transducer and the receiver, the wave speed can be calculated. The integrity of the structure can then be inferred from the wave speed. In the impact-echo method, the ultrasonic transducer and receiver are placed on the same side of the structure. The time of flight for a pulse to travel from the transmitter to the damage and back to the receiver is measured. Knowing the wave speed through the material allows one to calculate the depth of the damage.

The advantages of the ultrasonic method include (a) the ability to detect various damage modes, (b) good spatial resolution, and (c) the availability of an existing knowledge base. Some of the disadvantages include (a) the depth of penetration of the acoustic signal which limits the measurement depth (Cawley and Alleyne, 1996), (b) labor intensive

manipulation of the transducer and receiver (Bray and Stanley, 1997), and (c) the need for an effective ultrasonic coupling method between the probes and the host structure (Bray and Stanley, 1997).

2.2.2 *Radiographic Methods*

In the radiographic NDE method, the inspected structure is placed between an energy source (x-ray, γ-ray, neutrons or protons) and a recording plane. Once the energy from the source has passed through the structure, the image generated on the recording plane is then used to evaluate the integrity of the structure.

The advantages of radiographic methods include (a) visual recording of the damage provides easy interpretation of the damage state, (b) a vast amount of data exists for these methods of inspecting materials, and (c) specialized techniques such as computer tomography can provide more accurate assessment of the state of damage in the structure. The major disadvantages of radiographic techniques include (a) expense of the technique and (b) safety concerns in using high level radiation, and (c) difficulty in locating planar defects (Lahiri et al., 1992).

2.2.3 *Thermographic Techniques*

In the thermographic technique, the thermal changes due to a temperature load on the surface of the material are monitored with an infra-red (IR) detector. After the thermal load is applied, the IR detector can infer regions of damage in the structure due to the presence of hot or cold spots on the surface of the material. The advantages of thermographic NDE include (a) its ability to inspect large areas of the structure, and (b) relatively cheap equipment costs. Disadvantages of this technique include (a) insensitivity to defects far from the surface, and (b) difficulty in interpreting the results because of the complex interaction of the thermal loads and the host structure. (See for example Zhang and Sandor, 1992 for an overview of thermographic NDE techniques)

2.2.4 *Holographic Techniques*

Holography is a wave recording and reconstruction technique based on the recording of interference fringe patterns which result from a coherent superposition of the waves scattered off the object's surface. The most commonly used holographic NDE method consists of a double exposure method. The first exposure is of the tested material in the undeformed state and the second exposure is of the material in the deformed state. The resulting hologram is then a displacement field map of the tested material. The extent and position of the damage can then be inferred from the displacement perturbation around the damaged zone. Though the two-exposure holographic technique is not suitable for field NDE of structures because of its sensitivity to structural changes (such as vibration) between exposures, methods to overcome this problem are currently being investigated (Vest, 1986). The advantages of holographic techniques include (a) it is a non-contact method, and (b) it is highly sensitive. The disadvantages of the techniques include (a) its sensitivity to environmental vibration and (b) its depth penetration (i.e. defects far from the surface are not easily detectable). (See Hung, 1986 for a general overview of holographic NDE methods.)

2.3 Fiber Optic Based NDE Techniques

Fiber optic based damage detection techniques provide some clear advantages over traditional NDE techniques. These advantages include their immunity to electromagnetic interference, high sensitivity, continuous monitoring ability and low-cost. Another advantage of fiber optic sensors is the relative ease in which they can be embedded into curing materials such as concrete and advanced composites which makes them ideal for integrity monitoring of many civil and aerospace structures. Fiber optic damage detection sensors can be broadly divided into two categories (1) point sensors, and (b) integrated or distributed sensors. For a general overview of fiber-optic sensors, the interested reader is referred to Udd, 1992).

2.3.1 *Point Sensors*

Point sensing damage detection methods are currently the most commonly used fiber-optic based damage detection method. They rely on the detection of the local strain perturbations caused by the damage. The two most commonly used fiber-optic point sensing methods are (a) Bragg grating sensors, and (b) Fabry-Perot sensors.

The Bragg grating is a segment of the optical fiber with a half wavelength ($\lambda_o/2$) of light periodic variation in the refractive index of the core. When a wide frequency band light source passes through the Bragg grating, the light is reflected back off each successive refractive index change. Due to the half wavelength of light spacing of the grating, the successive reflections off each index change can constructively interfere which causes a very narrowband light source (with wavelength λ_o) known as the Bragg wavelength to be reflected. When strain is applied to the Bragg grating the period of the spacing changes which can be inferred from the change in reflected light's wavelength. The advantages of the Bragg grating sensor include (a) closely controlled automated fabrication, (b) sensitivity, and (c) multiplexing ability i.e. more than one Bragg grating sensor can be placed along the same optical fiber. Disadvantages of the Bragg grating sensor include (a) limited multiplexing (currently a maximum of 64 Bragg gratings can be placed on one fiber), (b) the need for relatively expensive measurement equipment. (A more detailed discussion of Bragg-grating sensors is given by Frieble, 1998)

The Fabry-Perot interferometer consists of two fibers separated by an air gap inside a hollow tube. The two ends of the fiber forming the air-gap are reflectively coated to create an optical cavity which can support an integral number of half light-wavelengths. Under applied strain the air-gap undergoes a length change which causes a shift in the resonance of the cavity. The state of the strain can then be inferred from the change in the length of the air-gap. The advantage of the Fabry-Perot sensor include (a) high sensitivity, (b) sensitivity only to axial strain, and (c) ability for multiplexing. The disadvantages are similar to the Bragg grating sensor.

In general the major problem with all point-sensing damage detection methods is that the strain perturbation caused be damage is localized around the vicinity of the crack. Thus in order for point-sensing to be effective the sensor has to be placed in the strain perturbation region. Since typically the position of the damage is not known *a priori* a vast network of point sensors is needed to detect the damage zone. At present the number of

sensors required to effectively monitor large structures makes the point sensing method impractical.

2.3.2 *Distributed Fiber Optic Sensors*

Distributed fiber optic sensing has the potential to overcome the need of knowing the position of the damage *a priori* by allowing for strain sensing anywhere along the optical fiber. In general distributed sensing relies on sending a high intensity light pulse down the fiber and continuously monitoring a backscattering phenomena (for example Rayleigh scattering or Brillouin scattering, see LeCoeche et al., 1998 for an overview of distributed structural sensing). An applied strain perturbation in the fiber caused by the damage leads to a localized refractive index change in the fiber due to the photo-elastic effect. Due to the strain induced change in refractive index, a portion of the light is reflected which changes the magnitude of the backscattered light. Measuring the time of flight of the laser pulse allows for the determination of the damage position. The problems with distributed fiber optic sensing systems include (a) their spatial resolution depends on the width of the applied pulse and speed of the measuring equipment, (2) the perturbations to the backscattered light tends to be small and thus the method is insensitive to the small strain perturbations caused by damage (Udd, 1992) and (3) the methods tend to be highly experimental and require potentially expensive equipment.

2.4 Modal Analysis NDE

Modal NDE relies on inferring the state of damage in a structure from the change in either (a) the structural natural frequencies, (b) the mode shapes, (c) the damping or (d) a combination of all three. Damage in part of a structure will in general reduce the local stiffness of the host material and thereby change the natural frequency and modal shape of the structure. The advantage of this method is that potentially only a few sensing points are needed to accurately assess the state of damage in the whole structure. The problems with this method include (a) the method is unreliable, since small changes in the structure can cause relatively large changes in dynamic behavior, and (b) the method relies on the solution of a complex inverse dynamic problem which makes real time assessment of structures difficult.

2.5 A Note on Closed Crack NDE

Cracks in which the faces are in contact provide a special problem for NDE. All the above mentioned techniques require significant modifications and extra sophistication in order to reliably locate this type of damage. In the ultrasonic method, there is no unique protocol for evaluating closed cracks, some option could include (a) selecting an ultrasonic frequency sensitive to closed cracks (Kundu *et al.* 1997), (b) position the transducer and receiver at various angles to the damage (Saka and Abe, 1994), and (c) generating various acoustic propagation modes such as Love waves (Kundu *et al.* 1997). Radiographic methods are very insensitive to planar closed defects and exposures at various angles are needed in order to get any indications of closed damage. At present there is no thermographic methods for closed crack detection since heat conduction through the faces of the closed crack are almost unperturbed, and thus do not significantly effect the thermal map

on the structures surface. The strain sensing techniques (holographic and existing fiber-optic sensors) tend to be insensitive to closed cracks since the stress perturbations due to closed cracks are significantly smaller than for open damage.

Chapter 3

INTERFEROMETRIC INTEGRATED STRAIN SENSING

3.1 The Description of the Technique

A schematic of the proposed fiber-optic damage detection scheme is shown in Figure 3.1. Light from a laser is coupled into a single mode optical fiber and is then divided into 2 single mode fibers by a 2x2, 50-50 fiber coupler. The first fiber which is not strained is called the reference fiber. The second fiber, which is attached (either embedded or surface mounted) to the structural member is called the sensing fiber. The light waves from the reference and sensing arms are allowed to recombine at the output fiber coupler and the interference between the two arms of the sensor is monitored with a light detector. In this section, ideal interference is assumed, that is (i) the polarization of the emerging beams are assumed to be the same, and (ii) the interferometer arms are assumed to be within the coherence length of the laser. Polarization and coherence length issues will be discussed in Section 3.7.

The intensity of the interference pattern between the two light waves is given by the superposition of the individual waves. The presence of integrated strain in the sensing fiber causes the sensing fiber to increase its optical length by ΔL. The optical length being equal to nL_o where n is the refractive index of the material through which the light is travelling and L_o is the geometric length of the fiber. The change in optical path length causes a phase shift ($\Delta\phi$) given by

$$\Delta\phi = \frac{2\pi\Delta L}{\lambda} \tag{3.1}$$

where λ is the wavelength of the laser light.

The sensing scheme consists of moving a prescribed load along the length of the member. The position and location of the damage can be determined by comparing the phase shift ($\Delta\phi$) versus load position between the damaged and undamaged (virgin) states.

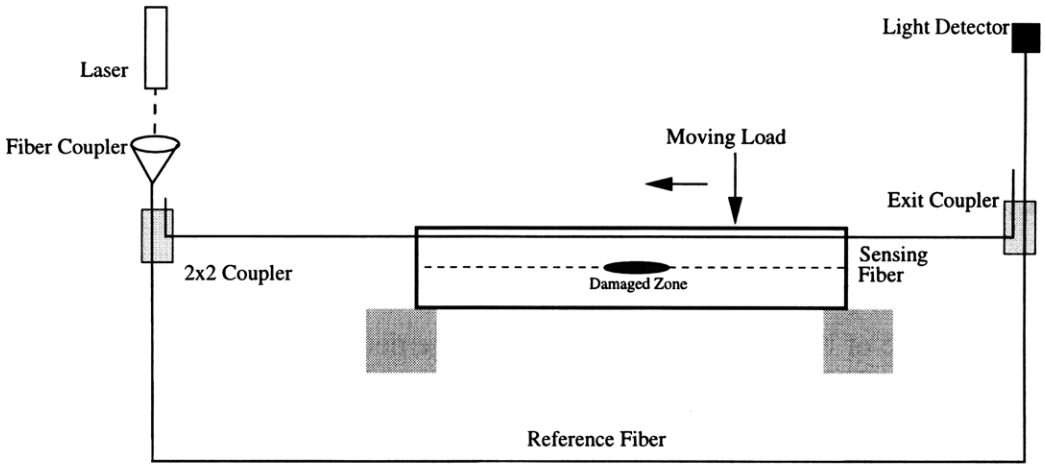

Figure 3.1: Schematic Mach-Zender interferometer attached to a damaged structural component and subjected to a moving point load

3.2 Interferometric Measurement

The intensity of the light at the photo-detector is given by the interference of the beams in the reference and sensing arm of the interferometer. This intensity is given by

$$I = (I_1 + I_2) + 2\sqrt{I_1 I_2}\cos\Delta\phi \tag{3.2}$$

where I_1 is the intensity of the light in the reference arm and I_2 is the intensity of the light in the sensing arm of the interferometer. Figure 3.2 shows the change of intensity (I) measured at the detector versus the phase change $\Delta\phi$ (assuming I_1=I_2).

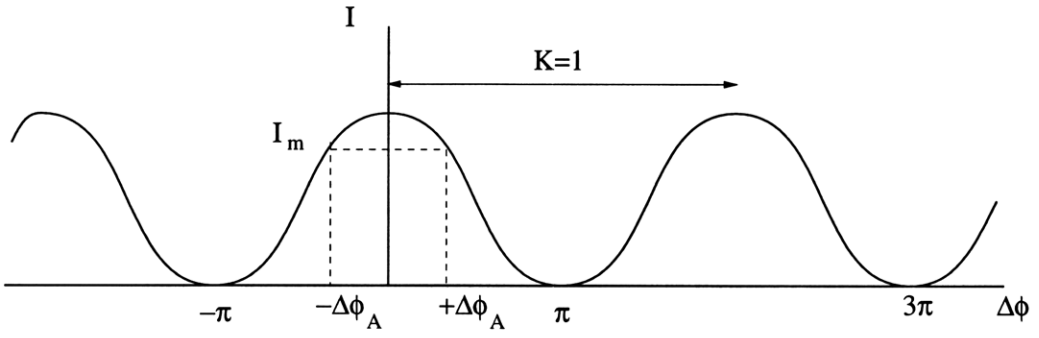

Figure 3.2: Plot of detector output versus $\Delta\phi$

3.3 Measurement of Large Phase Changes

For large changes in $\Delta\phi$, the optical path change between the two arms of the interferometer can be calculated by counting the number of fringes (K in Figure 3.2) seen by the detector. Fringe counting is typically done by counting the number of zero crossings seen by the detector. It must be noted that the fringe counting method can only be effectively used to find displacements within a half fringe resolution and thus this method is typically only used for measuring the phase change for a relatively large number of fringes. The

number of fringes counted is dependent on the dynamic range of the fringe counting circuit. Figure 3.2 also shows that in this interferometric technique the same measured interferometric output (I_m) is given for both a positive and negative applied phase change ($\Delta\phi_A$). Special modifications to this interferometric technique are needed in order the determine the direction of the phase change.

3.4 Measurement of Small Phase Changes

As will be shown in this thesis, the integrated strain sensing of damage requires the measurement of phase changes within a fraction of a fringe. This section describes some interferometric techniques which are able to measure small phase changes. Other sensitive interferometric techniques which are not discussed here can also be used to make measurements within a fraction of a fringe (see for example Jackson, 1985). Figure 3.2 shows that the sensitivity of phase change measurements is dependent on the slope of the phase-change versus intensity plot. In order to obtain the maximum sensitivity, a $\pi/2$ bias, corresponding to the maximum slope needs to be applied to the interferometer as shown in Figure 3.3 (a) (assuming that $\Delta\phi=0$ corresponds to a constructive interference peak). Another advantage of the biasing technique is that for measurements less than a quarter fringe, the direction of the phase change can also be measured. The disadvantage of this method is that measurement errors can occur depending on the stability of the bias and on the intensity fluctuations of the laser (unless an independent measurement of the laser intensity is made). A way of overcoming the intensity fluctuations problem is to symmetrically straddle the fringe (at $\pm\pi/2$) using two detectors as shown in Figure 3.3 (b). The signals of the two detectors are subtracted from each other and is equal to the phase change in the interferometer. Another advantage of the fringe straddling scheme shown in Figure 3.3 (b) is that the sensitivity of the sensing scheme is double that of the single sided biasing scheme shown in Figure 3.3 (a). It must be noted that, in the straddling scheme, intensity fluctuations do not affect the sensor output only if the two detectors are kept at symmetrical positions about a fringe, and thus the physical positions of the two detectors relative to the fringe must be carefully controlled.

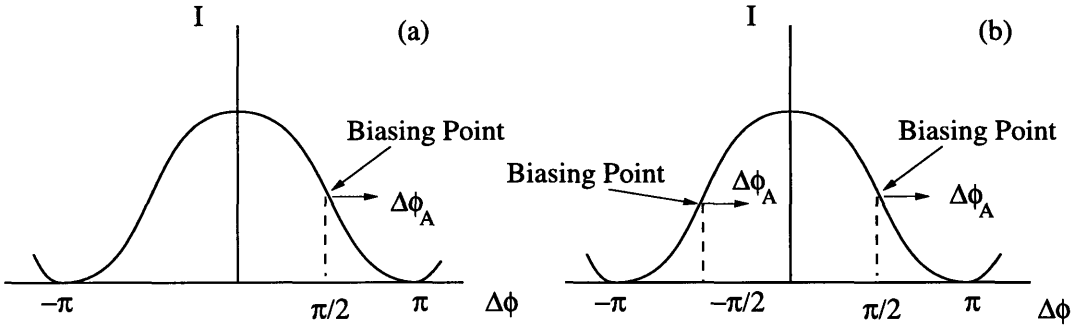

Figure 3.3: Methods of interferometer biasing

A way of overcoming the laser fluctuation disadvantage for biased interferometric schemes is by applying an A.C. phase modulation with amplitude $\Delta\phi_m = \pm\pi/2$ and frequency ω_m around $\Delta\phi=0$ to either the sensing or reference arm as shown in Figure 3.4.

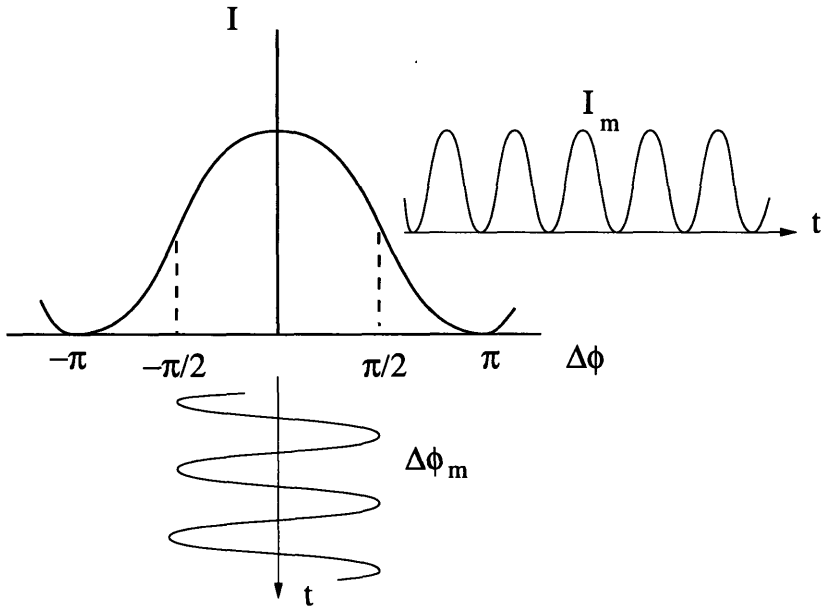

Figure 3.4: A.C. interferometric modulation and no applied phase change ($\Delta\phi$=0)

Figure 3.4 shows that for a modulation frequency of ω_m and with no applied phase change, ($\Delta\phi$=0), the frequency of the light intensity measured by the detector is doubled i.e. $2\omega_m$. Figure 3.5 shows the modulated interferometer output with an applied phase change.

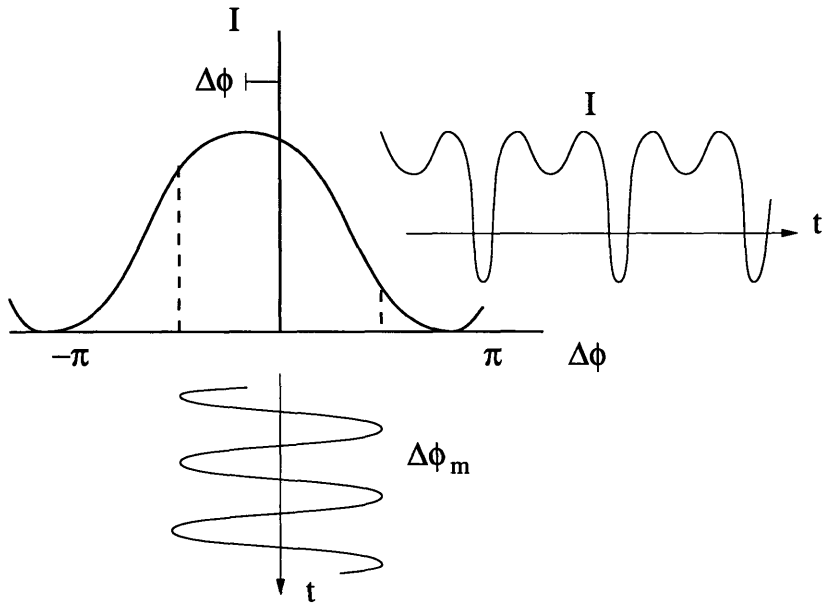

Figure 3.5: A.C. interferometric modulation with constant applied phase change

The intensity incident on the detector then becomes amplitude modulated. The intensity at the photodetector is given by:

$$I = (I_1 + I_2) + 2\sqrt{I_1 I_2}\cos(C\sin\omega_m t + \Delta\phi) \tag{3.3}$$

where C is the amplitude of the applied modulation, $\Delta\phi$ is the applied phase change due to integrated strain. Expanding Equation 3.3 in terms of Bessel functions produces (Arfken, 1985),

$$I = (I_1 + I_2) + 2\sqrt{I_1 I_2}\left(\left[J_0(C)\cos\Delta\varphi + 2\sum_{n=1}^{\infty} J_{2n}(C)\cos\Delta\phi\ \cos 2n\omega t\right] - \ \ldots \right. \tag{3.4}$$
$$\left.\left[2\sum_{n=1}^{\infty} J_{2n-1}(C)\sin\Delta\phi\ \sin(2n-1)\omega t\right]\right)$$

The component of the detected intensity at the modulation frequency is

$$I_\omega = -2(2\sqrt{I_1 I_2})J_1(C)\sin\Delta\phi\ \sin\omega t \tag{3.5}$$

Demodulating (which consists of multiplying Equation 3.5 by $\sin\omega_m t$ (after phase correction of the reference modulation) and considering only the DC component) gives

$$I_d = -2(2\sqrt{I_1 I_2})J_1(C)\sin\Delta\phi \tag{3.6}$$

Equation 3.6 shows that the demodulated intensity is zero for $\Delta\phi=0$, positive for $\Delta\phi < 0$ and negative for $\Delta\phi > 0$. The sensor output is shown in Figure 3.6.

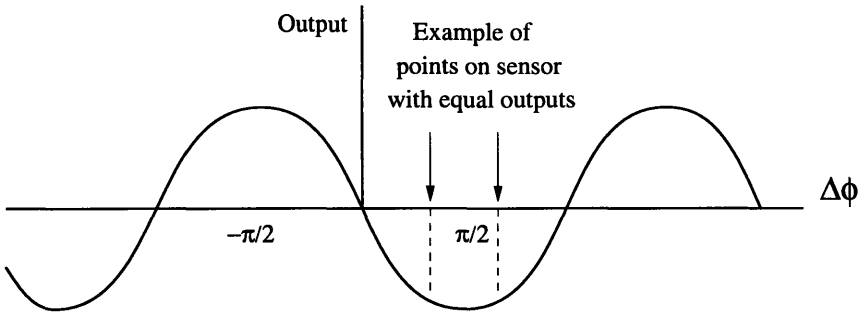

Figure 3.6: Output for A.C. modulated interferometer

Figure 3.6 shows that the sensor output is non-linear and that for measurements greater than $\Delta\phi=\pi/2$, the direction of phase change measured by the sensor cannot be determined since positive and negative phase changes produce the same detector output. The main advantages of the modulation method are that since the $\Delta\phi=0$ point is used, there is no need for external offset (provided that pure A.C. modulation is used) and that if a sufficiently high modulation frequency is used, the sensitivity of the interferometer can be reduced to the fundamental shot-noise limit (provided that $\Delta\phi$ is kept at zero)

. Figure 3.7 shows a schematic plot of a typical noise spectrum of a laser. The noise spectrum plot shows the so called '1/f' noise component at low frequencies and the shot noise limited region at high frequencies which is associated with the random fluctuations of photons. The range of frequencies at which the laser-noise is dominated by shot-noise depends on the source but is typically greater than a few kilohertz. The applied modulation

frequency is thus chosen so that the measurement is dominated by photon shot-noise. See for example Ezekiel, 1992 for a more detailed explanation of the shot noise phenomena.

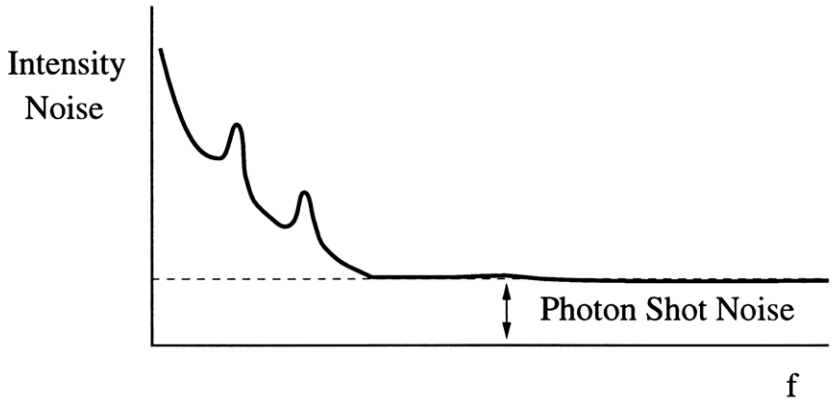

Figure 3.7: Typical laser intensity noise spectrum

3.5 Open Loop and Closed Loop Operation

An open loop modulated interferometric sensor is shown in Figure 3.8. An A.C. bias driven at ω_m is applied to the reference arm of the interferometer. The detector output is then demodulated at ω_m. After demodulation and low pass filtering, the sensor output versus displacement is sinusoidal as shown in Figure 3.6.

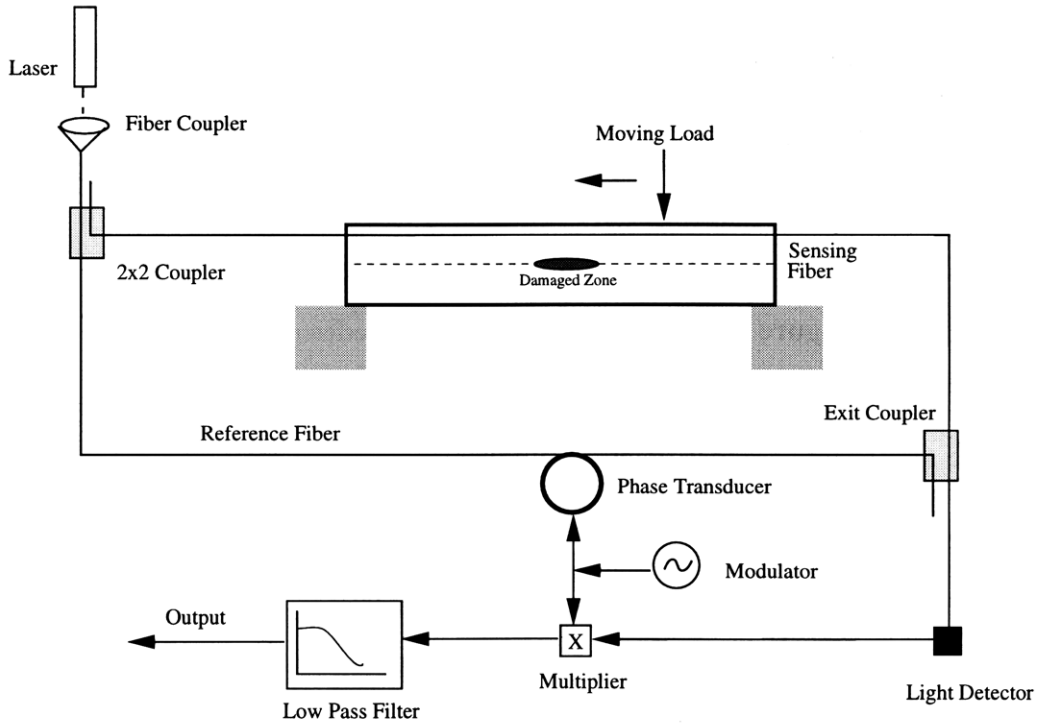

Figure 3.8: Schematic of open loop operation

The main disadvantages of the open loop system are that (a) the sensor demodulator output is dependent on the gains of the various amplifiers and thus needs to be calibrated, and (2) the demodulator output is non-linear with $\Delta\phi$. In the closed loop system, the output of the demodulator is fed into the servo amplifier which drives a phase transducer as shown in Figure 3.9. The servo keeps the demodulator output at zero for any applied phase change in the interferometer by applying exactly the negative phase change to the phase transducer. The advantages of the closed loop sensor are that (a) provided a very high open loop gain is maintained, the output of the sensor is independent of the gains of the individual components, and (b) the output linearity and stability is only dependent on the linearity and stability of the phase transducer.

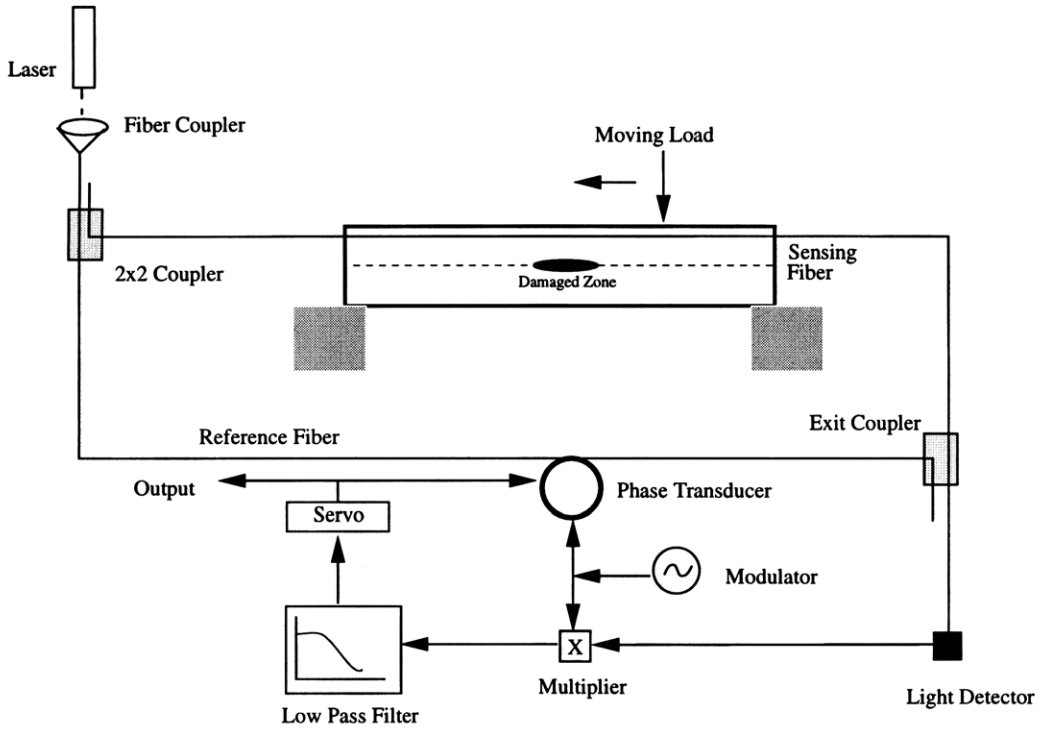

Figure 3.9: Schematic of closed loop operation

3.6 Photon-Shot Noise Resolution Limit

In order to explain the shot noise resolution limit, consider an interferometer with a D.C. bias as shown in Figure 3.3 (a). For maximum sensitivity, the bias point is chosen to be at the point of maximum fringe slope i.e at $\pi/2$. Any intensity fluctuations of the laser can appear to be changes in phase and cannot be distinguished from the phase change due to integral strain. Although there are ways to overcome this noise by the A.C. modulation method discussed in the previous section, it is not possible to overcome the effect of photon shot noise because it is a random process (Yariv, 1976). Thus, the fundamental uncertainty of interferometric sensing is limited by photon shot noise $\delta(\Delta\phi)$. This uncertaintity is given by:

$$\delta(\Delta\phi) = \frac{\text{photon shot noise}}{\text{maximum fringe slope}} \tag{3.7}$$

which is a minimum when the fringe slope is a maximum. The average light power at the detector can be related to the number of photons by Planck's law

$$P = n_p hf \tag{3.8}$$

where n_p is the number of photons falling on the detector per second, $h = 6.6266\text{x}10^{-34}$ J.s is Planck's constant and f is the frequency of light. The average number of photoelectrons coming from the detector ($\bar{N}$) is then given by

$$\bar{N} = n_p \eta_d \tau \tag{3.9}$$

where η_d is the quantum efficiency of the detector and τ is the averaging time (which is the time over which averaging occurs and is related to the bandwidth as $1/2\tau$). Assuming a Poisson arrival of photons at the detector, the standard deviation of the number of photoelectrons incident at the detector is

$$\sigma = \sqrt{\bar{N}} \tag{3.10}$$

The root mean square of the phase noise which is assumed to be equal to the phase change uncertainty, is then given by (Ezekiel and Arditty, 1982)

$$\delta(\Delta\phi) \approx \frac{\frac{\sigma}{\bar{N}}}{\text{Fringe Slope}} = \frac{1}{\frac{1}{\pi}\sqrt{\bar{N}}} = \frac{\pi}{\sqrt{n_p \eta_d \tau}} \tag{3.11}$$

Equation 3.11 shows that the critical factor in determining the shot-noise limit of the sensor are (1) the averaging time (τ) and (2) the laser power. Since the shot noise is assumed to be random with zero mean intensity, the longer one is able to average this intensity noise, the smaller will be the uncertaintity in the measurement. For demonstration, the maximum sensitivity can be computed for an interferometer with $\lambda = 632$ nm, $n_p = 3\text{x}10^{15}$ photons/sec corresponding to 1mW of power on the detector, $\eta_d = 0.3$, $\tau = 1/20$ second (corresponding to 40 Hz bandwidth). These values give $\delta(\Delta\phi) \approx 5\times10^{-7}$ rad which is the shot noise resolution limit of the interferometer. This number is approximately the same as calculated by Jackson (1985) who gives $\delta(\Delta\phi) \approx 1\times10^{-6}$ rad for a 600 nm light source.

3.7 Opto-Mechanical Considerations

The phase shift caused by the optical path length change along the sensing fiber is related to the axial strain in the sensing fiber. Consider a differential length of an interferometric sensor *ds* undergoing a state of triaxial strain (ε_{xx}, ε_{yy} and ε_{zz}) as shown in Figure 3.2

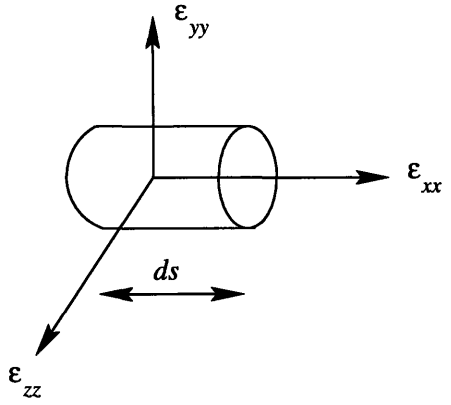

Figure 3.10: A differential fiber segment subjected to a state of triaxial strain

The optical path length change (ΔL) in the fiber is then given by

$$\Delta L = n(1 + \varepsilon_{xx}) \tag{3.12}$$

where n is the refractive index change of the deformed fiber and ε_{xx} is the axial strain in the fiber.The state of stress in the fiber introduces birefringence in the glass which changes the refractive index (n) in the fiber. The refractive index change (Δn) due to the optical-mechanical coupling is given by the average refractive index change in the y and z plane (Sirkis and Haslach, 1990)

$$\Delta\left(\frac{1}{n^2}\right) = \frac{1}{2}\Delta\left(\frac{1}{n_y^2}\right) + \frac{1}{2}\Delta\left(\frac{1}{n_x^2}\right) = P_{12}\varepsilon_{xx} + \frac{(P_{11} + P_{12})}{2}(\varepsilon_{yy} + \varepsilon_{zz}) \tag{3.13}$$

where $\Delta(1/n^2)=(1/n^2)-(1/n_o^2)$, P_{12} and P_{11} are Pockels' optical strain constants of the fiber , and ε_{yy} , ε_{zz} are the transverse normal strains in the fiber. Hence equation 3.3 yields,

$$n = \frac{n_o}{\sqrt{1 + n_o^2\left[P_{12}\varepsilon_{xx} + \frac{(P_{11} + P_{12})}{2}(\varepsilon_{yy} + \varepsilon_{zz})\right]}} \tag{3.14}$$

For small strains, equation 3.4 can be written in its first order Taylor series approximation as:

$$n = n_o\left(1 - \frac{1}{4}n_o^2[2P_{12}\varepsilon_{xx} + (P_{11} + P_{12})(\varepsilon_{yy} + \varepsilon_{zz})]\right) \tag{3.15}$$

Substituting equation 3.5 into 3.1 and 3.2 and neglecting all second order strain terms gives:

$$d\phi = \frac{2\pi n_o}{\lambda} ds\left[1 + \varepsilon_{xx} - \frac{1}{4}n_o^2[2P_{12}\varepsilon_{xx} + (P_{11} + P_{12})(\varepsilon_{yy} + \varepsilon_{zz})]\right] \tag{3.16}$$

The phase change ($d\Delta\phi$) between the reference and the unstrained sensing arm is:

$$d\Delta\phi = \frac{2\pi n_o}{\lambda} ds\left[\varepsilon_{xx} - \frac{1}{4} n_o^2 [2P_{12}\varepsilon_{xx} + (P_{11} + P_{12})(\varepsilon_{yy} + \varepsilon_{zz})]\right] \tag{3.17}$$

Integration of equation 3.17 with respect to ds then yields

$$\Delta\phi = \frac{2\pi n_o}{\lambda} \int_0^L \left(\varepsilon_{xx} - \frac{1}{4} n_o^2 [2P_{12}\varepsilon_{xx} + (P_{11} + P_{12})(\varepsilon_{yy} + \varepsilon_{zz})]\right) ds \tag{3.18}$$

which is the relationship derived by Sirkis and Haslach (1991). Sirkis and Haslach (1990) also showed that for a surface mounted fiber that does not significantly stiffen the host structure, the shear and transverse stresses are negligible and the fiber undergoes only axial stress. It can be shown from simple elasticity theory that since the fiber is only undergoing axial stress, the transverse strains (ε_{yy} and ε_{zz}) are equal to $-\nu\varepsilon_{xx}$ (ν being the Poisson's ratio of the fiber). Under these assumptions, and assuming that the sensing and reference arms of the Mach-Zender interferometer are of equal length, equation 3.18 can then be reduced to:

$$\Delta\phi = \frac{2\pi n_o}{\lambda}\left[1 - \frac{n_o^2}{2}\{P_{12} - \upsilon_f(P_{11} + P_{12})\}\right]\left(\int_0^L \varepsilon_{xx} ds\right) \tag{3.19}$$

which is the same as given by Sirkis and Haslach (1990). Equation 3.19 can be rewritten as

$$\Delta\phi = \frac{2\pi n_o}{\lambda}[1 - c_o]\left(\int_0^L \varepsilon_{xx} ds\right) \tag{3.20}$$

Since the terms in front of the integral sign are constants for any optical fiber and wavelength, the phase change, $\Delta\phi$ is proportional to the integral of the axial strain ($\int\varepsilon_{xx}$).

3.8 Some Practical Issues Concerning Ideal Sensor Performance

This section details some of the issues that are of practical importance when dealing with integral strain sensing interferometric performance. These issues include the characteristics of the (a) laser light source, (b) the optical fiber, (c) the servo, and (d) the phase transducer.

3.8.1 *The Laser Light Source*

The major issues of the light source are (a) the coherence length and (b) the intensity of the light.

The coherence length of the light depends on the frequency spread of the light source and affects the maximum allowable optical path length difference between the sensing and reference arm of the sensor. In general the maximum coherence length (L) is given by (see for example Fowles, 1975 for further explanation of this coherence length equation)

$$L \sim \frac{c}{\Delta f} \tag{3.21}$$

where c is the speed of light and Δf is the spectral width of the light source. For example in a typical He-Ne laser, regardless of the number of laser longitudinal modes, the largest spectral width of the source cannot be greater than the spectral width of the laser amplifier. For a He-Ne laser the spectral width of the amplifier is about 1.5 GHz which gives a coherence length of L~20 cm. Under certain circumstances it might not be possible to achieve the required precision to keep the reference and sensing arms within the coherence length of the laser. Readily available single frequency lasers may then be used to decrease the spectral width of the laser. Coherence lengths of 300 km have been achieved for single frequency He-Ne laser (Cook, 1971).

Adequate laser power is needed in order to achieve small photon shot noise as shown in Section 3.6.

3.8.2 *Fiber Type*

The most important considerations in selecting an optical fiber for interferometric measurements are (a) single mode operation, (b) birefringence, and (c) loss.

Single mode fibers are nearly always used for interferometric sensing due to the ease in which the modes can be aligned for interference. Interferometric fiber sensors are usually made from conventional low-birefringence optical fibers. A problem with these fibers is that owing to the random fluctuations of the state of stress in the two arms of the interferometer, the polarization of the interfering beams change. For example, if the two interfering beams have orthogonal polarization states, the fringe intensity goes to zero. This effect is known as polarization-induced signal fading. The use of strongly birefringent fiber (also known as polarization-preserving fiber) is one way of overcoming this problem. The disadvantage of using strongly birefringent fiber is that it is more expensive than conventional fiber. (Udd, 1992)

For long fiber lengths, light intensity attenuation down the fiber becomes critical. In order to preserve adequate light intensity, the laser wavelength has to be chosen for low fiber attenuation.

3.8.3 *The Servo*

The role of the servo in the closed-loop detection scheme is to control the phase change in the reference arm to be exactly equal to the phase change in the sensing arm, and thus keeping the interferometer output at null. In order to keep the output close to null the open loop gain must be kept high enough (see for example Kuo, 1991). The phase error (ε) between the reference and sensing arms is given by

$$\varepsilon = \frac{dP}{G} \tag{3.22}$$

where dP is the phase difference between the reference and sensing arms and G is the open loop gain. Equation 3.22 shows that the higher the open loop gain is, the closed the output is to null. In order to reduce the phase error (ε), the phase difference (dP) needs to

be kept small and can be periodically set to zero.

3.8.4 *The Phase Transducer*

The role of the phase transducer is both in applying the A.C. modulation to the reference arm of the interferometer and to compensate for the relative change between the sensing and reference arm, thus keeping the interferometer output at null. For example a phase transducer can be constructed by wrapping the optical fiber from the reference arm around a piezoelectric tube. The voltage applied across the tube causes a change in the tube's circumference and thus the fiber length. One requirement for selecting the phase transducer is that it can apply sufficient modulation to the interferometer at the modulation frequency. Another requirement for the phase transducer is the ability to apply enough phase change to the reference fiber in order to compensate for the phase change in the sensing arm. One of the problems encountered in practice with the phase transducer is that for large changes in phase, the circuit components in the servo can become saturated limiting the ability of the phase transducer to compensate for the changes in the sensing arm of the interferometer. In order to overcome this problem, the servo output has to be zeroed on reaching saturation with a reset circuit.

3.9 Possible Areas of Application

The previous chapter has introduced and discussed the relative advantages and disadvantages of several existing NDE techniques for subsurface damage detection. In general the position and extent of the damage can occur at any location in the structure and is not known *a priori.* Hence large number of point sensing positions such as Bragg-grating sensors are needed to effectively monitor the whole structure. This chapter introduces a novel integrated strain sensing technique for subsurface damage detection. The method relies on measuring changes in integrated strain caused by moving a mechanical load over the damaged structural element. This technique is applicable for damage detection in any structure in which the mechanical load can be applied to at least one surface of the structure. The fiber-optic based technique described here has the advantage over traditional point sensing method since the damage state at any point along the fiber can be determined. The technique is particularly useful for the detection of cracks in large structures (such as civil engineering bridges, pavements and runways) for which a distributed point-sensing array is not practical due to the large number of point sensors needed to spatially cover the whole structure.

Chapter 4

THE THEORETICAL FEASIBILITY OF OPEN CRACK DETECTION

4.1 Introduction

Open cracks often occur in structural members which are either subjected to predominantly tensile loads or with manufacturing defects such as voids. In this chapter open cracks refer to crack in which the faces are sufficiently far apart so as to prevent mechanical contact between them. This chapter studies the theoretical feasibility of using the novel fiber optic integrated sensing technique for detecting the position and extent of open subsurface damage in some typical structural members.

4.2 Theoretical Mechanical Considerations for Open Crack Detection

The method proposed in this chapter relies on analyzing the differential signal change between damaged and undamaged structures when a load is moved across one of the surfaces of the structure. Two structures (1) a beam on an elastic foundation, and (2) a simply supported beam, are analyzed in this chapter in order to assess the applicability of this method. For open damage detection, the fiber-optic sensor is assumed to be surface mounted. The surface strains for an undamaged member can be derived analytically using simple elasticity theory. In general, no closed-form solution is available for the damaged structures analyzed in this thesis. Hence, numerical methods need to be used to solve for the strains at the sensor location. In order to compare the numerical results presented in this chapter with existing theoretical solutions and in order to simplify the analysis, the model is assumed to obey plane strain conditions and can thus be analyzed in two dimensions.

4.3 Sensor Performance for Undamaged Members

This section derives the theoretical phase change for the elastically supported and simply supported beams. The analyzed structures are assumed to be 1-dimensional, isotropic and elastic Bernoulli-Euler beams. The position of the sensor is assumed to be at the beam's top surface. Section 3.7 has shown that for surface mounted interferometric sensors, the phase change in the interferometer is directly proportional to the integral axial strain $\int \varepsilon_{xx} ds$. The constant of proportionality before the strain integral sign in equation 3.20 depends not only on the optical and mechanical properties of the fiber as is discussed in Section 3.7 but also on (a) the various gains in the closed loop interferometer which in the closed loop case is dependent on the phase-transducer to servo voltage relationship, and (b) the effectiveness of the strain transfer from the host structure to the fiber which is itself dependent on the attachment material and the relative stiffness of the host fiber and structural member. The constant of proportionality in equation 3.20 is therefore a calibration factor and is thus assumed to be a normalization factor in this theoretical section.

4.3.1 *Beam on an Elastic Foundation*

An undamaged elastically supported beam is depicted in Figure 4.1. The sensing arm of the interferometer is assumed to be bonded to the top surface of the beam *(y = h)*. The beam is assumed to be long such that $\beta L > 5$ (Timoshenko, 1976) where

$$\beta = \left(\frac{k}{4EI}\right)^{1/4} \tag{4.1}$$

and k is the foundation modulus, which can be estimated by (Vlasov and Leontev, 1960)

$$k = \frac{E_f}{H}$$

E is the elastic modulus of the beam, E_f is the elastic modulus of the foundation, H is the assumed depth of the foundation, and I is the second moment of inertia of the beam.

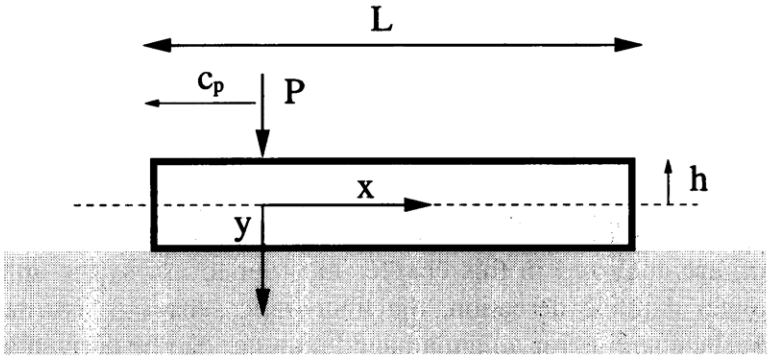

Figure 4.1: Schematic representation of a beam on an elastic foundation. The sensor is assumed to be attached to the beam's top surface.

The vertical deflection of the beam (v) at any point can be found in standard texts (Ugural and Fenster, 1987) to be:

$$v = \frac{P\beta}{2k}\{f_1(\beta x) + 2f_4(\beta c_p)f_4[\beta(x + c_p)] + f_3(\beta c_p)f_3[\beta(x + c_p)]\} \tag{4.2}$$

where P is the applied load, and

$$f_1 = e^{-\beta b}(\cos\beta x + \sin\beta x)$$

$$f_2 = e^{-\beta b}(\sin\beta x) \tag{4.3}$$

$$f_3 = e^{-\beta b}(\cos\beta x - \sin\beta x)$$

$$f_4 = e^{-\beta b}(\cos\beta x)$$

The axial strain on the top surface is given by

$$\varepsilon_{xx} = \frac{d^2v}{dx^2}h = \frac{P\beta^3 h}{k}\{f_3(\beta x) + 2f_4(\beta c_p)f_2[\beta(x+c_p)] + f_3(\beta c_p)f_1[\beta(x+c_p)]\} \tag{4.4}$$

For negative x, the above equation is modified by replacing x with $|x|$ in the $f_3(\beta x)$ term. The strain integral ($\int \varepsilon_{xx}$) is then calculated to be:

$$\int_{-c}^{L-c} \varepsilon_{xx}\, dx = \frac{P\beta^2 h}{k}\{f_2[\beta(L-c_p)] + f_4(\beta c_p)[f_1(\beta L) - 1] + f_3(\beta c_p)[f_4(\beta L) - 1] + f_2(\beta c_p)\} \tag{4.5}$$

4.3.2 *Simply Supported Beam*

An undamaged simply supported beam is shown in Figure 4.2. The fiber-optic sensor is once again assumed to be bonded on the top surface. The beam is assumed slender enough to allow use of the Bernoulli-Euler beam assumptions (typically $L > 10h$).

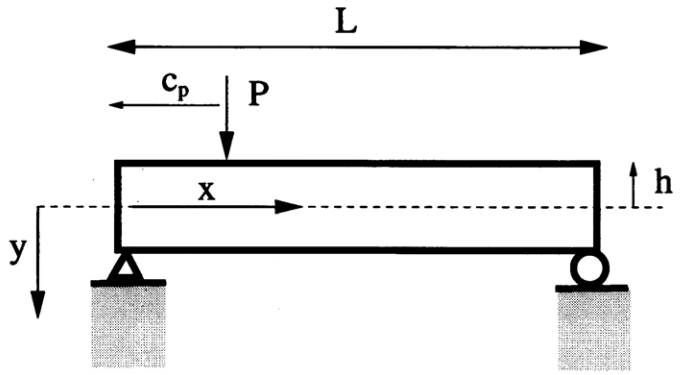

Figure 4.2: A simply supported beam subjected to a moving load

Elementary structural analysis gives the axial strain at the beam's top surface as:

$$\varepsilon_{xx} = \frac{P(L-c_p)xh}{LEI} \quad \text{for } x < c_p$$

$$\varepsilon_{xx} = \frac{P(L-c_p)xh}{LEI} - \frac{P(x-c_p)}{EI} \quad \text{for } x > c_p \tag{4.6}$$

The strain integral is given by

$$\int_{-c}^{L-c} \varepsilon_{xx}\, dx = \frac{Phc_p(L-c_p)}{2EI} \tag{4.7}$$

4.4 Open Crack Modeling Using the Finite Element Method

Since in general there are no closed-formed solutions for strains in arbitrarily damaged structures, a numerical solution method is needed. Though a myriad of solution techniques exist for solving these classical elasticity problems, the finite element method (FEM) is

chosen in this chapter. Some of the advantages of the FEM for solving open damage problems include the speed and robustness of the method. FEM commercial software is also readily available, which greatly simplifies pre- and post-processing tasks such as model input and data extraction.

4.4.1 *Model Assumptions*

The model geometry of the beam on elastic foundation is shown in Figure 4.3, where e is the axial position of the damage and f is the transverse position of the damage from the neutral axis. The elastic foundation is modeled by including a soft layer under the beam. The depth of the foundation layer (H) shown in Figure 4.3 is assumed to be 10 times the beam height. In order to maintain open-damage conditions, the damage zone is assumed to be rectangular.

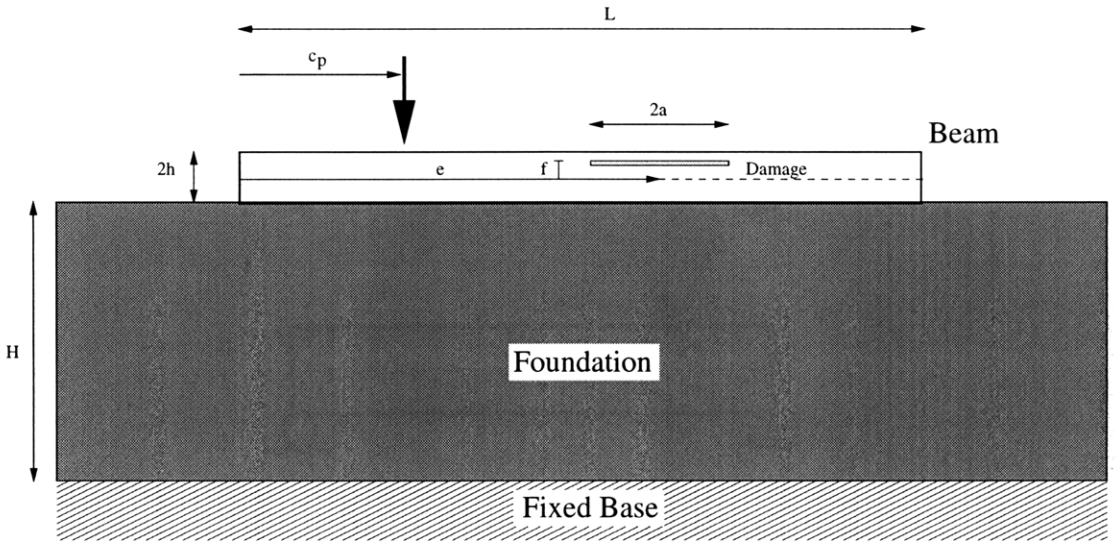

Figure 4.3: Physical model of the beam on elastic foundation

4.4.2 *Model Inputs*

The model parameters are assumed to be: beam length (L) 0.5 m and beam height ($2h$) 0.05 m. The damage is located at mid-height and mid-depth ($e=0.5L$, $f=0$). The damage length in the model varies from $2a=h$ to $2a=3h$, the height of the damaged zone is 1/5 of the total beam height. The material parameters are chosen so that the beam stiffness EI = 30000Nm^2 and the foundation stiffness β=20/m in equation 4.1. Substituting these values into equation 4.2 gives the foundation modulus (E_f) as 1.9 GPa.

4.4.3 *Boundary Conditions*

In the FEM, only the essential (geometric) boundary conditions need to be prescribed. The simply supported beam boundary conditions are modeled by assuming zero vertical and horizontal deflections at the left-bottom node and zero vertical and unconstrained horizontal deflections at the right-bottom node. For the beam on elastic foundation model, the bottom of the elastic layer is assumed to have no vertical and no horizontal deflections.

4.4.4 *Mesh Characteristics*

A sample mesh used for the damaged simply supported beam model is shown in Figure 4.4. The mesh consists of 206 quadratic, isoparametric plane strain elements. The damage zone is introduced by removing elements at the center of beam. The mesh is rect-

angular and is not intended to accurately capture the stress intensity factors near the damage edges. The ratio of the length to height of each element is kept at 3:2 which is well less than the recommended maximum 8:1 ratio (Desai, 1979). The mesh convergence is assumed adequate since doubling the number of model elements does not change the integral strain at any load position by more than 2%.

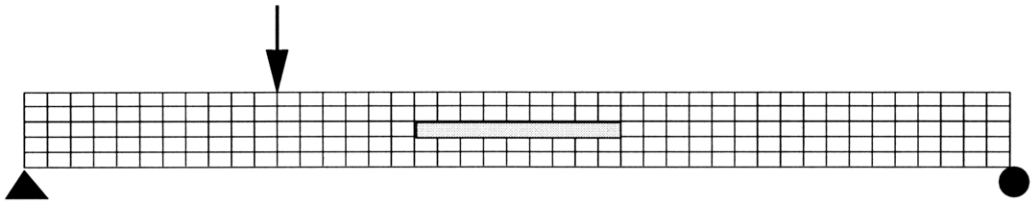

Figure 4.4: A sample FEM mesh used to analyze a damage simply supported beam.

A sample mesh for the damaged elastically supported beam is shown in Figure 4.5. The mesh consists of 665 quadratic isoporametric elements. The element mesh size in the elastic foundation layer increases with distance from the beam. The element mesh within the beam is kept exactly the same as for the simply supported case. The maximum element length to height ratio is kept at 8:1.

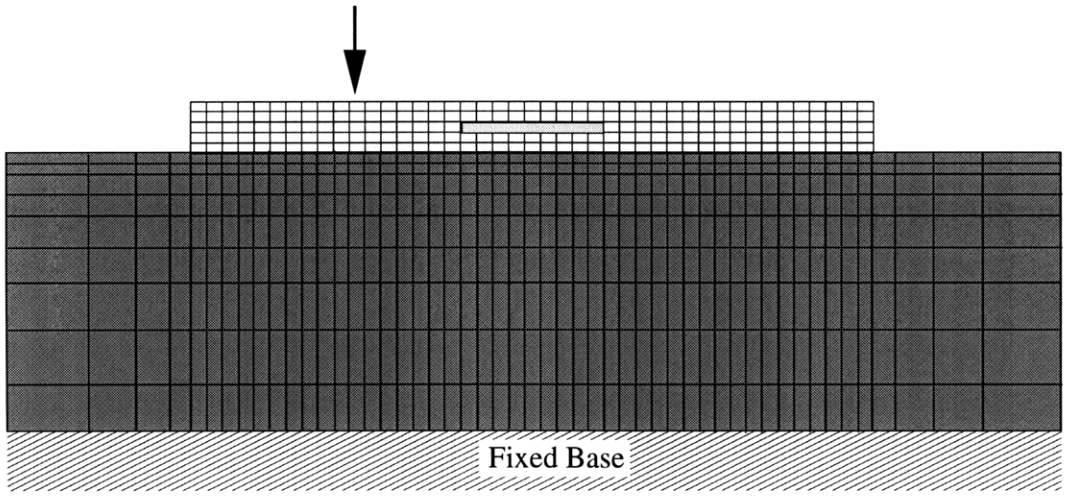

Figure 4.5: A sample FEM mesh used to analyze a damaged beam on elastic foundation

4.4.5 *Verification of the Finite Element Model*

In order to verify the FEM model, the numerical solution for the surface axial strain integral of the FEM model are compared with the theoretical solution for the virgin beams given in Section 4.3. Figure 4.6 shows a comparison of the numerical results with the theoretical strain integral for an elastically supported beam as given by equation 4.5. Figure 4.7 shows the numerical results with the theoretical strain integral for a simply supported beam as given by equation 4.7. Both Figures 4.6 and 4.7 show the excellent agreement between the FEM solution and the theoretical results.

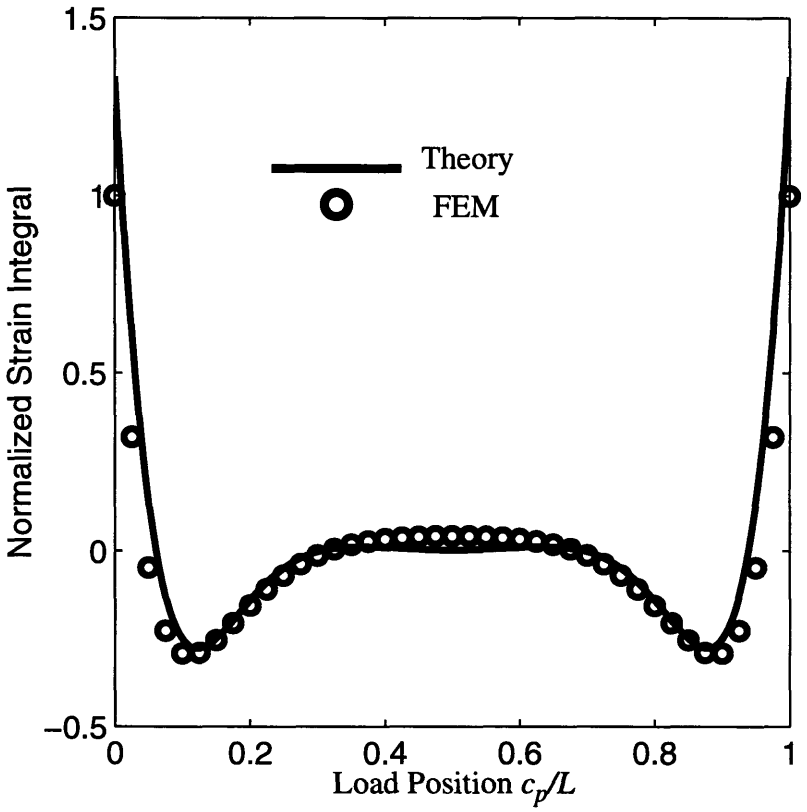

Figure 4.6: Comparison of the normalized strain integral for an undamaged beam on elastic foundation obtained from the analytical and FE solution

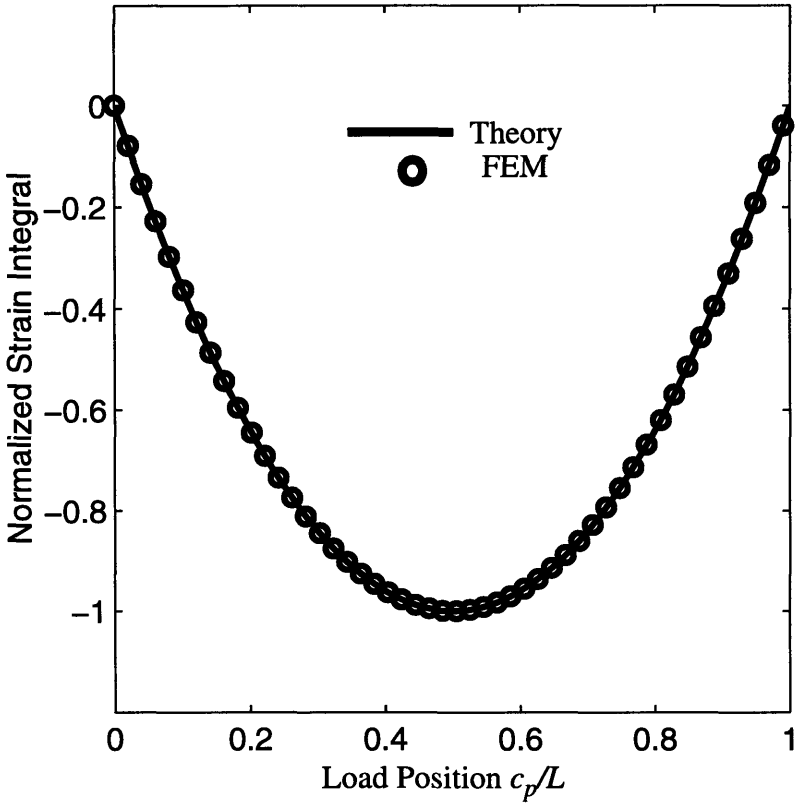

Figure 4.7: Comparison of the normalized strain integral for an undamaged simply supported beam obtained from the analytical and FE solution

4.5 Results for Open Damage

The feasibility of the damage sensing scheme is analyzed by comparing the effect for various damage lengths and locations for the two structural members. For each load position, the effect of the damaged zone, $(\Delta\Sigma)$ is calculated from the difference between the damaged (ε_D) and undamaged (ε_U) states.

$$\Delta\Sigma = \int(\varepsilon_D - \varepsilon_U)\, dx \tag{4.8}$$

The position of the damaged zone can be varied by changing its axial position along the beam (e) or its height (f) as shown in Figure 4.5.

A typical signal derived from the analysis of a damaged beam is shown in Figure 4.8a. This result is for a centrally located damage state ($e = L/2, f = 0$) with a crack length ($2a$) equal to $2a/L = 1/10$. The phase change is proportional to $\Delta\Sigma$ which is itself a function of applied load. To obtain the actual phase change requires knowledge of both the proportionality constant and the applied load during testing. This, however, is not our major concern because the objective of the study is to see how $\Delta\Sigma$ (and hence the phase change) is affected by delamination size and location. In all the following figures, $\Delta\Sigma$ is given in arbitrary units.

The differential of $\Delta\Sigma$, is defined as the differential of the strain integral, and is given by:

$$\Delta\Sigma' = \frac{d}{dc}(\Delta\Sigma) \tag{4.9}$$

Figure 4.8b shows $\Delta\Sigma'$ for the same case as shown in Figure 4.8a.

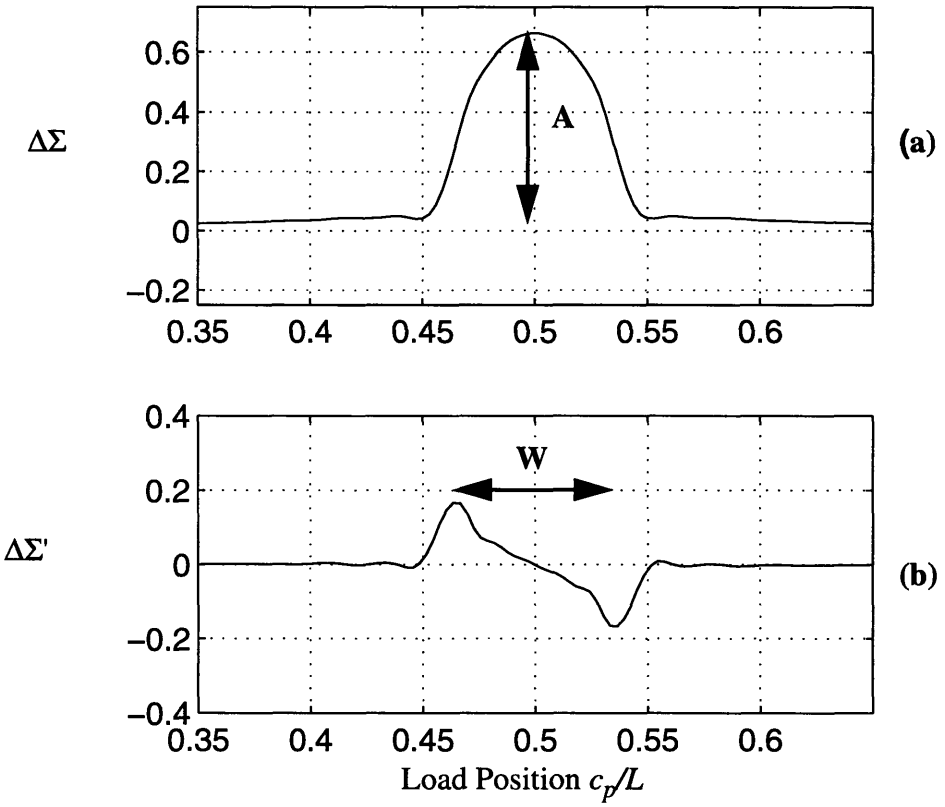

Figure 4.8: (a) A typical strain integral difference and (b) strain differential ($\Delta\Sigma'$) signal showing the amplitude (A) of the peak strain integral difference and the side band width (W).

It should be noted that extent of damage can be represented by two parameters (see Figure 4.8); (1) the side band length (W) which is defined as the width between the maximum and minimum values of $\Delta\Sigma'$, and (2) the peak amplitude of the signal (A) which is defined by:

$$A = \Delta\Sigma_{maximum} - \Delta\Sigma_{minimum} \tag{4.10}$$

where $\Delta\Sigma_{maximum}$ and $\Delta\Sigma_{minimum}$ are the maximum and minimum values of the strain integral difference ($\Delta\Sigma$), when the load position (c) is within the sideband W.

4.5.1 *Results for an elastically supported beam*

The effect of various centrally located ($e = L/2, f = 0$) damage zones are shown in Figure 4.9.

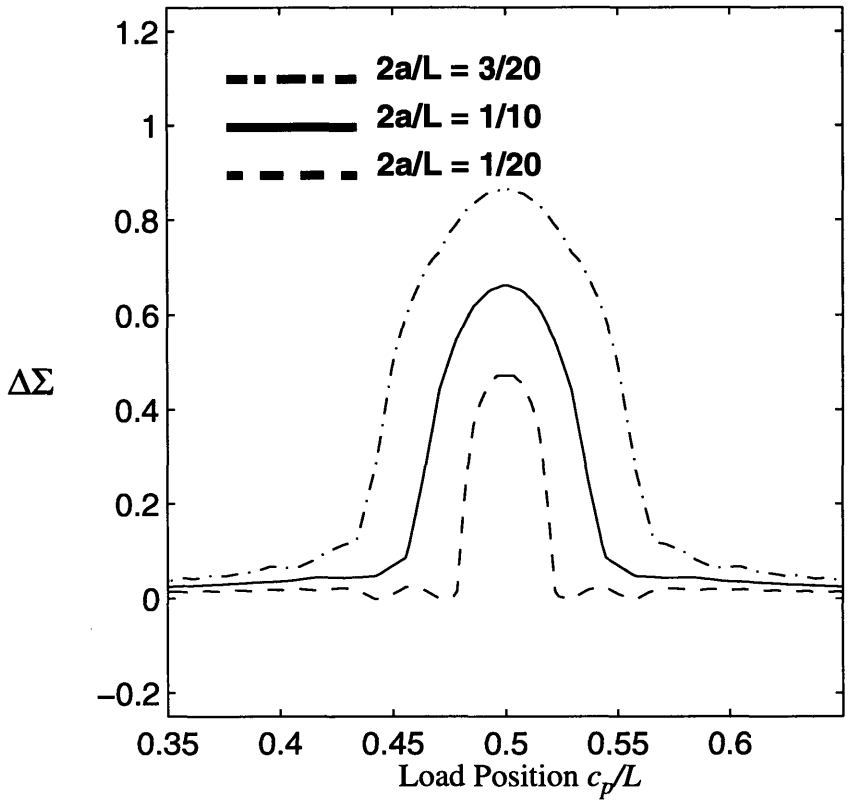

Figure 4.9: Effect of various centrally located cracks on the strain integral difference. The three crack lengths correspond to values of *2a/L= 1/20, 2a/L= 1/10* and *2a/L= 3/20.*

Two important features define the signal produced by the strain integral difference shown in Figure 4.9. These features are, (1) the axial location (e) of the damaged zone corresponds to the peak strain integral difference, and (2) the effect of increasing damage length ($2a$) is to increase both the peak value of the strain integral difference and the width of the side bands.

The effect of various crack heights (f) for an axially centered damage zone of fixed length is shown in Figure 4.10. The height of the damaged zone is changed by remeshing of the beam. The convergence of the mesh are rechecked by the same 2% strain integral criterion as previously explained.

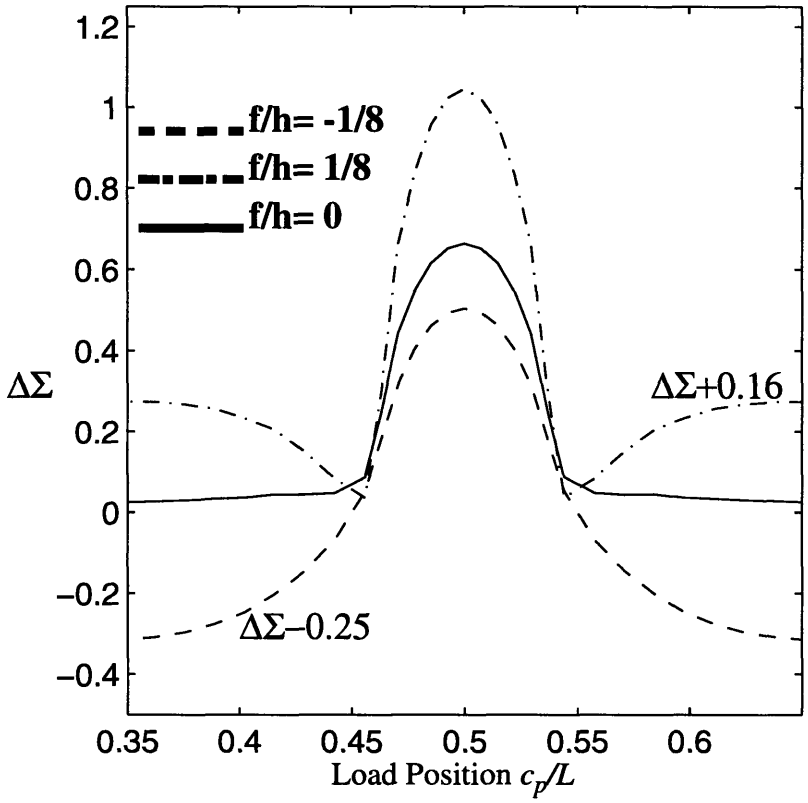

Figure 4.10: Effect of various crack depths (*f*) for damage located at *c/L = 0.5*. Crack length is *2a/L=1/10*. The crack heights correspond to values of *f/h = 1/8* (with 0.16 added to ΔΣ), *f/h = 0* and *f/h = -1/8* (with 0.25 subtracted from ΔΣ).

The effect of various crack depths can be clearly seen in Figure 4.10. For clarity, Figure 4.10 is plotted so as to keep the minimum strain integral difference ($\Delta\Sigma_{minimum}$) within each side band the same (the constant values added to each strain integral is shown in Figure 4.10). Figure 4.10 shows that as the damage approaches the top surface (to which the fiber is attached), the peak amplitude (*A*) increases while side band width (*W*) remains the same.

4.5.2 *Results for a simply supported beam*

Figure 4.11 shows the effect of various centrally located (*e = L/2, f = 0*) crack lengths for a simply supported beam. As in the elastically supported case, the position of the peak amplitude (*A*) corresponds to the center of the damage zone. The side band width (*W*) and peak amplitude value (*A*) correspond to the length of the damage zone.

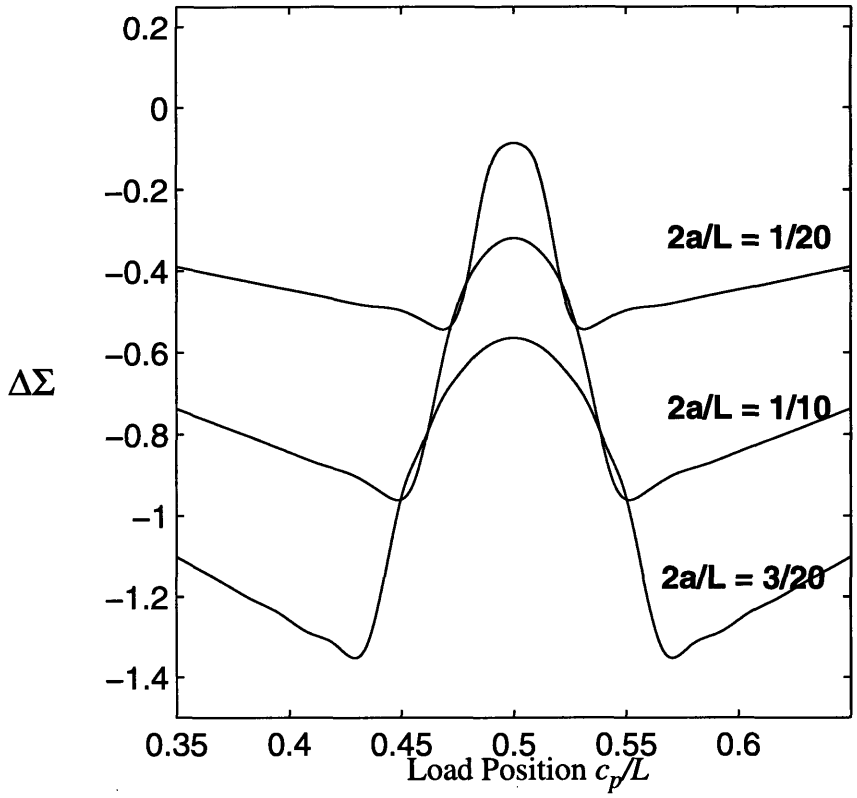

Figure 4.11: The effect of crack length for various simply supported beams with centrally located cracks ($e = L/2, f = 0$).

The effect of various crack depths for a simply supported beam is shown in Figure 4.12. For clarity, Figure 4.12 is plotted so as to keep $\Delta\Sigma_{minimum}$ within each side band the same. It should be noted that if we extend the plot to the supports, all strain integrals in Figure 4.12 will go to zero at $c_p/L=0$ and $c_p/L=1$.

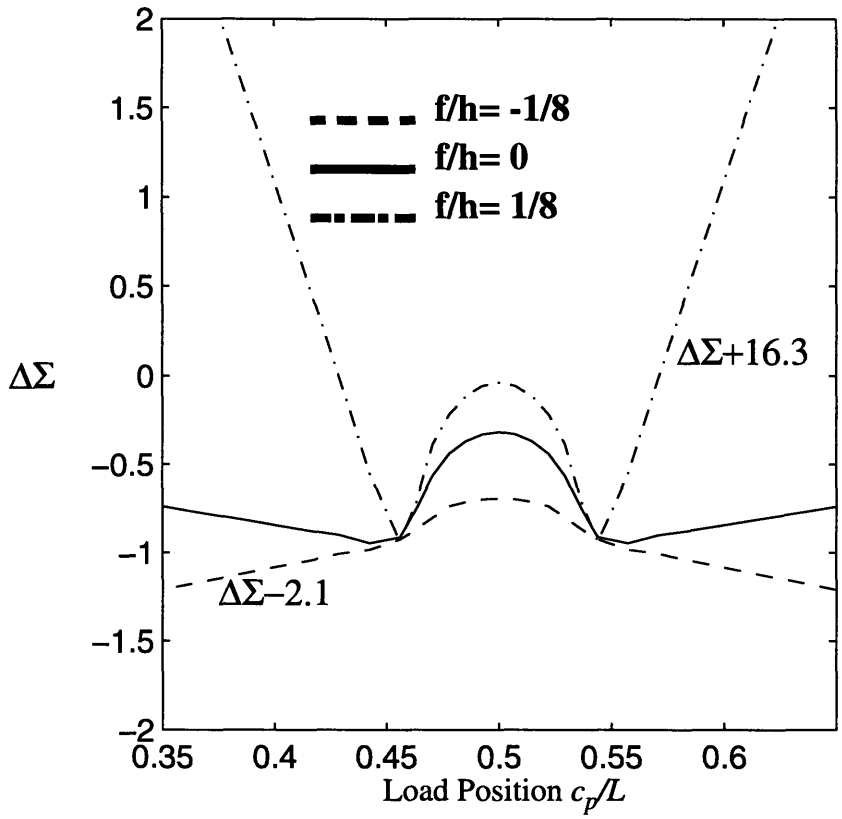

Figure 4.12: The effect of crack depth (*f*) for a simply supported beam with damage located at *c/L = 0.5*. Crack length is *2a/L=1/10*. The crack heights correspond to values of *f/h = 1/8* (with 16.3 added to ΔΣ), *f/h = 0* and *f/h = -1/8* (with 2.1 subtracted from ΔΣ).

In order to explain the signal trends in Figure 4.12, the axial strain fields are plotted for various load and damage cases in Figures 4.13 and 4.14. For both Figures 4.13 and 4.14 the crack length is *2a/L=1/10* and the axial range of the plot is between *0.4L* and *0.6L*. Figures 4.13a to 4.13d, show the axial strain band plots for the case of a quarter-span loaded (*c = L/4*) beam with no delamination and with the delamination at *f/h=0, f/h=1/8* and *f/h=-1/8*. Figure 4.13a show the axial strain band plot for the undamaged beam. As expected from simple beam theory, the axial strain linearly decreases from left to right across the beam as the bending moment decreases. Comparing the undamaged case (Figure 4.13a) and the centrally damaged case (Figure 4.13b) shows that the largest perturbation to the strain field occurs close to the delamination. The axial strain perturbation due to the delamination decreases as one moves away from the damage zone. Figure 4.13b shows that the axial strain remains symmetric about the center (*y=0*) of the beam. Comparing the undamaged case (Figure 4.13a) and the damaged case in Figure 4.13c (*f/h=1/8*), shows that the axial strains are no longer symmetric through the depth of the beam. In Figure 4.13c, relatively large axial strain perturbations occur at the top surface of the beam as compared with Figures 4.13b and 4.13d. This corresponds to the relatively large values of ΔΣ outside the bandwidth (*W*) as shown in Figure 4.12.

Figures 4.14a to 4.14d show the axial strain band plots for the case of a center span loaded (c_p=*L/2*) beam with no delamination and with the delamination at *f/h=0, f/h=1/8* and *f/h=-1/8*. Comparing Figures 4.14a to 4.14d, shows that the axial strain perturbation between damaged and undamaged beams on the beam's surface increases as the delamination height increases. After delamination occurs, the beam can be considered to consist of two parts (i) a small sub-beam made up of the material right above the delamination, and (ii) the rest of the member which acts as support to the small sub-beam on its two sides. Figure 4.15 shows the typical strain differential signal (ε_D–ε_W) for a simply supported beam with a centrally located crack and load at beam mid-span (c_p = *L/2*).

Careful inspection of Figure 4.15 shows tensile strains on both ends of the small sub-beam. These tensile strains indicate the existence of a hogging moment due to the partial constraint against rotation provided by the material at the ends of the small sub-beam. These tensile strains cause the strain integral shown in Figure 4.12 to become more positive when the load is over the delamination. It should be noticed that the tensile strains at the small sub-beam ends result from the assumption of an open crack. The trend of strain integral for a closed crack can be quite different. This topic is discussed in the following chapter

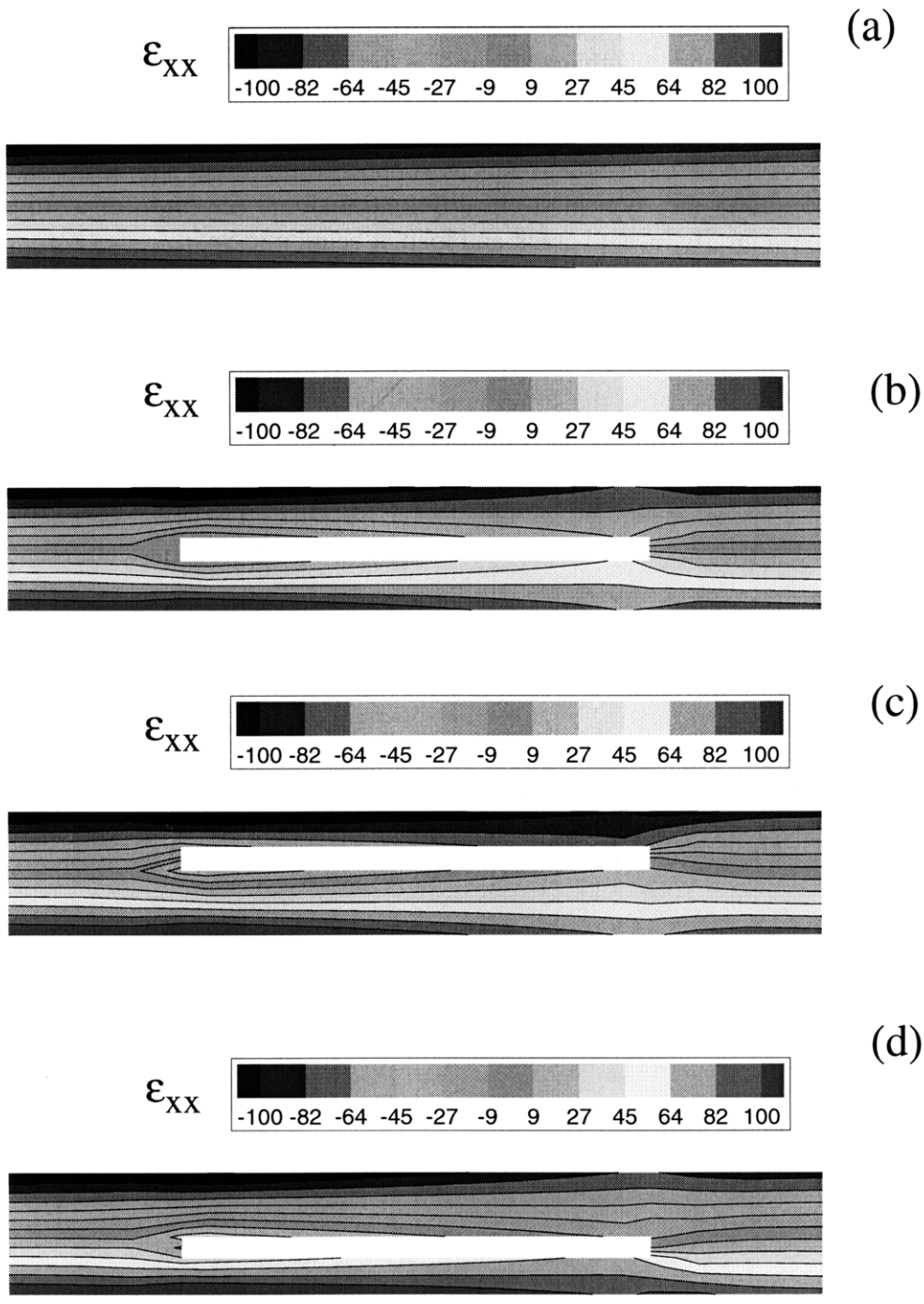

Figure 4.13: Axial strain band plots for delamination location corresponding to (a) undamaged beam, (b) damage at *f/h=0*, (c) damage at *f/h=1/8*, (d) damage at *f/h=-1/8*. Delamination length is *2a/L=1/10*. Load position is at $c_p/L=1/4$

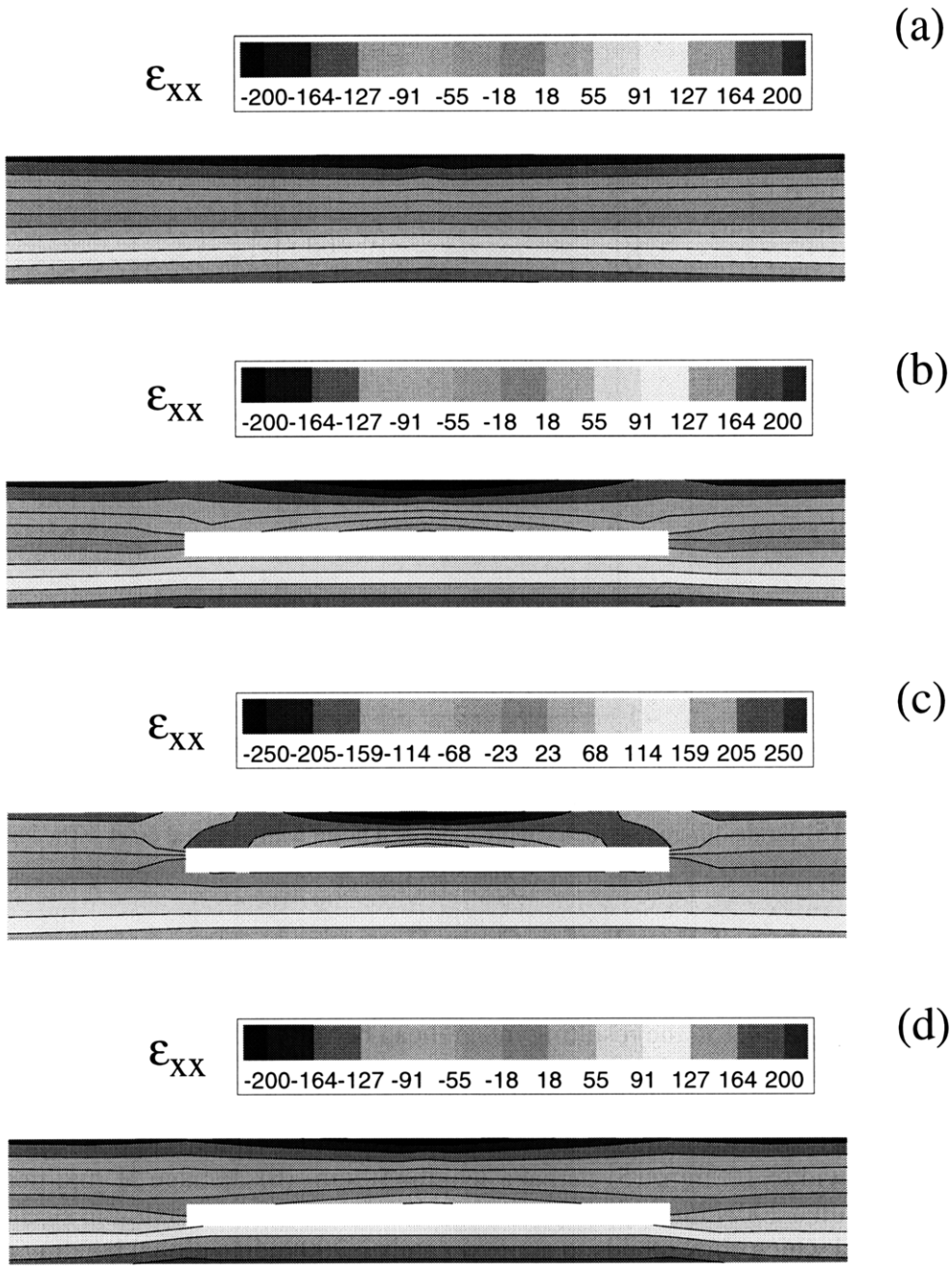

Figure 4.14: Axial strain band plots for delamination location corresponding to (a) undamaged beam, (b) damage at *f/h=0*, (c) damage at *f/h=1/8*, (d) damage at *f/h=-1/8*. Delamination length is *2a/L=1/10*. Load position is at $c_p/L=1/2$

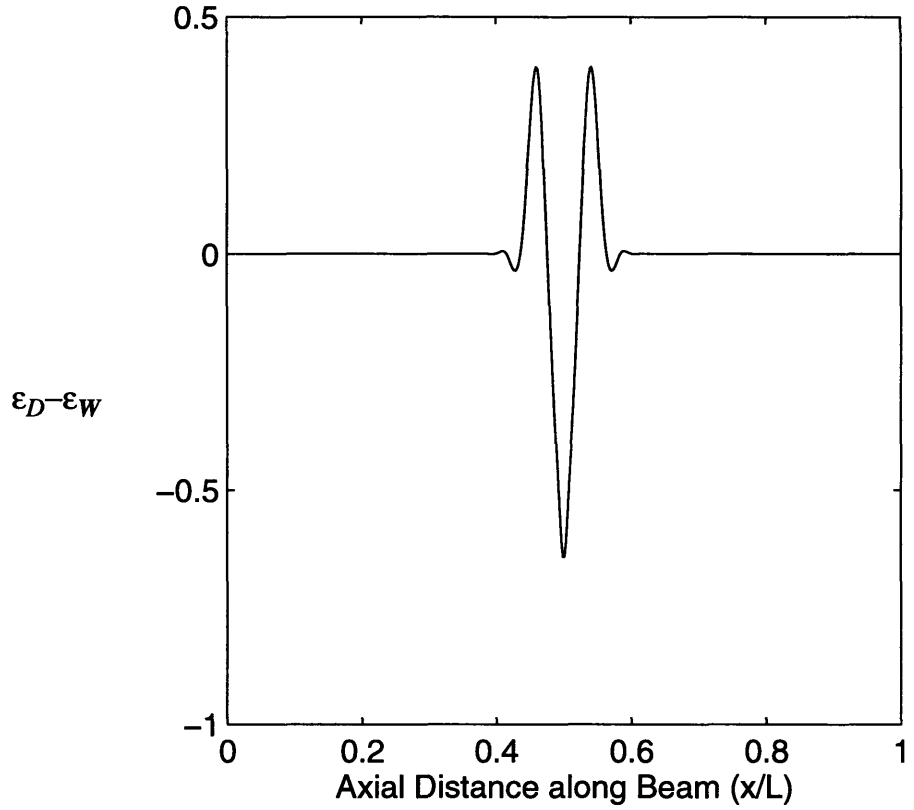

Figure 4.15: Strain differential for a simply supported beam with a central crack. The load position is at mid-span ($c_p = L/2$).

4.6 Discussion of Results for Open Damage

Due to the nature of the positive and negative components of the differential strain as shown in Figure 4.15, the resulting integral can be very small. To give a sense of the magnitude of the path-length change associated with this novel strain sensing technique, a simply supported aluminum beam with the following assumed properties and geometry was analyzed: (1) elastic modulus=70 GPa, (2) plate depth = 10mm, (3) plate length = 500mm, (4) plate width=100mm, (5) damage length=50mm, (6) damage at mid-depth and mid-length. With a 200N load applied at the center of the beam, a maximum strain of 200με is introduced which corresponds to approximately a 700 radian global bending phase change from Equation 3.20 and Equation 4.7. For this case the amplitude (A) of the path-length change is calculated to be 350 nm. Using the strain transfer value of c_o=0.11 (in Equation 3.20) reported by Sirkis and Haslach (1990) gives a phase change amplitude of 4.5 rads for a light wavelength of 632 nm and refractive index of 1.456. Sensitive sensing methods are thus needed to be utilized for this type of technique to be successful.

The axial location of the damage can be easily determined by locating the peak in the strain integral difference. The length of the damage zone can be determined from the width of the side band. Once the side band width is determined, the amplitude of the peak strain integral provides the information needed to locate the depth of the damage. Since

no two crack positions can produce the exact same signal, the proposed method unambiguously determines the position and extent of damage.

The results for various crack depths (as shown in Figures 4.10 and 4.12) show that as the fiber sensor location approaches the damage zone, the peak amplitude (A) increases. This implies that the sensitivity of this scheme can be improved with embedded fibers.

Chapter 5

THE THEORETICAL FEASIBILITY OF DETECTING CLOSED CRACKS

5.1 Introduction

The previous chapter dealt with the detection of open subsurface cracks using a novel fiber optic sensing method. However, in many practical situations, the consideration of crack closure is important in predicting the static and fatigue strength of structures subjected to global of local compressive stresses. For example, the growth of closed cracks under Mode II loading is the dominant failure modes for cracks in compressive fields. Closed cracks typically occur as a precursor to the final spalling damage by fretting fatigue in subsurface cracks (Hearle and Johnson, 1985) under moving rolling load. Furthermore, the growth of closed (kissing) cracks in laminated materials, which are formed due to impact damage or manufacturing defects, is one of the primary failure modes in composite structures.

This chapter deals with the theoretical feasibility of detecting closed cracks using the novel fiber optic damage detection method. Due to the non-linear nature of the contact problems associated with crack closure, the solution of these problems require extensive computational effort. Since the proposed damage detection technique requires the computationally time consuming solution of the contact crack problem for multiple load positions and crack geometries, this chapter first focuses on the development of a fast and efficient method for solving crack closure problems. The second part of this chapter concentrates on the feasibility of the novel detection method for closed cracks.

5.2 Background to existing methods of solving crack closure problems

The mechanics of crack closure has been extensively studied by many authors using various numerical, experimental and analytical techniques (Lee, 1997). The two most frequently used numerical techniques for studying fracture mechanics problems are the finite element method (FEM) and boundary element method (BEM). The main advantage of the BEM over FEM is that only the domain boundaries (which include the boundaries) need to be discretized. Contact can be easily included in the BEM since all the unknowns of the problem such as the contact tractions and displacements are boundary quantities. The BEM has another advantage of being particularly adept in calculating important fracture mechanics parameters such as stress intensity factors (SIF) and crack growth directions. The greatest disadvantage of the BEM is that the associated matrices are non-symmetric and are fully populated. Therefore these matrices cannot be as efficiently solved as the banded and symmetric FEM matrices.

Various BEM's have been proposed for solving crack problems. The most frequently used BEM is the subregion method (Blanford, *et al.* 1981). In the subregion method the cracked body is subdivided into two subregions and the traction and displacements along

all common nodes not on the crack faces are constrained to have equal displacements. The problem with the subregion method is that the resulting matrices tend to be large due to the extra nodes along the subregion interfaces which do not lie along the boundary of the body. Crouch (1976) has developed the displacement discontinuity boundary element method (DDBEM) which overcomes the problem associated with the constrained nodes in the subregion method. In the DDBEM, only the crack itself and external boundaries of the body are modeled assuming the displacements to be discontinuous across these boundaries. An integral equations written in terms of the applied tractions and displacement discontinuities are formulated and solved numerically.

Other methods have also been used to solve the open crack problem but have not yet been extended to the closed crack problem. An iterative method was proposed by Ameen and Raghuprasad (1994). In this method the body is subdivided into two sub-problems as shown in Figure 5.1. Sub-problem 1 models the body subjected to the prescribed force and displacement boundary conditions without the crack. Sub-problem 2 models a crack in an infinite domain subjected to internal shear and normal tractions. Iteration between the two sub-problems is then performed until all the boundary conditions in both bodies are satisfied. The final solution for the unknowns is a super-position of the unknowns of the two bodies. Ameen and Raghuprasad (1994) did not consider closed cracks and commented that the only advantage of their iterative method over other methods such as the DDBEM is that the matrix associated with each region requires less storage space than the combined problem and thus can be handled by computers with smaller memory storage.

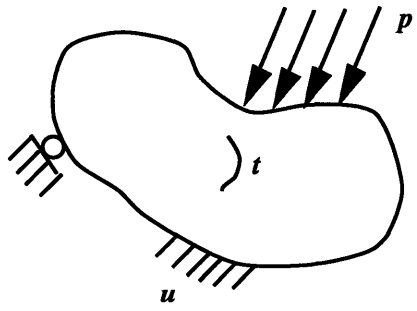

(a) Original Body with Crack

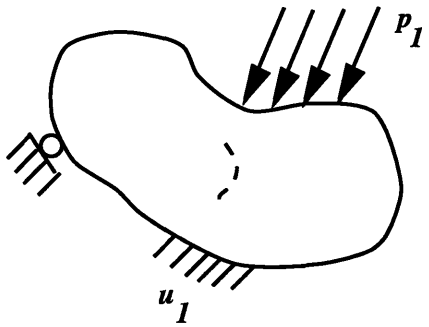

(b) Sub-problem 1: Uncracked body

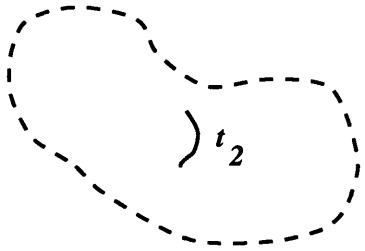

(c) Sub-problem 2: Crack in an infinite domain

Figure 5.1: Schematic Representation of the iterative method of solving crack problems after Ameen and Raghuprasad

Another method discussed by Sturt *et al.* (1993) uses a hybrid method in which the DDBEM is used to model the outer boundaries of the structure while a distributed dislocation technique (DDT) is used to model the crack. The greatest advantage of the DDT is that the stress tip singularities can be accurately calculated. Sturt *et al.* (1993) did not consider crack closure though the DDT can be extended to include this case.

This chapter discusses a coupled iterative-hybrid boundary element method (IHBEM). In this method the two bodies are modeled separately as described by Ameen and Raghuprasad (1994). Sub-problem 2 is modeled either by using the DDT or DDBEM. The advantage of the IHBEM is that since contact problems are non-linear, iteration is typically required for all solution methods, and since the IHBEM iterates on smaller matrices, the method can potentially prove to be significantly faster than traditional techniques. The method has the added advantage that any standard BEM code can be easily modified to obtain results for the crack-free region.

Closed crack simulation is particularly important in the study of subsurface crack growth under moving point loads and thus this problem has been extensively studied by various authors (see Komvopoulos, 1996 for a list of existing methods). A subsurface crack under a moving point load has been chosen as one of the example problems to illustrate the IHBEM since the crack face mechanisms illustrated by this example problem is directly applicable to the study of closed crack sensing by the novel detection method.

5.3 Theoretical Formulation

A two dimensional cracked body shown in Figure 5.1(a) is subjected to prescribed tractions (p) and displacements (u) on the outer boundary and tractions (t) on the crack surface. The body is assumed to be linear elastic, homogenous and isotropic. The problem is first partitioned into two subregions. Sub-problem 1, shown in Figure 5.1(b) represents the original body without the crack subjected to all the external boundary conditions (p_1 and u_1). Sub-problem 2, shown in Figure 5.1(c), represents a crack in an infinite body subjected to prescribed tractions (t_2). Any BEM can be used to solve the boundary value problem for both sub-problems. In this chapter however, sub-problem 1 is solved using the Quadratic Displacement Discontinuity (QDD) method (Bhattacharyya and Willment, 1988). Sub-problem 2 is solved using either the distributed dislocation technique (DDT) or QDD method. After sub-problem 1 is solved, the normal and shear tractions are calculated at the position of crack (t_2). These tractions are then applied as negative forces on the crack-faces of sub-problem 2. Sub-problem 2 is then solved and the boundary conditions on the boundaries of sub-problem 1 are calculated. These boundary conditions are then subtracted from the existing boundary conditions (p) of sub-problem 1 and the tractions at the crack are recalculated. The iterations between sub-problems 1 and 2 are performed until convergence is achieved.

5.3.1 *Background to the QDD method*

In the displacement discontinuity method, the analyzed body is subdivided into a series of N elements with unknown displacement discontinuities over each one. The unknown displacement discontinuities are then solved by summing the effects of all N elements so as to satisfy the prescribed boundary conditions. If stresses are prescribed on the ith element then the ith equations of the system are

$$ {}^{i}\sigma_s = \sum_{j=1}^{N} {}^{ij}A_{ss}\,{}^{j}D_s + \sum_{j=1}^{N} {}^{ij}A_{sn}\,{}^{j}D_n \text{ and } {}^{i}\sigma_n = \sum_{j=1}^{N} {}^{ij}A_{ns}\,{}^{j}D_s + \sum_{j=1}^{N} {}^{ij}A_{nn}\,{}^{j}D_n \tag{5.1} $$

Similarly for the prescribed displacements

$$ {}^{i}u_s = \sum_{j=1}^{N} {}^{ij}B_{ss}\,{}^{j}D_s + \sum_{j=1}^{N} {}^{ij}B_{sn}\,{}^{j}D_n \text{ and } {}^{i}u_n = \sum_{j=1}^{N} {}^{ij}B_{ns}\,{}^{j}D_s + \sum_{j=1}^{N} {}^{ij}B_{nn}\,{}^{j}D_n \tag{5.2} $$

where σ_s and σ_n are the tangential and normal stresses respectively. ${}^{ij}A$ and ${}^{ij}B$ are the stress and displacement influence coefficients respectively which relate the stresses (or displacements) of node i to a unit displacement discontinuity at node j. D_s and D_n are the shear and normal displacement discontinuities respectively which represent the relative displacements between the faces of a crack as shown in Figure 5.2.

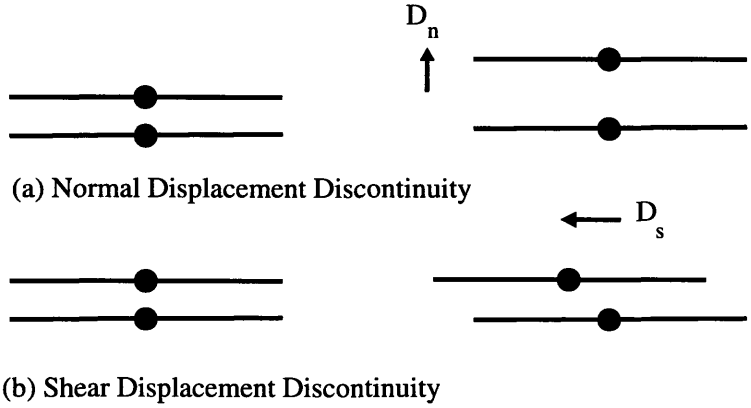

Figure 5.2: Schematic representation of normal and shear displacement discontinuities.

In the case of an assumed quadratic variation in displacement discontinuity, Bhattacharyya and Willment (1988) have shown that

$$ \boldsymbol{D} = \boldsymbol{D}(-b)\left[\frac{1}{2b^2}x(x-b)\right] + \boldsymbol{D}(0)\left[1-\frac{x^2}{b^2}\right] + \boldsymbol{D}(b)\left[\frac{1}{2b^2}x(x+b)\right] \tag{5.3} $$

where $\boldsymbol{D}$ has components D_s and D_n and needs to be evaluated at three points (nodes) along the element. In general the nodes can be placed at any position within the element except the element end-points where the stresses are infinite. In Equation 5.3 the nodes are placed at x=-b, x=0 and x=b. The influence coefficients ${}^{ij}A$ and ${}^{ij}B$ for the quadratic displacement discontinuity have analytical representations and are given by Bhatta-

charyya and Willment (1988) and in the included in Appendix A. Equations 5.1 and 5.2 can be formulated in matrix form as

$$\{\boldsymbol{b}\} = [\boldsymbol{C}]\{\boldsymbol{D}\} \tag{5.4}$$

where vector $\{\boldsymbol{b}\}$ are the prescribed boundary conditions, $[\boldsymbol{C}]$ is the influence function matrix and $\{\boldsymbol{D}\}$ is the displacement discontinuity vector. Once $\{\boldsymbol{D}\}$ is calculated, the stresses and displacements $\{\boldsymbol{f_1}\}$ for any set of interior points can be calculated using

$$\{f_1\} = [\boldsymbol{E}_1]\{\boldsymbol{D}\} \tag{5.5}$$

where $[\boldsymbol{E_1}]$ is the influence matrix relating the stresses and displacements of the interior point to the boundary displacement discontinuities.

5.3.2 *Background to the DDT method*

Consider a single dislocation of Burger's vector $\boldsymbol{b}$ (with components b_x and b_y) located at (x_d,y_d) in an infinite elastic domain shown in Figure 4.3. The resulting stresses and displacements at a second point (x,y) are (Hills *et. al.*, 1996)

$$\sigma_{xx}(x, y) = 2\frac{\mu}{\pi(\kappa + 1)}\{b_x G_{xxx} + b_y G_{yxx}\} \tag{5.6}$$

$$\sigma_{yy}(x, y) = 2\frac{\mu}{\pi(\kappa + 1)}\{b_x G_{xyy} + b_y G_{yyy}\} \tag{5.7}$$

$$\sigma_{xy}(x, y) = 2\frac{\mu}{\pi(\kappa + 1)}\{b_x G_{xxy} + b_y G_{yxy}\} \tag{5.8}$$

$$u_x(x, y) = \frac{1}{2\pi(\kappa + 1)}\{b_x U_{xx} + b_y U_{yx}\} \tag{5.9}$$

$$u_y(x, y) = \frac{1}{2\pi(\kappa + 1)}\{b_x U_{xy} + b_y U_{yy}\} \tag{5.10}$$

where μ is the shear modulus, κ=3-4ν in plane strain (ν being the Poisson's ratio). G_{lmn} and U_{ij} are the stress and displacement dislocation influence coefficients respectively given in Appendix B.

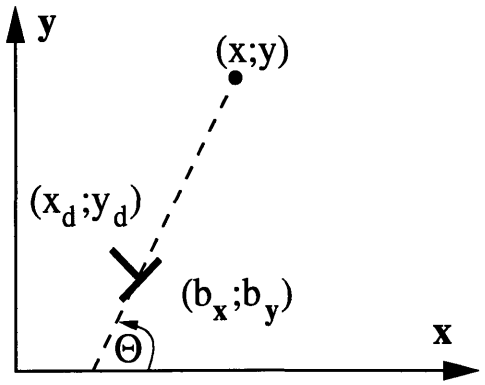

Figure 5.3: A dislocation with Burger's vector (b_x and b_y) in an infinite elastic space.

Consider a crack of length $2a$ with local co-ordinates x and y shown in Figure 5.4. By placing a dislocation density $\boldsymbol{B}$ (with components B_x and B_y) over the crack, the stresses and displacements at any point (x,y) can be calculated using

$$\sigma_{ij}(x, y) = 2\frac{\mu}{\pi(\kappa + 1)}\int_{-c}^{c}(B_x G_{\hat{x}ij}(x, y, \xi, 0) + B_y G_{\hat{y}ij}(x, y, \xi, 0))d\xi \tag{5.11}$$

$$u_i(x, y) = \frac{1}{2\pi(\kappa + 1)}\int_{-c}^{c}(B_x U_{i\hat{x}}(x, y, \xi, 0) + B_y U_{i\hat{y}}(x, y, \xi, 0))d\xi \tag{5.12}$$

where $B_k = (db_k)/(d\hat{x})$, $G_{\hat{k}ij}$ and $U_{i\hat{k}}$ are the local coordinate stress and displacement influence functions for a Burger's vector density in the k direction respectively. A standard tensor coordinate transformation is needed to map the global influence functions to the local coordinates (see Hills *et al.*, 1996) .

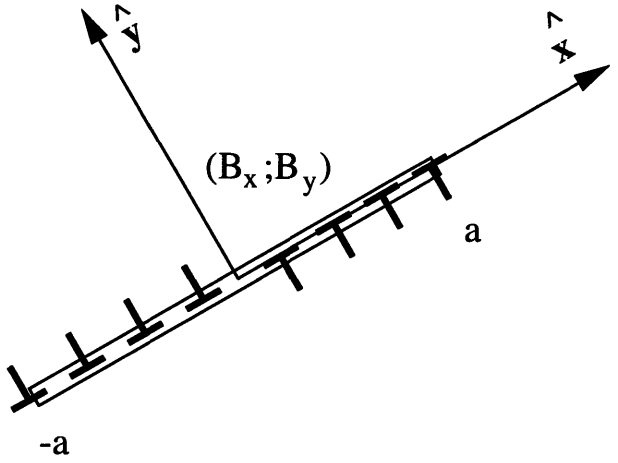

Figure 5.4: A crack modeled by a distribution of dislocation densities (B_x and B_y)

It must be noted that in general the integrals in equations 5.11 and 5.12 contain singularities of the order $1/\sqrt{d}$ which cannot be solved analytically and require special numerical integration techniques such as Gauss-Chebyshev quadrature. (For a full explanation of Gauss-Chebyshev quadrature see Hills *et al.*, 1996). Since there is a -1/2 singularity at the crack tip, B_k can be expressed as $B_k = \phi_k/\sqrt{a^2 - x^2}$ where ϕ_k is a non-singular function. After numerical integration, equation 5.11 and 5.12 can be rewritten as

$$\{\boldsymbol{T}\} = [\boldsymbol{G}]\{\Phi\} \tag{5.13}$$

where vector $\{\boldsymbol{T}\}$ corresponds to the prescribed boundary conditions, $[\boldsymbol{G}]$ is the dislocation influence matrix and vector $\{\Phi\}$ represents the unknowns ϕ_k. Once $\{\Phi\}$ is computed, the unknown dislocation density $\{\boldsymbol{B}\}$ can be obtained. Equations 5.11 and 5.12 can also be used to calculate the stresses and displacements $\{\boldsymbol{f_2}\}$ at any point in the domain using

$$\{f_2\} = [E_2]\{B\} \tag{5.14}$$

where $[E_2]$ is the influence matrix relating the stresses and displacements of the interior point to the dislocation densities.

5.3.3 *Background to the analysis of closed crack*

Consider a partially closed crack of length $2a$ shown in Figure 5.5. For each pair of corresponding particles located on either face of the closed portion of the crack, the relative normal displacement are constrained to be equal and the shear tractions are related to the normal tractions through a friction law. In the case of Coulomb friction, the crack faces will stick and the relative shear displacement will be zero if

$$|S| < c + \mu N \tag{5.15}$$

where S and N are the shear and normal tractions along the closed portion of the crack, and c and μ are the cohesion and the coefficient of friction respectively. In the case when the shear traction (S) is sufficiently large to overcome stick, the shearing traction is limited by friction, i.e.

$$|S| = c + \mu N \tag{5.16}$$

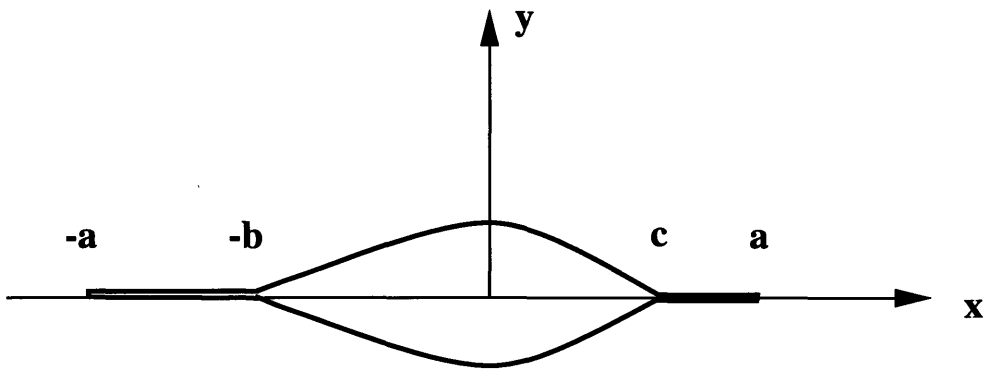

Figure 5.5: A schematic depiction of a partially closed crack

For the crack shown in Figure 5.5, the location of the crack closure points b and c as well as the stick/slip conditions are unknown and need to be found as part of the solution. Although the DDT can be used to solve crack-closure problems, the resulting integral equations tend to require complicated formulation which are beyond the scope of this thesis and the interested reader is referred to Hills *et al.* (1996).

A more practical method for solving closed crack problems is given by Crouch (1979) in which the crack surfaces are connected by springs with constant normal stiffness K_n and shear stiffness K_s so that

$$^iS = K_s{}^iD_s \text{ and } ^iN = K_n{}^iD_n \tag{5.17}$$

Now combining equations 5.1 and 5.17 gives

$$0 = -K_s{}^{i}D_s + \sum_{j=1}^{N} {}^{ij}A_{ss}{}^{j}D_s + \sum_{j=1}^{N} {}^{ij}A_{sn}{}^{j}D_n \text{ and } 0 = -K_n{}^{i}D_n + \sum_{j=1}^{N} {}^{ij}A_{ns}{}^{j}D_s + \sum_{j=1}^{N} {}^{ij}A_{nn}{}^{j}D_n \quad (5.18)$$

By choosing relatively large values of K_n and K_s, the faces of the crack can be prevented from relative deformations. In general crack-closure problems are path dependent which means that load incrementing is needed to find the final displacement and stress state of the body. At any load step (k), the shear and normal tractions calculated in equation 5.16 have to be compared with the Coulomb friction criterion given by equation 5.15. If the shear traction S is sufficiently large to overcome stick, equation 5.16 and 5.1 need to be used giving

$$c + \mu N = \sum_{j=1}^{N} {}^{ij}A_{ss}{}^{j}D_s + \sum_{j=1}^{N} {}^{ij}A_{sn}{}^{j}D_n \text{ and } 0 = -K_n{}^{i}D_n + \sum_{j=1}^{N} {}^{ij}A_{ns}{}^{j}D_s + \sum_{j=1}^{N} {}^{ij}A_{nn}{}^{j}D_n \quad (5.19)$$

At any load increment, the normal tractions on the faces can be negative indicating separation of the crack faces. In this case the crack-faces are stress free and Equation 5.1 becomes

$$0 = \sum_{j=1}^{N} {}^{ij}A_{ss}{}^{j}D_s + \sum_{j=1}^{N} {}^{ij}A_{sn}{}^{j}D_n \text{ and } 0 = \sum_{j=1}^{N} {}^{ij}A_{ns}{}^{j}D_s + \sum_{j=1}^{N} {}^{ij}A_{nn}{}^{j}D_n \quad (5.20)$$

At load step (k) an element that has slipped in a previous step can stick in which case the old shear stress S_{old} is "locked" into the model which is given by

$$S_{old} - K_s({}^{i}D_s)_{old} = -K_s{}^{i}D_s + \sum_{j=1}^{N} {}^{ij}A_{ss}{}^{j}D_s + \sum_{j=1}^{N} {}^{ij}A_{sn}{}^{j}D_n \quad (5.21)$$

Equations 5.18 to 5.21 need to be solved iteratively until all boundary conditions are satisfied.

5.3.4 *Iterative Solution Technique*

The iterative solution technique presented in this chapter extends the work of Ameen and Raghuprasad (1994) to include closed crack problems. The following algorithm can then be used to solve the problem.

(1) Compute the matrices $\boldsymbol{C}$, $\boldsymbol{G}$, $\boldsymbol{E_1}$ and $\boldsymbol{E_2}$ in Equations 5.4, 5.5, 5.13 and 5.14

(2) Factorize matrix $\boldsymbol{C}$ using $[\boldsymbol{C}]=[\boldsymbol{L}][\boldsymbol{U}]$, where $\boldsymbol{L}$ and $\boldsymbol{U}$ are the lower and upper matrices.

(3) Calculate $\boldsymbol{D}$ for sub-problem 1 from $\{\boldsymbol{b}\}=[\boldsymbol{L}][\boldsymbol{U}]\{\boldsymbol{D}\}$.

(4) Find the stresses $\boldsymbol{f_1}$ at the internal points corresponding to the crack position of sub-problem 2.

(5) The calculated stresses $\boldsymbol{f_1}$ are assumed to act as tractions on the crack faces of subproblem 2. The crack is assumed closed at all points and the crack face reactions are calculated.

(6) Use equations 5.18 to 5.21 to calculate the crack discontinuities and tractions on each element. The various conditions that need to be checked for each element are as follows:

(6.1) If the frictional sliding forces are smaller than the normal contact resisting force - corresponding to a condition of stick - use Equation 5.18

(6.2) If the frictional sliding force is greater than the normal contact resisting force - corresponding to a condition of slip - use Equations 5.19

(6.3) If the normal contact resisting force is negative - corresponding to separation of the crack faces - use Equation 5.20

(6.4) If a previously slipped element sticks, the previous shear stress is "locked" into the element and Equation 5.21 needs to be used

(7) Repeat steps (8) to (12) below till sufficient accuracy is obtained

(8) Calculate the unknown stresses/displacements f_2 from sub-problem 2 at the boundary points of sub-problem 1.

(9) Modify the prescribed boundary conditions in subproblem 1 by subtracting f_2 and the new displacement discontinuities are calculated from $\{b\} - \{f_2\} = [L][U]\{D\}$

(10) Recalculate the stresses f_1 at the internal points corresponding to the crack position of sub-problem 2.

(11) The calculated stresses f_1 are assumed to act as negative tractions on the crack faces of subproblem 2.

(12) Solve subproblem 2 using equations 5.18 to 5.21 as described in 6 above.

(13) The final displacement and stresses solutions at any point in the body is derived by superposition of the solutions for sub-problems 1 and 2.

It must be noted that LU decomposition is used to factorize matrix C since in general step (8) has to be calculated at least 4 times for open cracks and 10 times for closed cracks before convergence is achieved. Since **LU** decomposition only requires back-substitution at each step, this is considerably faster than the full reduction of C at each step.

5.4 Some Practical Aspects of Using the Iterative Boundary Element Method

The performance of any contact algorithm is dependent on (1) the initial assumptions of the conditions at the crack i.e. is the crack initially open or closed, and (2) the method in which the constraints are enforced.

Since crack closure is both a non-linear and an history dependent phenomena, the final solution of the problem is strongly influenced by the initial assumptions of the crack behavior. Whether the crack is initially assumed open or closed could significantly effect the final solution. The first step of the iteration begins by calculating the tractions at the crack position from sub-problem 1. In the present boundary element approach, the crack is assumed to be initially fully closed (i.e. both shear and normal springs are applied to the crack faces and the faces are assumed to be stuck- this follows the Crouch and Starfield,

1983 approach). The crack-face tractions calculated from sub-problem 1 are applied to sub-problem 2 and the displacement discontinuities for sub-problem 2 are calculated. The dominant crack-face mechanism for sub-problem 2 is checked and modified as described in Step 6 of Section 5.3.4. The solution method then follows Steps 7 to 13 in Section 5.3.4 until sufficient accuracy has been achieved

A second problem arises in modeling closed cracks using spring constraints - namely the spring constraint stiffnesses (K_s and K_n) cannot be assumed arbitrarily large since this can lead to ill-conditioned matrices (see Bathe, 1996). One method to overcome this is to use quadruple (or higher) precision arithmetic throughout the calculation. However quadruple precision calculations vastly decrease computer speed in solving the problem. The increase in storage space for quadruple precision also means that only smaller matrices can be handled within the active (RAM) memory of the computer. One method to overcome this problem is to solve the same problem with successive increases in spring stiffnesses. The results will tend to converge with increasing spring stiffnesses until the matrix becomes ill-conditioned and the solution becomes significantly (orders of magnitude) different to the previous step. This process of selecting the spring stiffnesses has to be repeated for different discretizations since the relative stiffnesses of the structural elements and axial springs change. It is probable that this problem can be overcome using methods such as Lagrange constraints, but this requires significant reformulation of the solution method and is left for future development of the method.

5.5 Example Problems

The newly developed method described in this chapter is used to solve two classical fracture mechanics problems. The first problem deals with a central crack in a finite width strip. This open crack problem uses the QDD method to model the exterior plate and the DDT to model the internal crack. The second example problem analysis a subsurface crack in a half plane subjected to a moving point load. The second problem has been extensively studied [Hearle and Johnson, 1985, Chang *et al.*, 1984 and Komvopolous, 1996) because of the interest in rolling contact fatigue failure.

5.5.1 *Example Problem 1 - Open Crack Problem*

Consider a finite width strip with a centrally located crack subjected to a remote tensile stress as shown in Figure 5.6.

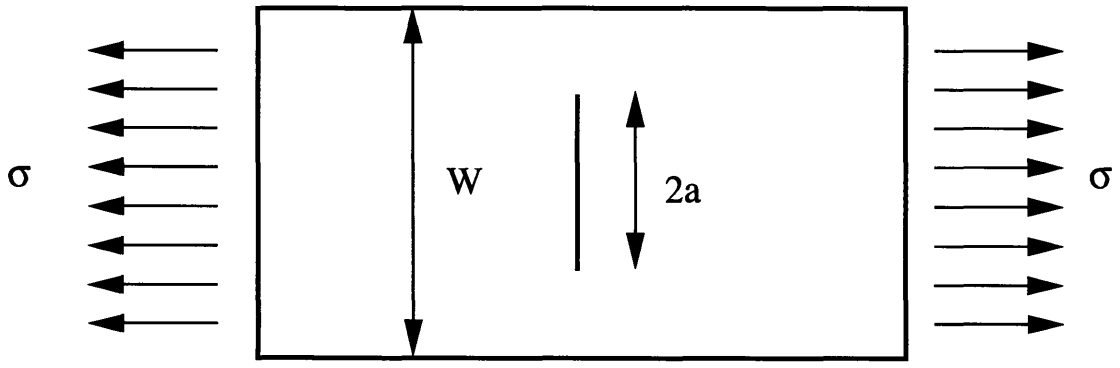

Figure 5.6: A cracked tension strip with crack length ($2a$) and width (W)

Since the analyzed crack is straight and horizontal, Equations 5.11 and 5.12 can be further simplified by setting $y=0$ for G_{ijk} in Appendix B. The normal ($N(x)$) and shear ($S(x)$) tractions are then given by:

$$N(x) = 2\frac{\mu}{\pi(\kappa+1)}\int_{-a}^{a}\frac{B_y(\xi)}{x-\xi}d\xi \text{ and } S(x) = 2\frac{\mu}{\pi(\kappa+1)}\int_{-a}^{a}\frac{B_x(\xi)}{x-\xi}d\xi \tag{5.22}$$

When Equations 5.22 are normalized over the interval [-1,+1] and $s=\xi/a$, it can be shown (Hills *et al.*, 1996) that the function $B_k(\xi)$ can be rewritten as

$$B_k(s) = \frac{\phi_k(s)}{\sqrt{1-s^2}} \tag{5.23}$$

Gauss-Chebyshev quadrature gives:

$$N(t_k) = 2\frac{\mu}{\pi(\kappa+1)}\frac{1}{N}\sum_{i=1}^{N}\frac{\phi_y(s_i)}{t_k-s_i} \tag{5.24}$$

$$S(t_k) = 2\frac{\mu}{\pi(\kappa+1)}\frac{1}{N}\sum_{i=1}^{N}\frac{\phi_x(s_i)}{t_k-s_i} \tag{5.25}$$

where N is the number of integration points, $s_i = \cos\left(\pi\frac{2i-1}{2N}\right)$ are the integration points ($i=1..N$), $t_k = \cos\left(\frac{\pi k}{N}\right)$ are the collocation points ($k=1..N-1$). In order to solve the system of equations 5.22 and 5.23 for the unknowns $\phi_x(s_i)$ and $\phi_y(s_i)$, two further equations are needed.

$$\int_{-a}^{a}B_x(\xi)d\xi = \frac{\pi}{N}\sum_{i=1}^{N}\phi_x(s_i) = 0 \tag{5.26}$$

$$\int_{-a}^{a}B_y(\xi)d\xi = \frac{\pi}{N}\sum_{i=1}^{N}\phi_y(s_i) = 0 \tag{5.27}$$

Equations 5.26 and 5.27 are known as the side conditions and are obtained from the requirement that the crack faces meet at both ends. After Equations 5.24 to 5.27 are solved, the stress intensity factor (SIF) at the crack ends can be calculated using (see Hills *et al.* 1996)

$$K_I(\pm a) = \pm 2\sqrt{\pi a}\frac{\mu}{\kappa+1}\phi_y(\pm a) \quad \text{and } K_{II}(\pm a) = \pm 2\sqrt{\pi a}\frac{\mu}{\kappa+1}\phi_x(\pm a) \tag{5.28}$$

Since $\phi(\pm a)$ are not explicitly calculated in the solution of Equations 5.22 to 5.25, an extrapolation method must be used. Krenk's extrapolation formulae (Hills *et al.* 1996) is a particularly powerful method for finding $\phi(\pm a)$. Krenk's formula for open cracks is

$$\phi(\pm a) = \frac{1}{N}\sum_{i=1}^{N} \frac{\sin\left[\frac{2i-1}{4N}\pi(2N-1)\right]}{\sin\left[\frac{2i-1}{4N}\pi\right]}\phi_y(s_i) \tag{5.29}$$

Example problem 1 is solved for various crack lengths (a in Figure 5.6). The results for the SIF are compared with $K_I = [\sec(\pi a/W)]^{-1/2}\sigma\sqrt{\pi a}$ given by Feddersen (Edwalds and Wanhill, 1986) and $K_I = [1-(2a/W)^2]^{-1/2}\sigma\sqrt{\pi a}$ given by Dixon (Edwalds and Wanhill, 1986) in Table 5.1. The boundary of the strip are discritized using 40 quadratic displacement discontinuity elements and 30 dislocation density integration points are placed on the crack.

Table 5.1: Comparison of SIF calculations for various methods

a/W	$K_I/(\sigma\sqrt{\pi a})$ Dixon	$K_I/(\sigma\sqrt{\pi a})$ Feddersen	$K_I/(\sigma\sqrt{\pi a})$ Iterative
0.1	1.0206	1.0254	1.0139
0.2	1.0911	1.1118	1.0942
0.25	1.1547	1.1892	1.1689
0.3	1.2500	1.3043	1.2859
0.4	1.6667	1.7989	1.8190

Table 5.1 shows that the iterative technique is within 3% of the analytical solutions. The solution time for the problem on an INDY silicon graphics workstation was 2.23 seconds for the iterative method. In order to assess the speed of this technique, the same problem was solved using a direct quadratic displacement discontinuity (QDD) method to model both the boundaries and crack. In order to obtain the same 3% accuracy as the hybrid technique, the QDD method took 1.89 seconds. When the problem was resolved using double the elements for both methods, the iterative technique required 11.2 seconds while the QDD method required 14.2 seconds. The accuracy of the both hybrid and QDD techniques improve only slightly to 2.5% of the analytical solution when the number of elements are doubled indicating that the solution has converged.

Thus for larger problems, the iterative method is more efficient than the traditional QDD method for solving open crack problems. The iterative technique is faster than the direct approach since it requires the reduction of a smaller matrix (associated with the uncracked body only) than the direct approach (associated with the full cracked body problem).

5.5.2 *Example Problem 2 - partially closed crack problem*

The growth of a crack parallel to a surface undergoing periodic compressive loading is one of the major causes of fatigue damage of riding surfaces. This damage mode has been extensively studied by several authors including the analytical solution of Hearle and Johnson (1985), the DDT technique of Chang *et al.* (1984), and the FEM approach of Komvopolous (1996). In order to verify the iterative boundary element method presented in this chapter, the developed iterative technique is compared with the example problem studied by Komvopolous (1996).

Consider a horizontal subsurface crack of length $2a$ and depth h subjected to a moving point load (P) as shown in Figure 5.7. Depending on the load position (x_p) and crack geometry, various parts of the crack can either undergo forward slip, backward slip, separation or stick as shown in Figure 5.8.

For this example, the crack-to-depth ratio $2a/h$ is equal to 3, the Young's modulus E is $1x10^{11}Nm^{-2}$ and Poisson's ratio ν is 0.3. The top surface of the elastic-half plane is modeled using 100 QDD elements and the crack is modeled using 25 QDD elements. The first and last elements of the elastic half space are placed 4 crack lengths from left and right crack tips. The shear and normal spring stiffnesses (K_s and K_n in equation 5.17) are assumed to be $2x10^{17}Nm^{-1}$. The coefficient of friction (μ) is set equal to 0 and 0.5.

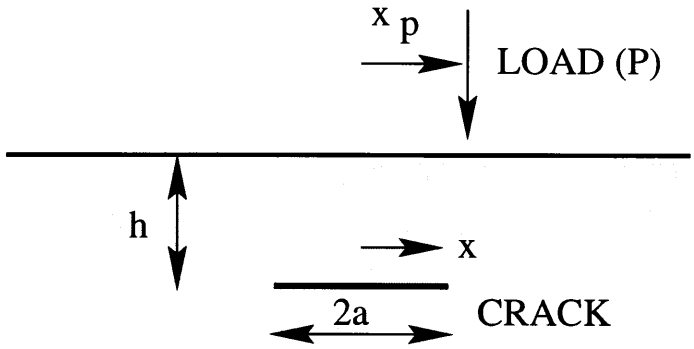

Figure 5.7: A subsurface crack in an elastic half-space subjected to a moving point load

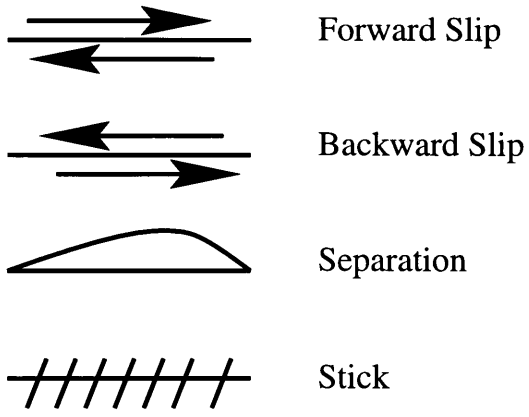

Figure 5.8: The stick, slip and separation modes for a closed crack

The results of the Mode II SIF at the left crack tip and the various modes of crack-opening, closure and stick are compared with the results of Komvopolous (1996). The Mode II SIF is calculated from Zhang and Leech (1986)

$$K_{II} = \frac{\mu}{4(1-\nu)}\sqrt{\frac{2\pi}{r}}D_s^{tip} \tag{5.30}$$

where D_s^{tip} is the near crack-tip shear discontinuity and r is the distance from the crack tip. K_{II} is calculated by taking the average value calculated in Equation 5.30 for the 3 nodes (i.e. the nodes in the first element) closest to the crack tip.

The normalized Mode II SIF $K_{II}/(2P/\pi\sqrt{l})$ for the left crack tip of a frictionless horizontal crack is compared with the analytical solution of Hearle and Johnson (1985) in Figure 5.9.

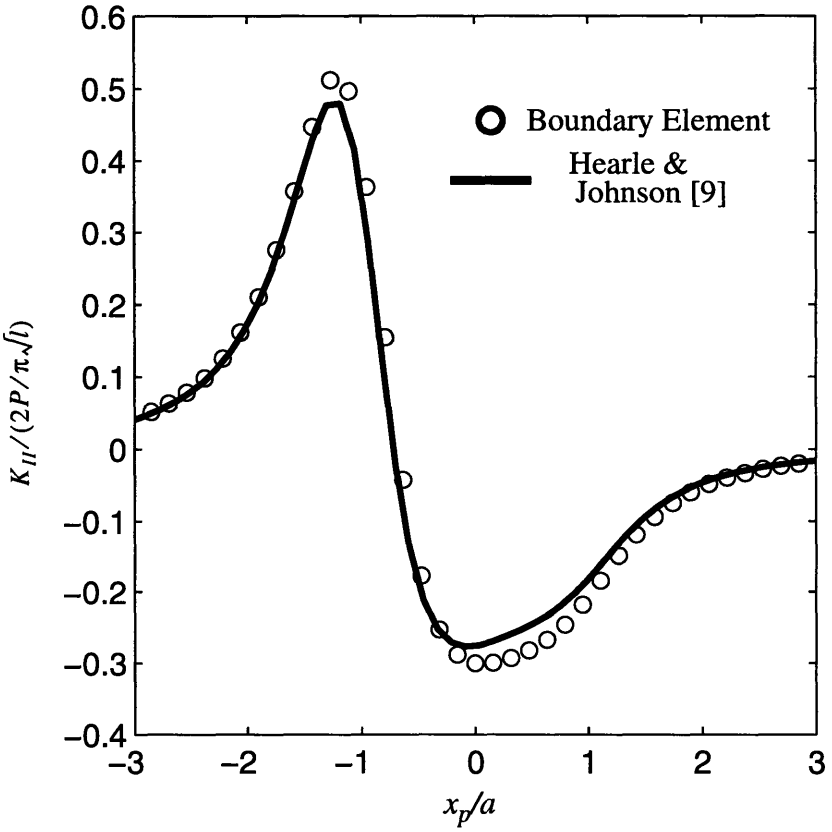

Figure 5.9: Comparison of the analytical and boundary element methods for the left crack-tip mode II SIF for a frictionless subsurface crack under various concentrated point load positions.

The developed iterative boundary element method shows good agreement with the analytical solution. The crack opening and sliding mechanisms for various normalized load positions (x_p/a) are shown in Figure 5.10. The sliding and opening behavior of the crack compares well with the FEM solution of Komvopolous (1996).

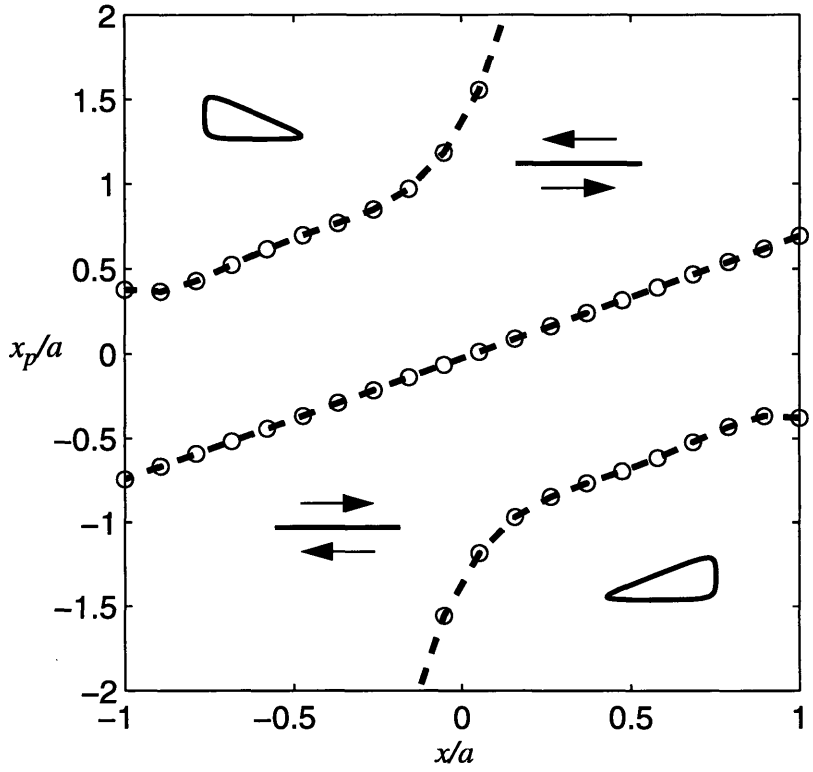

Figure 5.10: Regions of slip and separation for the frictionless subsurface crack under various positions of a concentrated point load.

The mode II SIF for frictionless and frictional contact (μ=0.5) for the left crack tip is shown in Figure 5.11. Figure 5.11 shows that the consequence of frictional contact is to reduce the SIF for all load positions. Figure 5.12 show the various stick, slip and separation zones for various load positions. The results for the frictional contact case compare well with the FEM solution of Komvopolous (1996).

Komvopolous' FEM results at x/a=-1 and x/a=1, however, show stick zones near x_p/a=-2 and x_p/a=2 which do not appear in Figure 5.12. The present analysis is considered correct since the extent of stick zone at these points can be attributed to the assumed contact convergence parameters used by Komvopoulos (1996). Using a similar FEM model, Komvopoulos and Cho (1997) also shows stick at the same locations for deep cracks ($2a/h$=1). These stick-zones are not consistent with Hearle and Johnson's analysis (1985) which show a slip zone since the driving shear force is greater than the frictional resisting force at a deep crack.

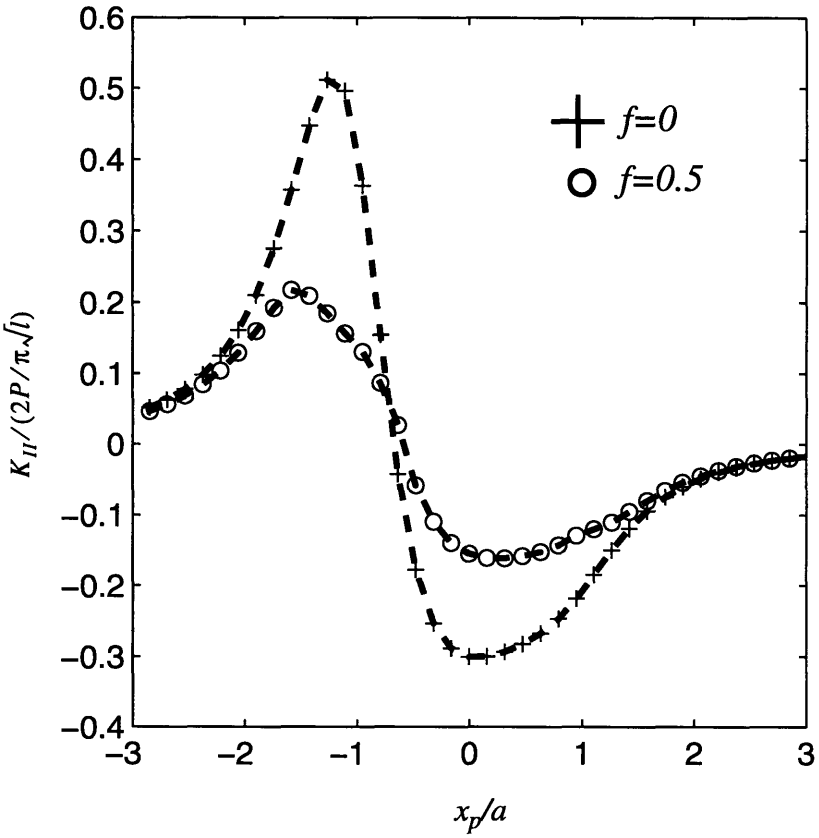

Figure 5.11: Comparison of the mode II SIF for the left crack-tip of a frictionless and frictional subsurface crack under various concentrated point load positions.

In order to illustrate the solution speed of the new iterative approach, the full problem was solved for all loading positions using the same number of quadratic displacement discontinuity elements (100 on the elastic half plane and 25 on the crack) and the solution time was compared with the iterative procedure. The solution time for the full problem on an INDY Silicon Graphics workstation was 2 hours while for the iterative solution was 13 minutes. The vastly improved speed can be attributed to the fact that the exterior problem's geometry remains the same throughout the solution and can be **LU** decomposed

after the first iteration. Subsequent solutions only requires back-substitution for the exterior problem and the full solution of the much smaller interior crack-problem.

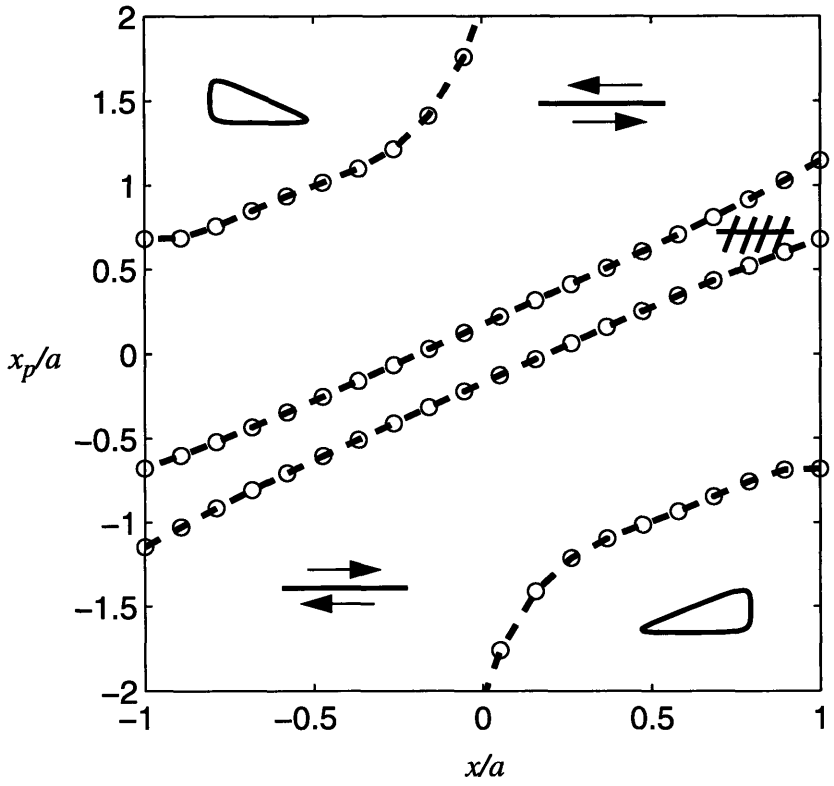

Figure 5.12: Regions of slip, stick and separation for the frictional subsurface crack under various positions of a concentrated point load.

5.6 Discussion of the Iterative Boundary Element Method

The iterative boundary element method has been presented in the previous sections of this chapter and has been applied to the modeling of closed and open cracks. The method of partitioning the problem into two sub-problems consisting of the exterior body without crack and a crack in an infinite domain has been shown to have some significant advantages over other solution methods. These advantages include :

(1) Increased solution speed for large linear elastic (open crack) problems.

(2) Vastly increased speed for closed crack problems which involve load-stepping and iteration.

(3) The two sub-problems are independently formulated and can be solved with different methods leading to a hybrid approach.

(4) The computer matrix-storage space is reduced.

In comparison with the traditional FEM method, Komvopoulos (1996) reports solution times on the order of 2 to 4 hours for the contact example problem discussed in this chap-

ter. This solution time is significantly slower than the 13 minute solution time of the IHBEM.

5.7 Some Aspects of Sensing Closed Cracks

In this chapter, the fiber is assumed to be embedded at depth (s) above the neutral axis of the beam. A schematic representation of beam-layout is shown in Figure 5.13.

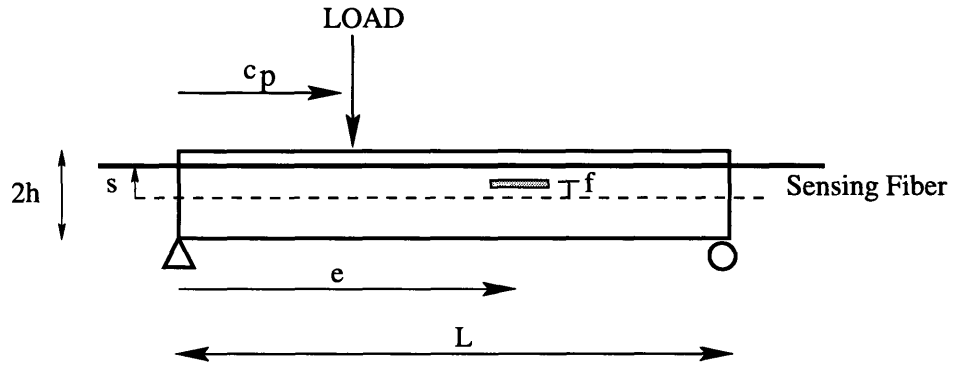

Figure 5.13: The geometry of a damaged, simply supported beam subjected to a moving load.

For an embedded optical fiber interferometer, the opto-mechanical phase change relationship is given by equation 3.18. For an uncracked beam, simple structural mechanics shows that the axial and normal strains (ε_{xx} and ε_{yy} respectively) are given by:

$$\varepsilon_{xx} = \frac{P(L-c_p)xs}{LEI} \quad \text{for } x < c_p$$

$$\varepsilon_{xx} = \frac{P(L-c_p)xs}{LEI} - \frac{P(x-c_p)s}{EI} \quad \text{for } x > c_p \tag{5.31}$$

$$\varepsilon_{yy} = -\nu\varepsilon_{xx} \quad \text{for all } x$$

The strain integrals are given by

$$\int_0^L \varepsilon_{xx}\, dx = \frac{Psc_p(L-c_p)}{2EI} \tag{5.32}$$

$$\int_0^L \varepsilon_{yy}\, dx = -\upsilon \int_0^L \varepsilon_{xx}\, dx \tag{5.33}$$

Substituting equations 5.31 and 5.32 into 3.18 gives

$$\Delta\phi = KsPc_p(L-c_p) \tag{5.34}$$

where K is the calibration coefficient for the sensor and is dependent on the material properties of the beam, the optical properties of the fiber, the geometry of the beam and the

strain transferal from the host material of the beam to the optical fiber. The assumption in Equations 5.30 to 5.33 is that the strain perturbation at any location through the depth of the beam is dominated on the global Bernoulli-Euler bending behavior and ignores effects such as the change in the strains in the fiber due to stress distribution under the point load itself. Timoshenko (article 35. 1934) discusses how the stress distribution directly under a point loaded beam is at first approximation the same as the Flamant solution for a point-load in a semi-infinite domain at any location of the point load along the beam (except very closed to the beam supports). Thus the strains due to the point load do not change with load position and can be assumed to be constant with load position. Thus if the contribution of the point load stresses were to be taken into account, Equation 5.34 would only need to be modified with the addition of a constant.

As seen from the sample calculation in Section 4.6, the phase change due to the bending of the virgin beam are substantially larger (two orders of magnitude) than phase perturbations caused by the damage. Thus the phase perturbation due to damage cannot be easily distinguished from the global bending phase change of the beam. The small perturbations due to damage can only be successfully detected when the fiber is placed in such a way as to cancel the global beam bending effect. For example from Equation 5.34 it can be seen that placing the fiber on the neutral axis ($s=0$) leads to zero global bending phase changes. Further methods of fiber placement to overcome global bending effects are discussed in Section 6.7.2.

This chapter introduces a new method of damage detection which does not rely on accurate fiber placement. Closer inspection of Equation 5.34 shows that the phase change is parabolic. If Equation 5.34 is differentiated twice with respect to load position, the resulting quantity ($\Delta\phi''$) is constant. Thus any non-constant perturbation in $\Delta\phi''$ is directly related to the presence of damage in the beam.

The analyzed simply supported beam shown in Figure 5.13 is assumed to have linear elastic behavior. The beam is assumed to have elastic modulus $E = 2\text{x}10^{11}$ N/m^2 and Poisson's ratio ν=0.3. The optical properties of silica glass are assumed to be the same as in the work of Sirkis and Haslach (1990) which correspond to a red light propagating in a single mode fiber. The Pockel's constants are taken to be P_{11}=0.121 and P_{12}=0.27. The refractive index is n_o=1.456 and the wavelength of light is λ_o=632.8nm.

The IHBEM is used to model the beam and crack. 100 quadratic displacement discontinuity (QDD) elements are used to model the beam boundaries (10 elements through the beam depth and 40 elements on both the beam's top and bottom surface), and 15 QDD elements are used to model the crack.

5.8 Results for Closed Crack Sensing

The effects of crack length ($2a$), crack height (f) and crack-face friction (μ) are studied in this section. Two typical, normalized $\Delta\phi''$ perturbations for various load positions with beam geometry $e=L/2, f=0.5h$, $s=0.6h$, $L/2h=10$ and $2a=2L/20$ are shown in Figure 5.14. In this analysis, the load is assumed to be applied at discrete points along the structure and thus no residual locking is allowed due to the load movement. This loading condition corresponds to applying a load which starts at zero and finished at zero before it is moved to a new position and can be achieved in practise by applying a vibrating force.

Figure 5.14 shows the importance of considering crack closure by comparing the predicted $\Delta\phi''$ for a beam with (a) no damage, (b) no crack-face closure constraints (i.e. the faces of the crack are allowed to interpenetrate) and (c) contact constraint and zero friction. Since in general, the sensor calibration factor K in Equation 5.34 must be determined experimentally, $\Delta\phi''$ is left in arbitrary units (A.U.). $\Delta\phi''$ is calculated by applying the load at discrete points along the beam and calculating the $\Delta\phi$ integral given by Equation 3.18. Once the phase change ($\Delta\phi$) at the discrete points have been calculated, a spline is fitted to the data and $\Delta\phi''$ is calculated using the central difference method.

Figure 5.14 shows that for the undamaged beam, $\Delta\phi''$ is essentially constant as can be predicted from simple beam theory. For both assumed crack contact conditions, the axial position of the crack leading and trailing edges (x_l and x_t) occur at the minimum of $\Delta\phi''$. The crack's axial position (e) and length $2a$ can then be easily predicted from:

$$e = (x_t + x_l)/2 \tag{5.35}$$

$$2a = x_l - x_t$$

Figure 5.14 also shows that neglecting the contact conditions at the crack face can severely over-predict the magnitude of the measured $\Delta\phi''$. Furthermore, the actual shape of the load position versus $\Delta\phi''$ curve for a crack with contact can be significantly different from a crack in which contact is ignored.

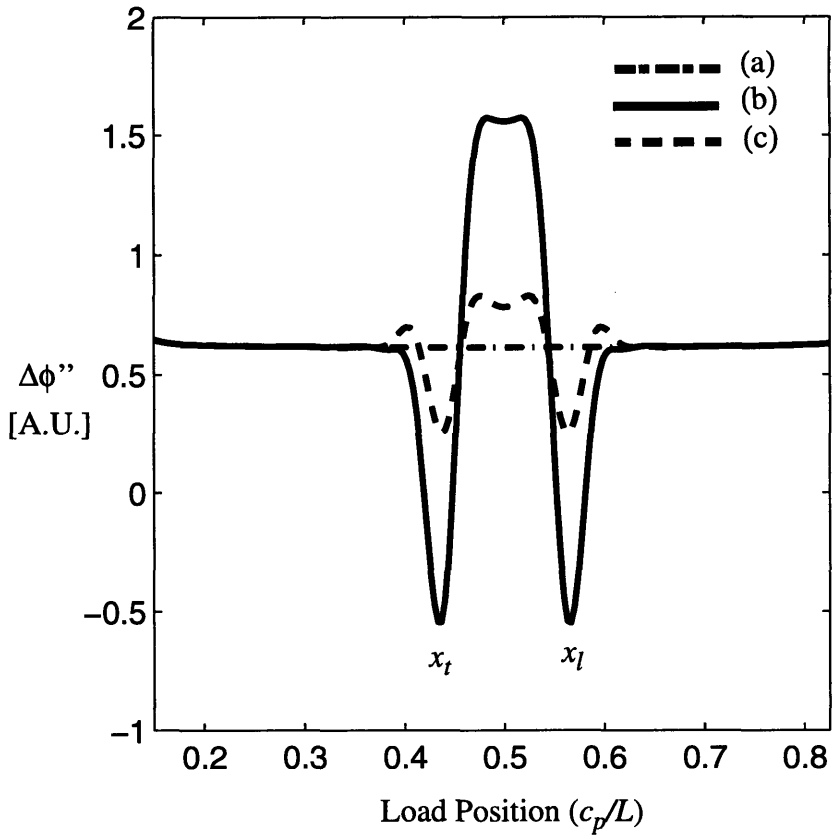

Figure 5.14: Comparison of $\Delta\phi$" for a (a) undamaged beam, (b) beam with damage and no contact constraint and (c) beam with damage and frictionless contact constraint. The crack position is at $f=0.5h$, the sensor position is at $s=0.6h$ and the crack length is $2a=2L/20$.

The extent of crack stick, slip and separation are strongly dependent on crack depth and length (Komvopoulos, 1997). Since crack opening mechanisms can change abruptly due to crack geometry , the effect of representative crack depths and lengths are studied in this chapter. Figure 5.15 shows the effect on $\Delta\phi$" for crack lengths of (a) $2a=3L/20$, (b) $2a=2L/20$ and (c) $2a=L/20$. As in Figure 5.14, Figure 5.15 shows that the position of $\Delta\phi$" minimum corresponds to axial position of trailing and leading edges of the crack (x_{ta} to x_{tc} and x_{la} to x_{lc}). Equations 5.34 can thus be used to determine the axial position and extent of the crack.

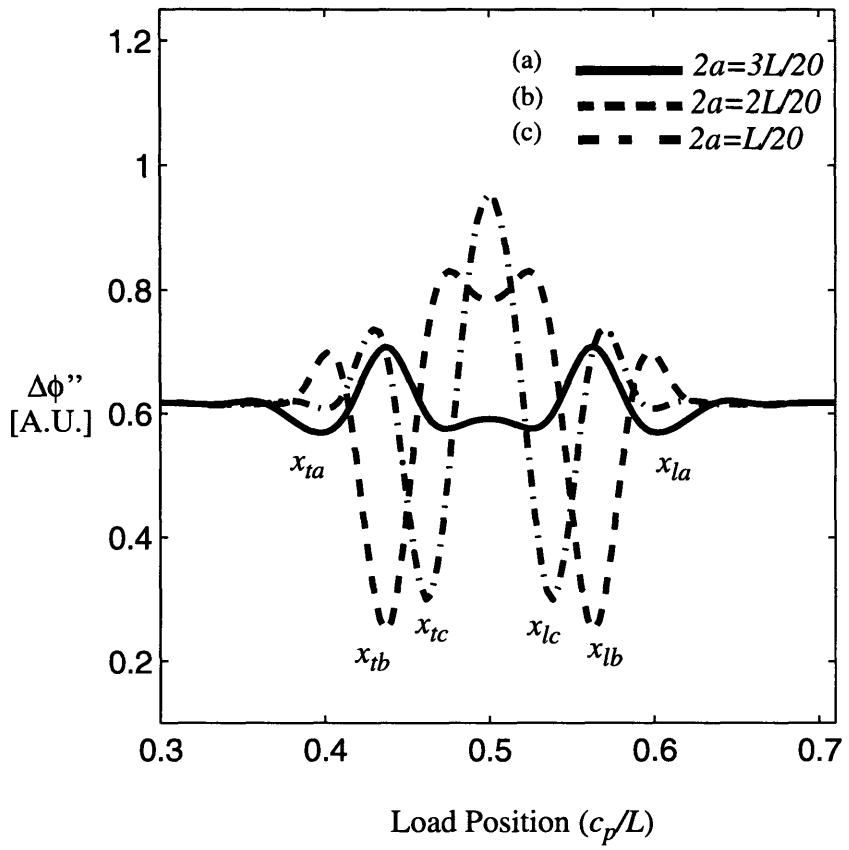

Figure 5.15: Comparison of Δϕ" for a simply supported frictionless crack with cracks of length (a) *2a=3L/20*, (b) *2a=2L/20* and (c) *2a=L/20*. Crack position at *f=0.5h* and sensor position at *s=0.6h*.

The variation of Δϕ" with cracks at depth *f=0.5h*, *f=0.4h* and *f=0.3h* and constant crack length of *2a=2L/20* and sensor position *s=0.6h* are shown in Figure 5.16. Figure 5.16 shows that though the positions of Δϕ" minimum remains the same, the perturbation to the Δϕ" signal from the virgin (constant) state decreases with increasing crack distance from the sensor. The decrease in the Δϕ" perturbation is non-linear with depth and decreases rapidly with crack distance from the sensor. Due to the small perturbation signal, multiple embedded sensors through-out the depth of the beam are needed to accurately locate the crack.

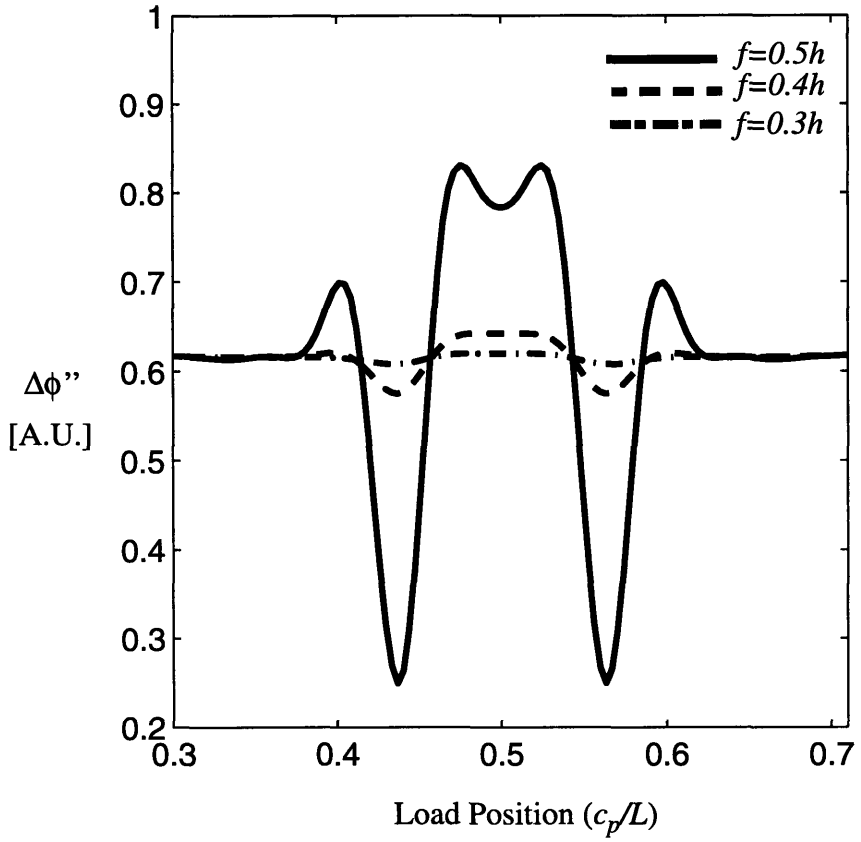

Figure 5.16: Comparison of $\Delta\phi$" for a simply supported cracked frictionless beam with crack depths at $f=0.5h$, $f=0.4h$ and $f=0.3h$. Crack length is $2a=2L/20$ and sensor position $s=0.6h$.

Figure 5.17 shows the variation of $\Delta\phi$" for $f=0.4h$ and $f=0.3h$ for 2 sensors, embedded at $s=0.6h$ and $s=0.5h$. The magnitude of the perturbation of $\Delta\phi$" is greater for the sensor embedded at $s=0.5h$, which is the sensor closest to the crack. Figure 5.17 also shows that the position of the $\Delta\phi$" minimums do not change with sensor position which is consistent with Equation 5.35.

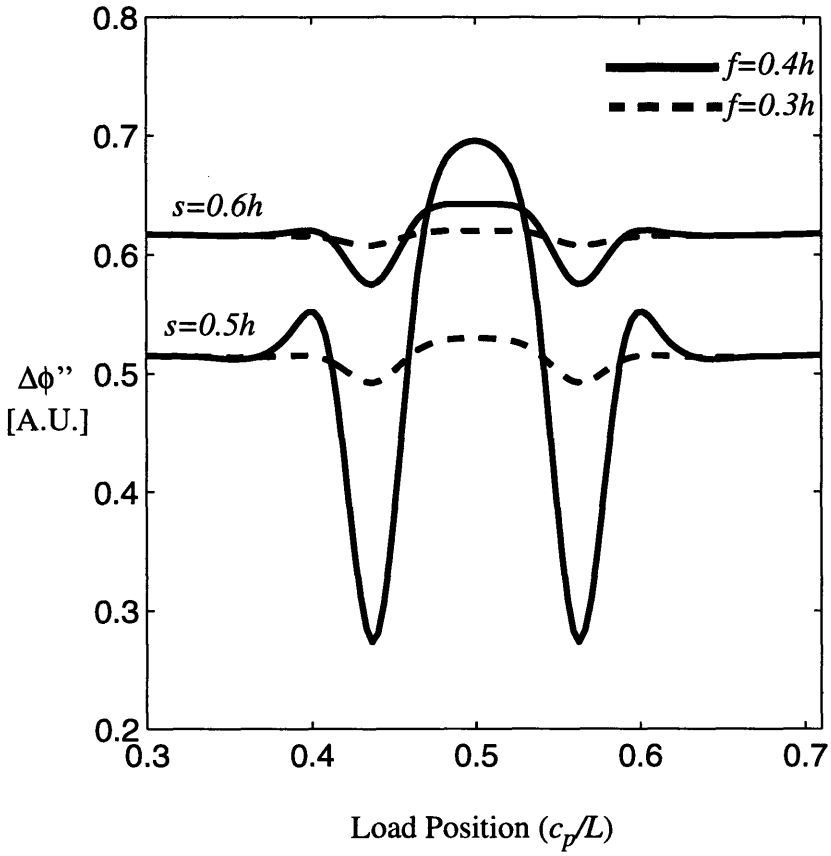

Figure 5.17: Comparison of Δϕ" for frictionless cracks at depths *f=0.4h* and *f=0.3h* and sensor position of *s=0.6h* and *s=0.5h*. Crack length is *2a=2L/20*.

The effect of crack face friction (μ=*0*, μ=*0.25* and μ=*0.5*) is shown in Figure 5.18. The crack position is at *f=0.5h*, sensor position at *s=0.6h* and crack length *2a=2L/20*. Figure 5.18 shows that the effect of increasing coefficient of friction is to decrease the magnitude of the Δϕ" perturbation.

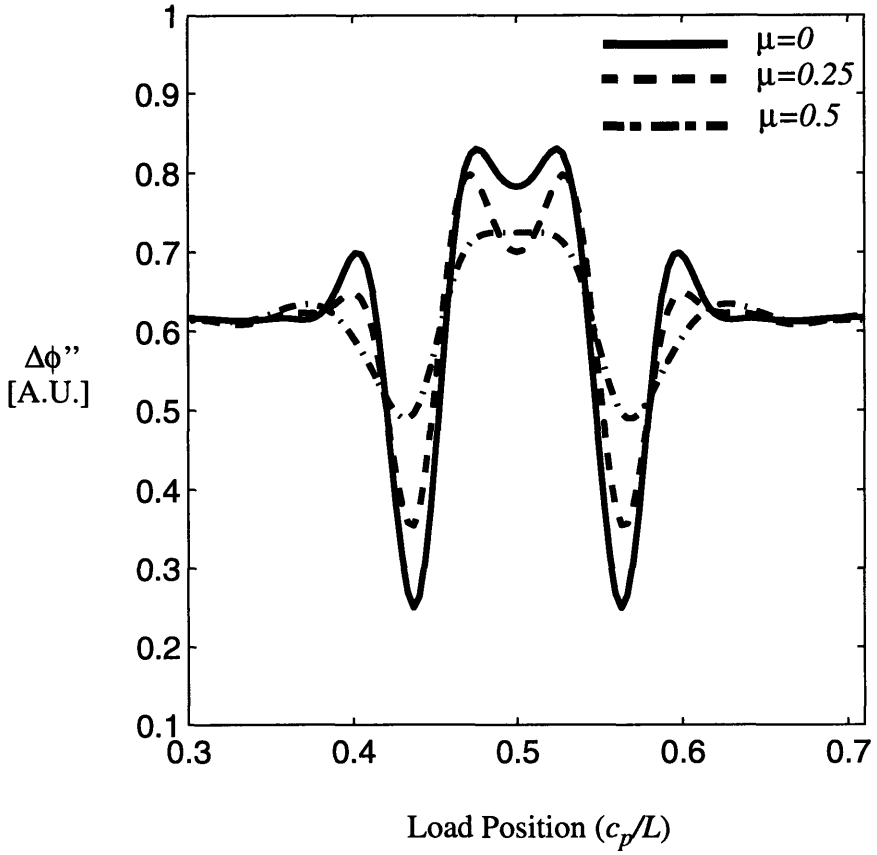

Figure 5.18: Effect of friction ($\mu=0$, $\mu=0.25$ and $\mu=0.5$) on $\Delta\phi$" for a closed crack of length $2a=2L/20$. Sensor position at $s=0.6h$ and crack depth $f=0.5h$.

5.9 Effect of Crack Opening Mechanisms

In general prediction of closed crack behavior is difficult because of the various mechanisms of stick, slip and separation that can occur. These crack-face mechanisms are dependent on material properties of the beam, the load-position, crack-position and crack length. As an illustrative example of the effect of various mechanisms on crack behavior, only the effect of crack length is studied in this section. Generally it is easier to understand the physical meaning of the phase change ($\Delta\phi$) than the second derivative of the phase change ($\Delta\phi$"). Since the phase change due to the crack is much smaller than the phase change due to the beam bending, in this discussion we will only consider the phase perturbation due to damage alone ($\Delta\phi_c$) by subtracting the phase change due to the global beam bending ($\Delta\phi_v$) from the overall phase change ($\Delta\phi$) *i.e.* $\Delta\phi_c=\Delta\phi-\Delta\phi_v$.

The effect of four different frictionless crack lengths ($2a=4L/20$, $2a=3L/20$, $2a=2L/20$ and $2a=L/20$) on the phase perturbation ($\Delta\phi_c$) are plotted in Figure 5.19. Figure 5.19 is in direct contrast to the results of Chapter 4, which showed that for open cracks, the shape of the phase perturbations are similar with both peak value and position of local minimum increasing with increasing crack length.

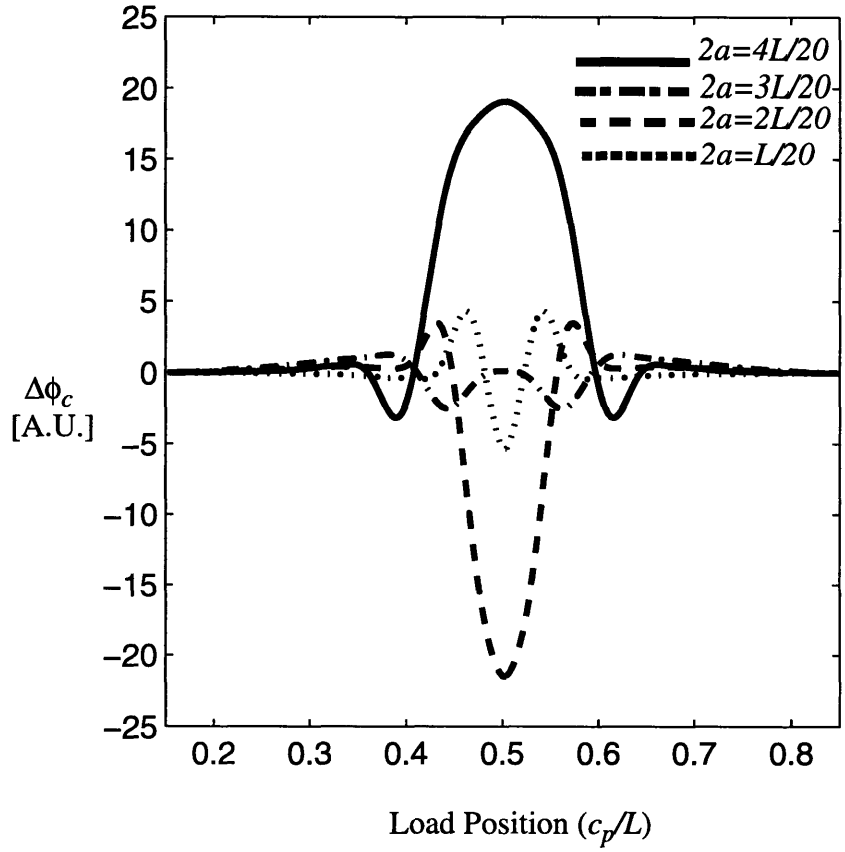

Figure 5.19: The effect of crack length (*2a=4L/20*, *2a=3L/20*, *2a=2L/20* and *2a=L/20*) on the phase perturbation $\Delta\phi_c$ for a frictionless crack. Crack depth is at *f=0.5h*. Sensor position is at *s=0.6h*.

Figure 5.19 shows that the shape of each phase perturbation ($\Delta\phi_c$) curve is unique for the particular crack length. This behavior can be attributed to the fact that the mechanisms on the crack face change with increasing crack length.

Figure 5.20 shows the crack face mechanisms acting on the various lengths of closed cracks for the load over the crack center. For crack lengths shorter than *2a=3L/20*, the crack is closed along it entire length with symmetrical regions of backward and forward slip occurring about the crack center-line. For cracks longer than *2a=3L/20*, separation occurs at the crack tips. The change in crack-face mechanisms can also be seen in the phase perturbation curves ($\Delta\phi_c$) in Figure 5.19. The $\Delta\phi_c$ curves for crack lengths shorter than *2a=3L/20*, decrease over the crack center *(c/L=0.5)* while for cracks longer than *2a=3L/20*, the curves increase over the crack center.

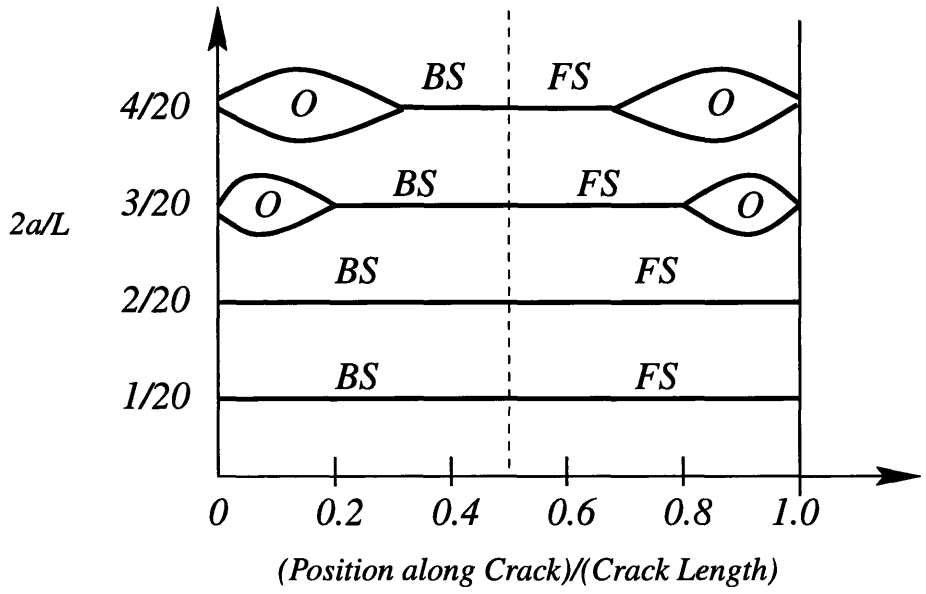

Figure 5.20: Crack face mechanisms for a frictionless crack of lengths (*2a=4L/20, 2a=3L/20, 2a=2L/20* and *2a=L/20*). Crack depth *f=0.5h* and sensor position is at *s=0.6h*. Load position is over the center of the crack (*c=L/2*). *O* indicates crack separation, *BS* indicates backwards slip, *FS* indicates forward slip.

The effect of introducing friction along the crack face can be seen in Figures 5.21 and 5.22. The phase perturbation curves for a crack length of *2a=3L/20* and friction coefficients of $\mu=0$, $\mu=0.25$ and $\mu=0.5$ for a centrally loaded beam are shown in Figure 5.21. The change in the phase perturbation ($\Delta\phi_c$) with friction coefficient (μ) can be attributed to an increase of the stick zone at the center of the crack as shown in Figure 5.10.

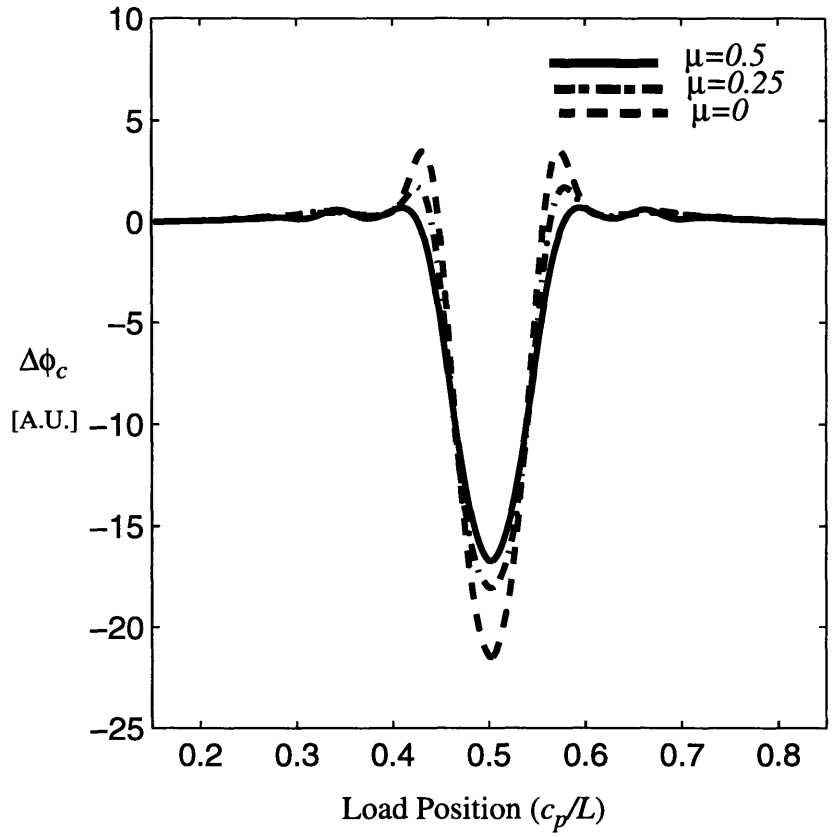

Figure 5.21: The effect of coefficient of friction ($\mu=0$, $\mu=0.25$ and $\mu=0.5$) on phase perturbation $\Delta\phi_c$. Crack Length $2a=2L/20$ and sensor position at $s=0.6h$.

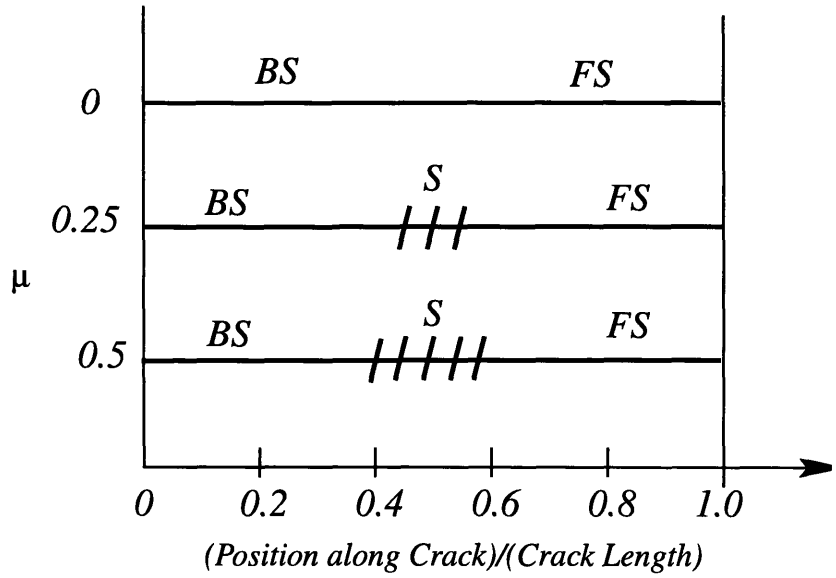

Figure 5.22: Crack face mechanisms for a crack of length $2a=2L/20$ with friction ($\mu=0$, $\mu=0.25$ and $\mu=0.5$). Crack depth $f=0.5h$, sensor depth $s=0.6h$ and load position $c=L/2$. *S* indicates stick.

Figures 5.19 to 5.21 show that the phase perturbation is significantly influenced by the crack opening mechanisms.

5.10 Implication to Closed Damage Detection in Practice

The theoretical work presented in the previous chapter has shown that for accurate location of open cracks, sensitivity of 4.5 radians in phase perturbation is needed. Though chapter 4 dealt with a surface mounted fiber, for comparison's sake the same strain transfer parameters are assumed for the embedded fiber. Figure 5.23 shows the relative expected phase perturbation magnitude for an open and closed crack for the same case as shown in Figure 5.14. The phase change magnitude for the open crack is approximately an order of magnitude greater than for the closed crack.

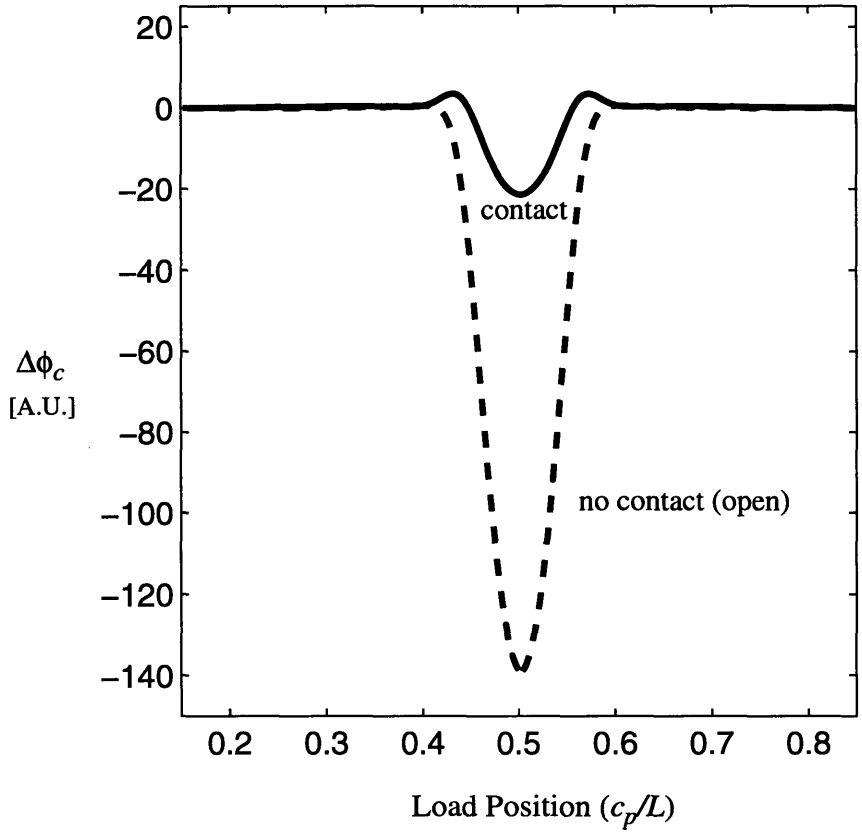

Figure 5.23: Phase perturbation ($\Delta\phi_c$) for the case of a crack with no contact constraint and with contact constraint. The same parameters as in Figure 5.2 apply.

5.11 Conclusions

This chapter has introduced a highly efficient iterative boundary element method for solving closed crack problems. The newly developed method has been used to show the theoretical feasibility of using a novel fiber-optic based technique for detecting both the location and size of subsurface closed cracks with friction. The phase perturbation for closed cracks, can be expected to be an order of magnitude smaller than for open cracks. The work in this chapter has also shown that the second derivative of the phase change with respect to load position can successfully eliminate the large phase change due to global beam bending with the resulting signal only being sensitive to damage. Detection sensitivity drops rapidly with distance between the fiber and damage and thus multiple fibers through the depth of the structure are needed to accurately determine the depth position of the damage.

Chapter 6

EXPERIMENTAL VERIFICATION

6.1 Introduction

A detailed description of the experimental performance of the novel fiber optic damage detection method are given in this chapter. The goal of the experimental work is to, (a) study the feasibility of the proposed detection method, (b) highlight the practical aspects of fiber-optic damage detection, and (c) provide sensor calibration. The two open damage cases (simply supported and elastically supported beam) studied in the theoretical feasibility section (Chapter 4) of this thesis are considered in this chapter.

6.2 Detailed Experimental Layout Description

A more detailed description of the closed loop interferometer as shown in Figure 3.9 is presented in this section. The experiment can be broadly divided into three parts, namely (i) the optical, (ii) the electrical, and (iii) the mechanical.

A single mode He-Ne laser is chosen because of its good coherence length as discussed in Section 3.8.1. A spherical lens which is mounted onto a translational stage couples the light into a single mode Dow-Corning PS901 Flex 633 step-index optical fiber. The fiber used was not polarization preserving. The correct polarization was maintained by twisting the reference fiber. A Gould 2x2 50-50 coupler is used to split the light into the reference and sensing arms. A Gould 2x2 coupler is used to recombine the light from the reference and sensing fibers. The output of one of the coupler's legs is monitored using a PIN photodetector.

The electrical components include the modulator, demodulator, servo and data-acquisition system. The phase transducer consisted of a 3 inch PZT E-63 Cylinder (EDO Corporation, New York) and 10 fiber windings of the reference arm fiber attached to it with epoxy as shown in Figure 6.1

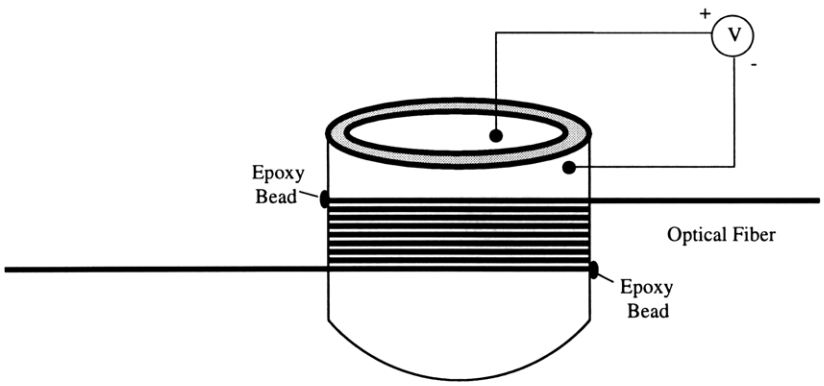

Figure 6.1: PZT cylinder phase transducer

Modulation and de-modulation is done by a standard lock-in amplifier. The modulation frequency is chosen at 45 kHz where the noise in the light is close to the shot noise limit. The shot noise limit for the laser is checked by detecting the laser output with the photodiode. The output from the photodiode was passed into a spectrum analyzer. The point on the light-intensity frequency spectrum at which the noise intensity began to flatten out was at 10 kHz. This intensity noise was close to the photon shot noise limit calculated in Section 3.6.

The servo consists of an electronic integration circuit to achieve high gain at low frequencies with supporting reset circuitry. The saturation level of the integrator is ±15 volts. The dynamic range of the phase transducer is measured to be ±5.5 fringes. In order to avoid saturation of the servo integrator, a reset circuit is provided. Since the servo needs to track the fringe maximum, the servo needs to be reset at an integral number of fringes. The reset circuit is calibrated so that the servo-output is zeroed at ±5 fringes (the largest integral value smaller than the dynamic range of the servo) which corresponds to 13.6 volts. The servo output is stored on a personal computer and the phase change is simply post-processed and added to the previously stored value after reset occurs. (All electronic components were custom built by Stephen P. Smith and V.K. Sudarshanam of the Quantum Optics and Photonics Group at MIT).

6.3 Sensor Output with Zero Applied Load

A typical calibrated sensor output for zero applied load and averaging time τ=1/100 seconds, for about 1 minute is shown in Figure 6.2. The variation in sensor output around 0.01 rads is due to environmental drift effects caused by differential temperature, creep and structural vibration strain between the sensing arm and reference arm of the fiber. Environmental drift affects all strain sensors and can lead to unreliable sensor performance since the sensor cannot discriminate between phase change due to applied load and the phase change caused by the drift.

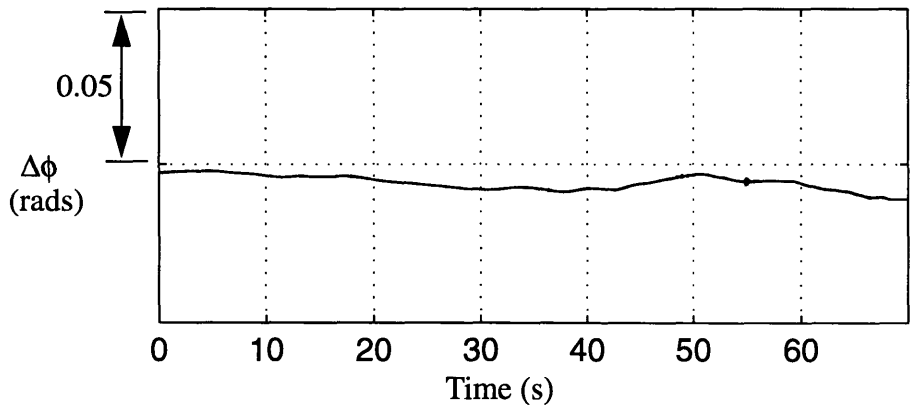

Figure 6.2: Typical sensor output with no applied load and averaging time τ=1/100 sec, showing environmental drift

Closer investigation of Figure 6.2 shows that the environmental drift is dominated by low frequency components mostly caused by slow temperature fluctuations between the sensor and reference arms. Taking the numerical fourier transform of the sensor output in Figure 6.2, gives the frequency spectrum of the environmental drift as shown in Figure 6.3. Figure 6.3 shows that for frequencies greater than approximately 5 Hz the environmental drift effects are three orders of magnitude smaller than the low frequency components. Investigation of the sensor output over several days in the laboratory showed that the environmental drift does not vary by more than ± 0.1 rads per hour of observation because of the controlled laboratory environment. The environmental drift drops off with frequency, and is $\pm 1 \times 10^{-4}$ rads at 5Hz.

In Section 4.6 it has been shown that the theoretical phase change caused by open subsurface damage is on the order of 4 rads at the peak. For adequate resolution of the features of the phase change signal, one may assume that a 0.2 rad measurement accuracy is needed. If one compares the 0.1 rad environmental drift magnitude to the required 0.2 rad measurement resolution, one obtains a phase perturbation to the environmental drift ratio of 2 for slow (near static) load applications, and 2×10^3 for frequencies greater than 5Hz. Note that the 4 rads phase change is for the particular loading configuration and damage size that was studied in Section 4.6. It should also be noted that relative ratio of the phase perturbation to the environmental drift is dependent on the actual load magnitude that can be applied at the load modulation frequency which could be significantly smaller than the 200 N load applied in the example discussed in Section 4.6.

For other structural configurations and load magnitudes, the phase change (and hence the required resolution) is likely to be different.

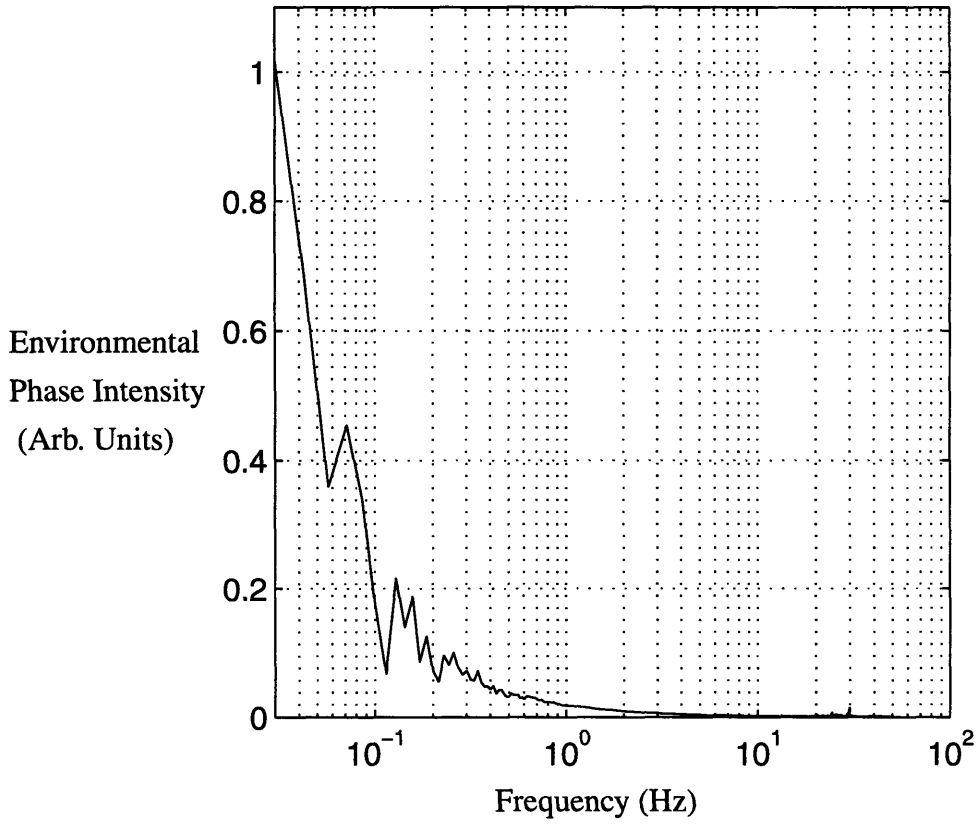

Figure 6.3: Environmental phase intensity spectrum for an unloaded beam.

6.4 Load Application and Sensor Performance

The previous section has shown that for nearly statically applied loads, the signal (due to the phase perturbations caused by the crack) to noise (caused by the environmental drift) ratio is 2. For this signal to noise ratio, the sensor output cannot be unambiguously resolved from the environmental drift. Several methods (or combinations thereof) are presented here in order to overcome this problem. The first method is to apply a load with a dominant frequency of 5 Hz to discrete points along the damaged member. Monitoring the sensor output at 5 Hz limits the environmental noise components to less than 1×10^{-4} rads. A sample output of the sensor and load cell with a peak-to-peak amplitude of 20 N and a frequency of 5 Hz applied to the elastically supported beam is shown in Figure 6.4,

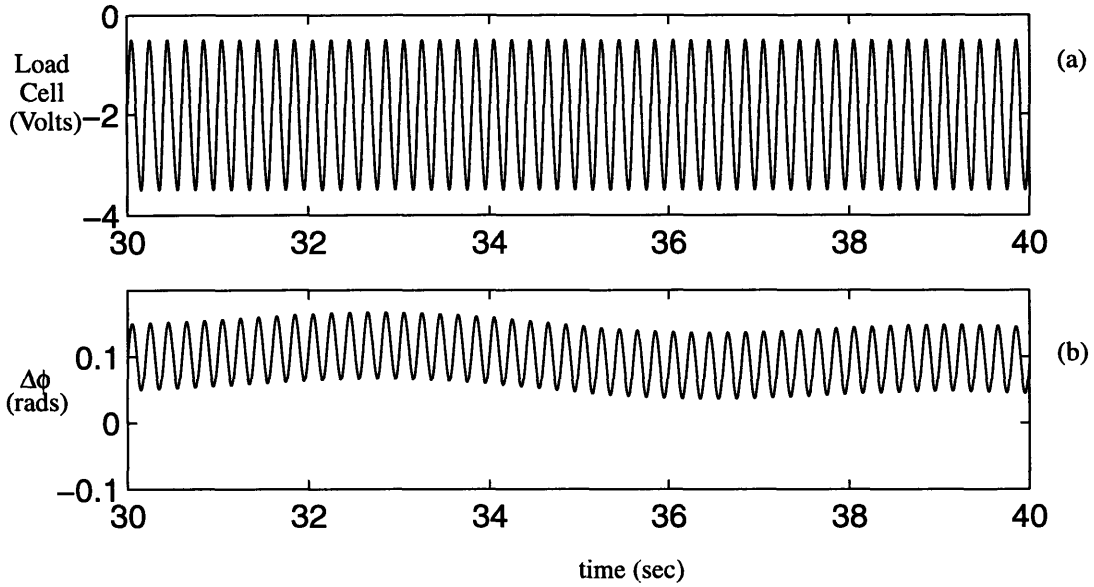

Figure 6.4: (a) Load cell and (b) sensor output for a harmonically applied load at frequency 5 Hz and peak-to-peak magnitude of 20N (1 volt on the Load Cell = 8N) (averaging time τ=1/100 sec)

In order to obtain the sensor output due to the applied load only, the sensor and load data is passed through a 4th order elliptical bandpass filter (4.9 to 5.1 Hz bandpass) (See MATLAB Signal Processing Toolbox) . Figure 6.5 shows the data presented in Figure 6.4 after numerical low pass filtering. It is evident that the drift and D.C. off-set of the sensor has been eliminated and that the time history of the filtered sensor output accurately matches the applied load.

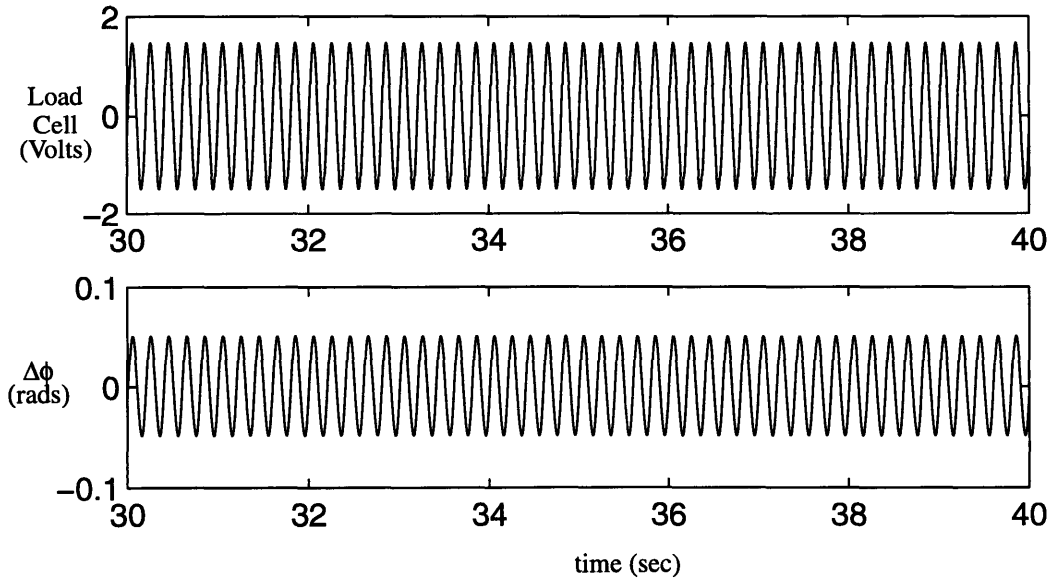

Figure 6.5: (a) Load cell and (b) sensor output after a 5Hz numerical bandpass filtering

The second method of overcoming drift, consists of applying a moving load to the member at a high velocity. Figure 6.3 shows that the environmental drift is dominated by frequencies with periods greater than 30 second (corresponding to 0.033 Hz). Since under laboratory conditions, the drift is of the order of 0.1 rads, a 2 second test could have a maximum drift induced error of 0.04 rads assuming the drift variation to be sinusoidal. Since the test has to be completed over a brief period of time, these testing speeds might not be practical for all structures

The third method consists of time averaging the sensor output over many loading cycles. The performance of this method is strongly dependent on the length of the load cycle and the number of tests performed. This method can also prove to be time consuming and tedious for practical structural inspection.

The load application method used in this experiment is discussed in the following section.

6.5 Mechanical System Description

A schematic of the mechanical layout of the experiment is shown in Figure 6.6. A model-train rail is mounted on rigid supports above the tested specimen. The testing cart is attached to a motor with a winding drum which moves the testing cart across the rail. The load applied to the tested specimen is measured through a load cell which is attached to a computer based data-acquisition system.

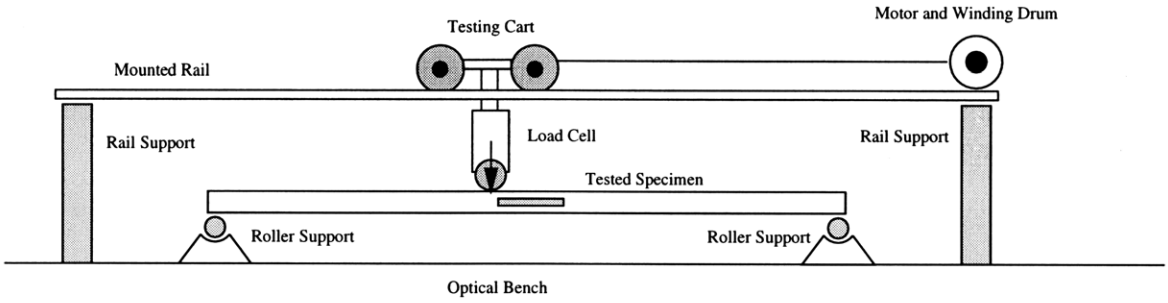

Figure 6.6: Layout of mechanical system used for moving load test

A detailed schematic of the testing cart is shown in Figure 6.7. The position of the load application point is monitored by measuring the voltage change across a rheostat made from high resistance Nickel-Titanium wire which is in sliding contact with the testing cart. In the case of the 5 Hz sinusoidal load application, a PZT actuator driven at 5Hz is attached to the test-cart as shown in Figure 6.7. The actual load applied to the test structure is monitored by the load cell which is attached to a computer data-acquisition system. In the 5Hz load application, the test cart is moved to a fixed position along the beam before the load is applied. After the discrete point is tested, the testing cart is moved to a new discrete position along the beam length.

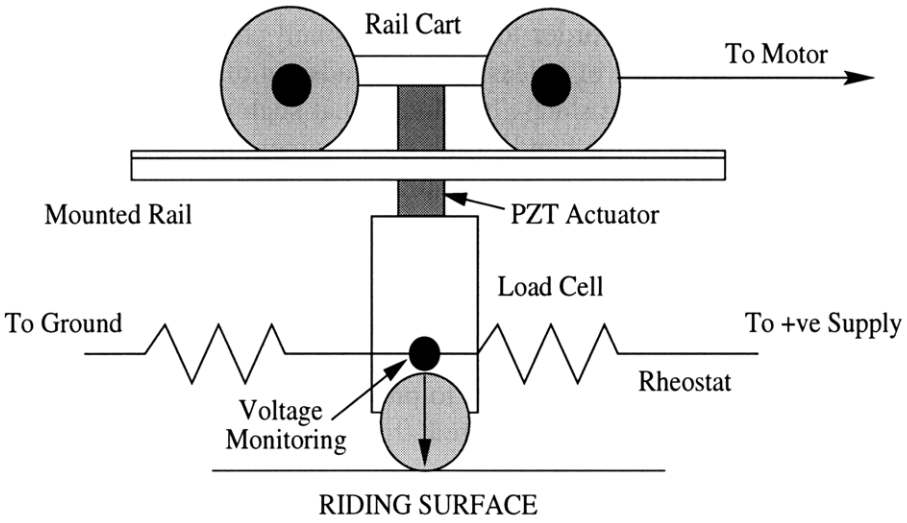

Figure 6.7: Detailed Schematic of Mechanical Testing Cart

In order to prevent direct contact between the sensor and load, the sensor is attached to the center of the beam (along the width), the point load contact with the structure is made with two wheels which pass over the sensor. The load applied to the structure is due to the variation in prescribed deflection given to the beam as the fixed mounted rail is positioned in such a way as to provide initial deformation to the beam. Since the amount of deflection changes with load position due to the flexibility of the structure, the load-cell is needed to monitor the applied load to the structure.

6.5.1 *Beam Preparation*

Four, 0.6 meter long, 12.5 mm deep and 15 cm wide Plexiglass beams were cut from the same plexiglass sheet. A nearly rectangular damage zone of 2.5 mm height and lengths of (i) 25 mm, (ii) 50 mm and (iii) 75 mm were introduced at mid-length and mid-depth of three beams by water jet cutting. For the simply supported beams, mechanical rollers which allowed for free rotation and axial sliding were used as supports. The beam on the elastic foundation was simulated by foam-taping the Plexiglass beams to an optical table. For the simply supported beam, the beam was positioned so that it was supported over 0.4 meters of its length and the damage position was at quarter span.

6.5.2 *Fiber Attachment to Structure*

The method of attachment of the fiber to the structure must be chosen as a consequence of the expected overall behavior of the structure. For the elastically supported beam shown in Figure 4.5, the global integrated bending strain is of the same order of magnitude as the integrated perturbation strain due damage. For such a case, a single fiber attached to the top surface will work. However, the theoretical results that for a simply supported beam show that the surface strains are dominated by the global bending of the beam. The local differential strains associated with the damage zone are 2 orders of magnitude smaller than the global bending strains. For example, in order to measure a 4 radian path length change due to the damage, a 700 radian global strain would need to be

measured (as is discussed in Section 4.6.) The problem with this measurement is that the phase perturbation due to the damage cannot be easily discerned from the global bending behavior of the beam i.e. in order to detect the small changes to the total phase change caused by bending, accuracy of at least 0.5% (4 rads out of 700 rads) is needed to measure the undamaged and damaged states. It is likely that such precise and consistent measurement will fall within the error band of the measurement as the structure undergoes periodic inspection over prolonged periods of time.

In order to overcome this problem, the sensing fiber arm was attached to both the top and bottom surfaces of the beam as shown in Figure 6.8. The optical path length shortening due to the global compressive strains on the top surface are cancelled by the optical path length increase on the tension side. The difference between the two path lengths is the local effect of the damage. In order to prevent compression of the bottom fiber at the support, the supports were manufactured from two separate pieces and the fiber was passed between them.

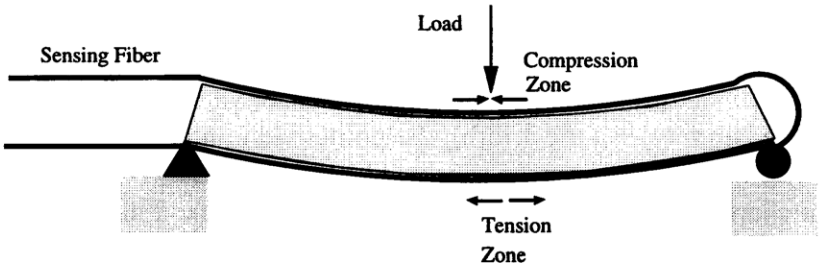

Figure 6.8: Geometric layout of sensing fiber for the simply supported beam

In all cases, the fiber is attached with 3-M Scotch tape to the plexiglass beams. Scotch tape provides some advantages over the traditional epoxy attachment including (i) the same sensor can be re-used for surface measurements of multiple specimens without having to rebuild the sensor, (ii) alignment mistakes during attachment of the sensor can be easily and quickly corrected, and (iii) the tested specimen is not modified with epoxy and can be used for multiple boundary condition testing. The reference arm is attached to an unloaded beam and is not changed for various tested beams.

6.6 Experimental Results

The theoretical and experimental results for various damage lengths are presented for simply supported and elastically supported beams. The finite element method is used to calculate the strain integrals as discussed in Chapter 4. The mechanical input parameters into the theoretical calculation are: the beam moduli, the foundation stiffness, the applied load and the strain transfer to the fiber. The strain transfer between the fiber and the surface of the beam depends on the thickness and shear modulus of the attachment material.

To calculate the phase change, the fiber material parameters, the optical and elasto-optical parameters, the servo and interferometer gains are needed. The sensor output depends on the relationship between the applied voltage to the phase transducer (PZT cylinder) and the corresponding fiber path length change.

Sirkis and Haslach (1990) have shown that for surface mounted optical fibers, the strain transfer, the elasto-optical parameters and the electronic parameters are not known

and need to be calibrated. Calibration of both the elastic, optical and electronic parameters are done for one experiment by fitting the undamaged elastically supported beam experimental results to the theoretical curve. It must be noted that for the elastically supported beam, the only two parameters needed are the ratio of beam to foundation stiffness and a linear scaling factor which takes into account all other parameters. The relative foundation stiffness is fitted using the shape of the curve for an undamaged elastically supported beam. The calibration of the elastic, optical and servo parameters is done by curve fitting the magnitude of the servo output. Calibration for the simply supported beam needs only one linear scaling factor.

6.6.1 *Elastically supported beam*

The elastically supported beam is tested by using a modulated load with peak-to-peak magnitude of 20N and frequency 5 Hz for 30 cycles at discrete locations. After the data is acquired, the servo-output is bandpass filtered at 5 Hz using a standard 4th order elliptic filter with a band-pass between 4.9 and 5.1 Hz (see MATLAB Signal Processing Toolbox for a description of the filtering technique).

Figure 6.9 shows the calibration fit between the theoretical and experimental results. The theoretical and experimental results are compared in Figure 6.10(a) to (c). Figure 6.10(a) shows some typical features of the phase-change plots. The definitions of the amplitude (A) and sidewidth (W) are the same as in Chapter 4. In Figure 6.9, a 0.1 change in scaled $\Delta\phi$ corresponds to a total phase change of 0.4 rads. The error bands correspond to the same test repeated 10 times

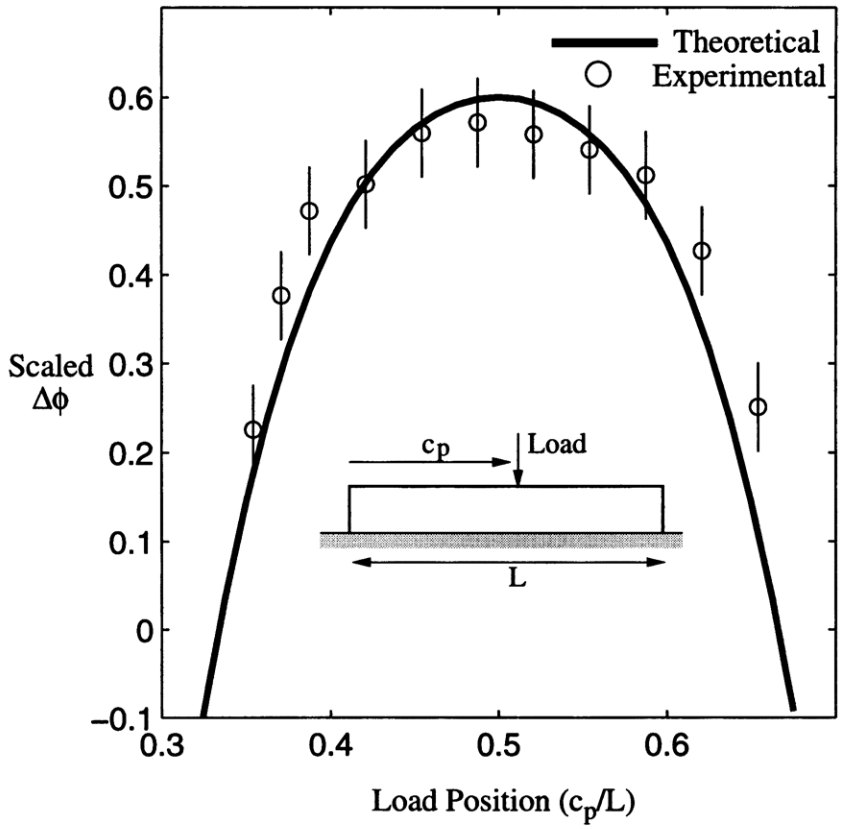

Figure 6.9: Calibration of experimental and theoretical results for an undamaged elastically supported beam. c_p is the load position, L is the length of the beam.

Once the scaling factor is obtained from the undamaged beam, experimental data for the damaged beam can be compared with theoretical results. For all cases, experimental and theoretical results show good agreement. The experiments show the typical features predicted by the theory, namely: (1) the axial position of the amplitude (A) correspond to the centre of the damaged zone, (2) as the crack length decreases the phase change amplitude decreases, and (3) the side-band width (W) corresponds to the damage length. In order to discern the salient features (such as amplitude and side-band width) of the various phase change signals, phase changes of the order of 0.05 rads need to be measured.

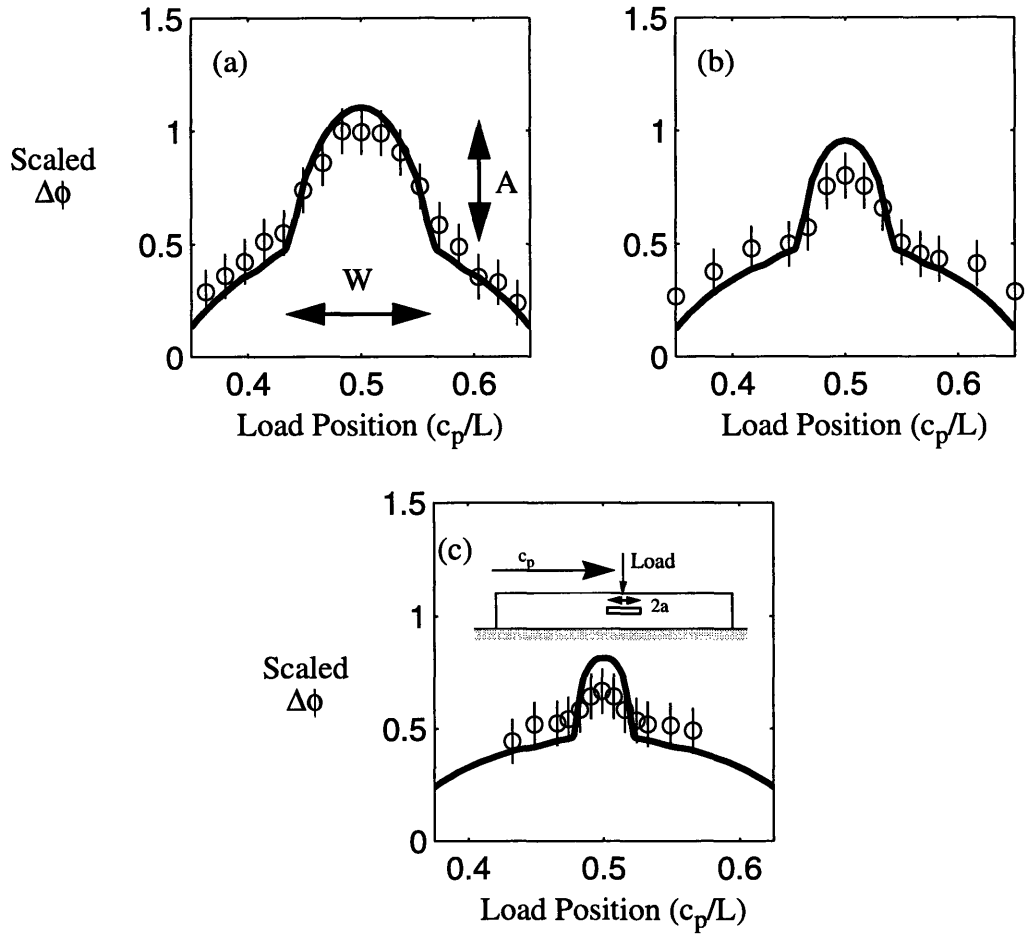

Figure 6.10: Comparison of theoretical and experimental results for three damage lengths. (a) *2a/L = 3/20*, (b) *2a/L=1/10* (c) *2a/L=1/20*, where *2a* is the length of the damage zone.

6.6.2 *Simply supported beam*

The simply supported beam is tested by driving the test cart at 0.2 m/s corresponding to a 2 second test, The experimental results for the simply supported beams are shown in Figure 6.11. This figure shows fluctuations when the load is over the support for all damage lengths (including the undamaged case). The error bands correspond to the maximum and minimum scatter for the same test performed 10 times. This fluctuation can be attributed to the start-up dynamics of the moving load. In order to remove the start-up dynamics from the signals in Figure 6.11, the undamaged signal is subtracted from the damage signals as shown in Figure 6.12. The experimental results of Figure 6.12 show good agreement with the theoretical results shown in Figure 6.13. As in the simply supported case, the axial position and damage lengths can be predicted from a simple moving load test. In Figures 6.9 and 6.10, a 0.1 change in $\Delta\phi$ corresponds to a phase change of 0.04 rads. For accurate assessment of the amplitude and bandwidth of the signals shown in Figure 6.12, differential phase change measurements of 0.005 rads need to be measured.

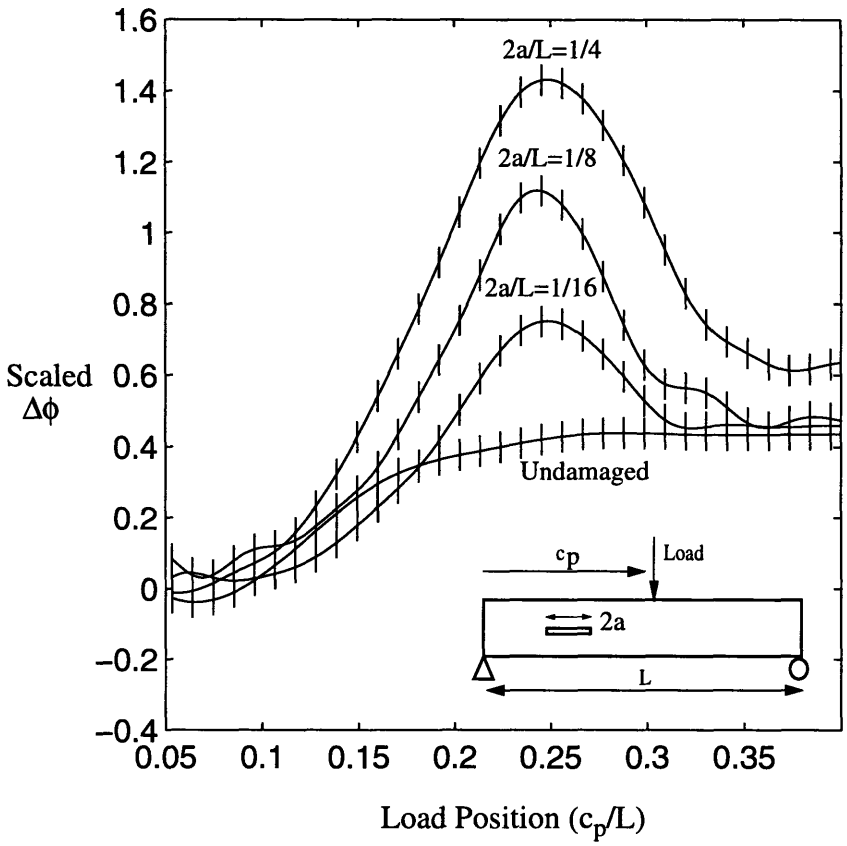

Figure 6.11: Experimental results for simply supported damaged beams subjected to a moving load. The damage position is at beam mid-depth and quarter span.

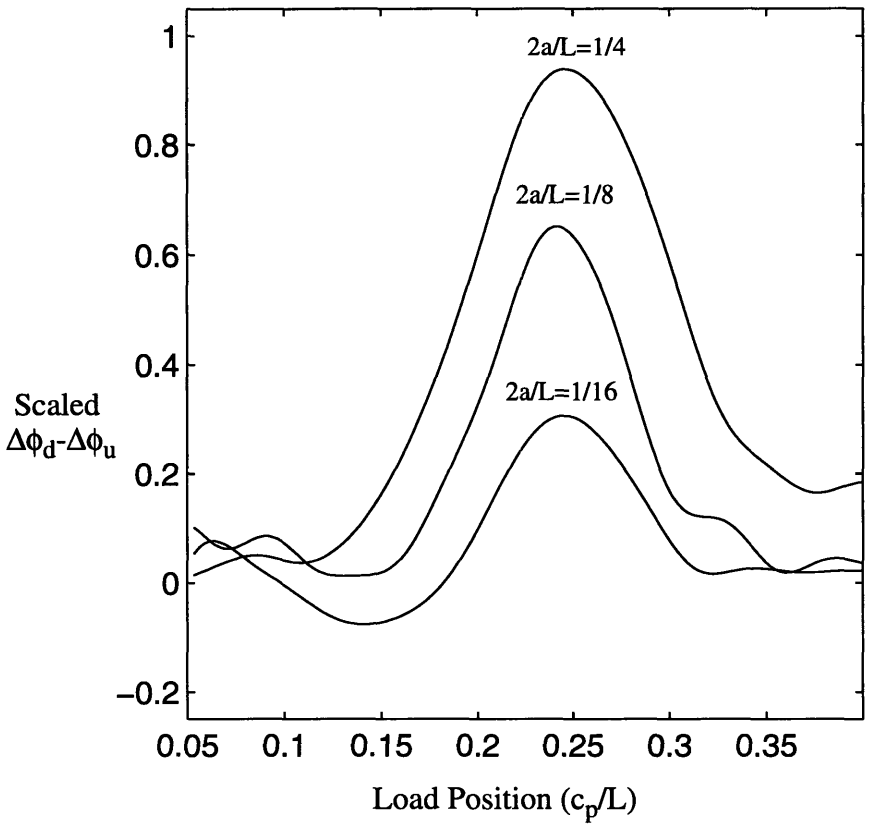

Figure 6.12: Experimental results for simply supported damaged beams subjected to a moving load. The undamaged phase change ($\Delta\phi_u$) is subtracted from the damaged phase change ($\Delta\phi_d$).

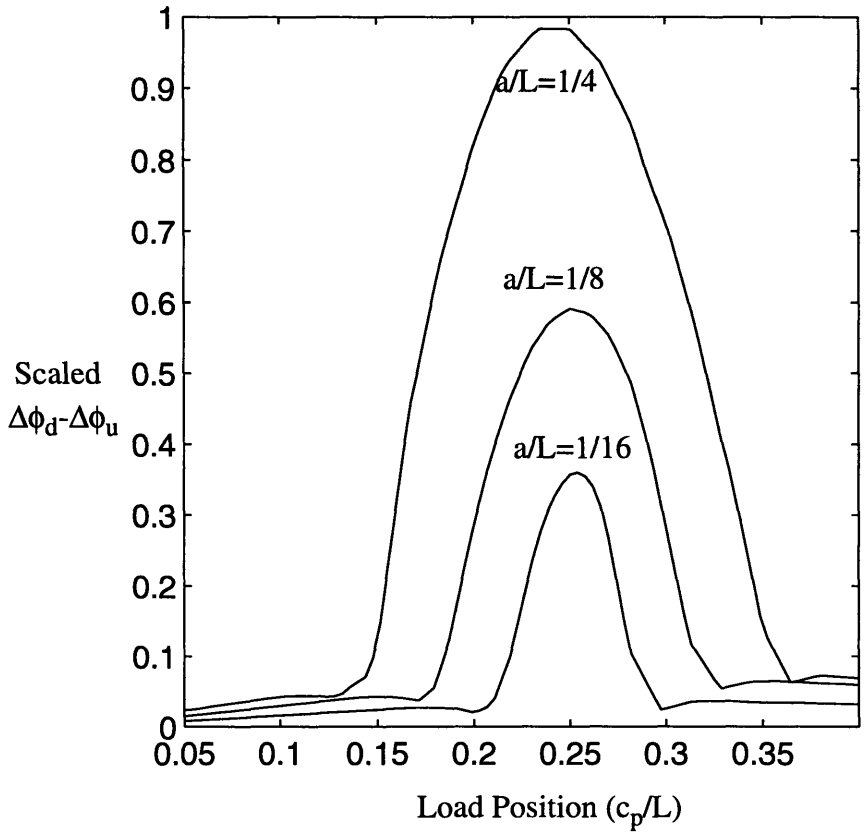

Figure 6.13: Theoretical results for damaged simply supported beams subjected to a moving load.

6.7 Discussion on the Results for Open Damage in a Model Beam

The experimental results on model beams presented in this chapter show that a closed-loop load-modulated interferometer can be used to measure the effect of subsurface damage on simply supported and elastically supported beams. This chapter has also shown that the required phase change sensitivity of 0.005 rads is needed for accurate location of damage. In both the simply supported and elastically supported beams, the size of the delamination zone can be garnered by comparing the amplitude and bandwidth of the phase-change signal difference of a damaged and undamaged beam. The location of the damage can be obtained by locating the position of the peak in the phase change signal.

The experimental results show that in order to obtain signals which do not have large drift components, the loading can be achieved either by (1) point-wise excitation at frequencies larger than 5 Hz (see Figure 6.3), or (2) by a moving load test. In order for the signal not to be corrupted by large drift components in the moving load test, the test should be completed faster than the drift rate. In the case when this is not possible, several tests need to be run so that the drift components can be averaged out. The disadvantage of the point-wise excitation scheme is that the test can become time consuming depending on the desired number of load positions. The practical aspects of using load modulation will be further discussed in Chapter 8.

Chapter 7

COMPARISON OF POINT SENSING VERSUS PROPOSED METHOD FOR DAMAGE DETECTION

A brief discussion of point sensing damage detection techniques (including Bragg Grating and Fabry-Perot sensors) was given in Chapter 2. Point sensing methods rely on measuring the strain perturbation caused by damage at a single point and then inferring the position and extent of damage from this measurement. This section discusses some implications of point-sensing to real-world damage detection, and compares current point sensing techniques with the novel damage sensing method.

Assume a 2-dimensional plane strain structure (such as a cantilever beam shown in Figure 6.1) loaded by a point load at its free end. The presence of any damage (shown as an open rectangular defect at beam mid-span and mid-height) will cause a perturbation to the undamaged strain field. The principle behind point-wise strain measurement is to determine the position and extent of damage in the structure with a grid of point sensors. This section attempts to ascertain the number of point-sensors that are needed in order to insure that the damage position is accurately determined.

As mentioned in Chapters 5, the measurement of strain is greatly influenced by the global behavior of the structure. For demonstration purposes, the following assumptions are made in this section: (i) the point sensor only measures axial strain, (ii) a 1% strain perturbation is needed in order to accurately resolve the strain from the global behavior of the structure, and (iii) the damage is open. The cantilever case is used as a demonstration example.

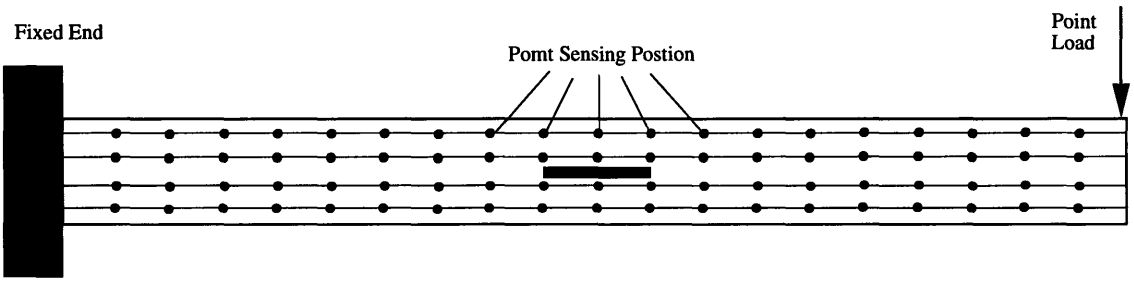

Figure 7.1: Schematic representation of a damage cantilever beam with a grid of point sensing positions

In this analysis, we assume that at least 4 point sensors have to show a perturbation of 1% (or greater) in order to accurately ascertain both the position and extent of damage. The iterative boundary element method described in Chapter 5 is used with 100 quadratic boundary elements on the beam and 20 quadratic boundary elements on the rectangular damage. The damage size is assumed to be $2a=L/10$, the length to height ratio of the rectangular damage is 1/10. Since the beam is elastic and we are considering only relative strain perturbations between damaged and undamaged structures, the results can be scaled

by applied load and elastic modulus. Figure 7.2 shows a simplified axial strain perturbation plot (in percentage deviation from the undamaged state) for the cantilever case.

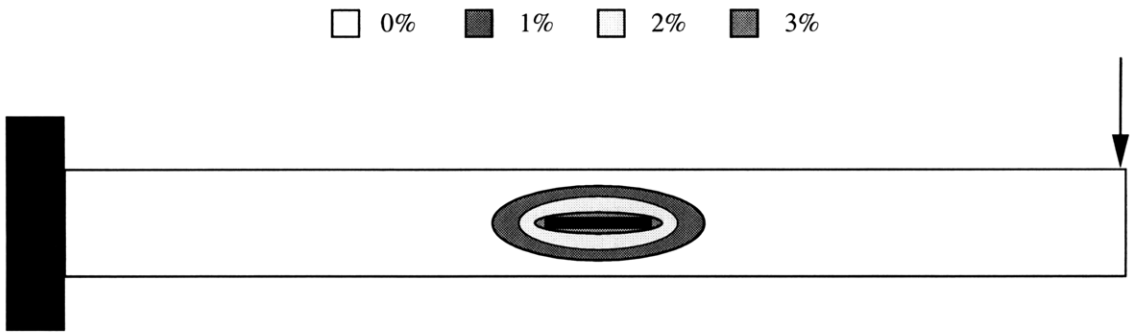

Figure 7.2: Relative strain perturbation between damaged and undamaged beam.

Figure 7.2 shows that the strain perturbation area is relatively localized around the damaged area. Performing the same analysis for different damage lengths and damage locations shows that on average, a 1% strain perturbation occurs in an area of $1.5\text{x}(2a)^2$

Assuming the position of the damage is not known *a-priori*, and that it can occur in any position within the beam, the number of sensors that are needed to accurately determine the location and position of the damage is given by
(Area of Structure x Number of Sensors to Locate Damage)/(1% Strain Perturbation Area) or

$$\frac{n_s 2hL}{1.5(2a)^2} \approx 5 \times \frac{hL}{(2a)^2} \tag{7.1}$$

where n_s is the number of sensors within the damage zone that is needed to accurately locate the damage size and position, which is assumed to be 4 in this analysis.

For example in a civil engineering bridge beam, of span L=100ft and depth 2h=5ft, 1300 point sensors per bridge span are needed to accurately locate a damage length of 1 ft, having assumed a 2-dimensional structure.

As an example of point sensing in an advanced composite, the 15.2 cm long glass fiber/epoxy composite four ply unidirectional laminated plate presented by Jian et al. 1997 is studied. Since advanced composite plates tend to be thin relative to their length, and the size of the damage is typically an order of magnitude greater than the laminate thickness, we assume that only 1 fiber is placed in the thickness direction of the laminate. In this case in order to detect a delamination of the order of 1 cm, approximately 40 point sensors in 2 dimensions are needed to locate a 1 cm long delamination. (It must be noted that the anisotropic behavior of the plate is ignored in this study and should be included in a more rigorous calculation).

This simplified analysis shows that a relatively large number of point sensors are needed to accurately detect the position and location of damage. The problem with moni-

toring and meaningful interpretation of the data from so many point sensors is an ongoing focus of many research efforts (Culshaw et al., 1998).

In contrast to the point sensing method, the novel integrated sensing method described in this thesis would require no more than 4 sensors in two dimensions (for redundancy) to monitor the entire structure (see Chapter 4 for open crack examples). Furthermore equation 7.1 shows that the number of sensors is scaled by structure length i.e. more sensors are needed for longer structures while the novel sensing technique is length invariant i.e. the number of sensors does not change with length scale.

Chapter 8

PRACTICAL ASPECTS OF OPTICAL FIBER SUBSURFACE DAMAGE DETECTION

8.1 Parametric Study of Method Sensitivity

This section studies some of the parameters that can influence sensor performance. Unlike point sensing methods such as the Bragg grating method, the closed loop load-modulated interferometer's resolution is dictated by the photon shot noise limit of the sensor discussed in Section 3.6 which is approximately $\delta(\Delta\phi) \approx 5\times10^{-7}$ rad . Chapters 4, 5 and 6 have also shown that without special data interpretation (such as differentiating the phase change output discussed in Section 5.7) the sensor output is dominated by the global bending effects of the structure. The global bending effects can produce outputs 1000 times greater than perturbations caused by damage. Two methods (the bridged fiber shown in Figure 6.8 and the $\Delta\phi$" method discussed in Section 5.7) have been proposed to resolve the phase perturbation caused by the damage from the global bending effect. For demonstration purposes, only the influence of sensor position uncertainties on the $\Delta\phi$" measurement technique for open damage is studied in this section.

8.1.1 *Sources of Measurement Uncertainty*

Various sources of uncertainty can influence the performance of the sensor. These can include (i) the uncertainty of the applied load magnitude and position, (ii) the structural configuration including structural dimensions and variations in elastic properties, (iii) the position of the sensor, (iv) the consistency of the attachment of the sensor to the structure, and (v) noise in the measurement system. It must be noted that some of the typical noise sources (assuming them to be random) such as the noise in the measurement system can be averaged out over multiple tests. Other uncertainties such as sensor position and beam properties are constant and can lead to erroneous interpretation of damage position and extent.

It can be noted that without any sources of uncertaintity, the resolution of the modulated interferometer which is theoretically governed by shot noise ($\delta(\Delta\phi) \approx 5x10^{-7}$ rads), is practically governed by environmental drift effects ($\delta(\Delta\phi) \approx 1x10^{-4}$ rads at 5 Hz). For demonstration purposes, consider a 200 mm long, 20 mm deep, cantilever beam with elastic modulus = 70 GPa, Poisson's ratio = 0.3, subjected to a moving point load. The optical properties are the same as described in Section 4.6 and the sensor is assumed to be surface mounted, The beam is assumed to have open damage at its mid-depth and mid-length. A moving load equal to 4.5 kN (corresponding to a maximum strain of 200 $\mu\varepsilon$) is applied to the structure. For adequate resolution of the damage, let it be assumed that the environmental drift effect at 5Hz load modulation is $\delta(\Delta\phi) \approx 1x10^{-4}$ rads and that in order to

resolve the damage a maximum phase perturbation due to the damage is $1x10^{-2}$ rads is required. Calculations for this case shows that the smallest damage length that has a phase change greater than $1x10^{-2}$ rads is approximately 2 mm (i.e. 1/10 of the beam height). It must be noted that increasing the modulating frequency would further decrease the environmental effects up to the shot noise limit of the interferometer, and would allow for increased resolution.

8.1.2 *Uncertainty Analysis*

Assume the mean sensor position to be placed at position (s_m) above the neutral axis, with a s_p uniform harmonic spacial fluctuation as shown in Figure 8.1(a) for maximum s_p=1%. The $\Delta\phi$" sensor output for a virgin simply supported beam as studied in section 5.8 is then given by Equation 5.34 with $s=s_m+s_p$ and $s_m=0.6h$ as shown in Figure 8.1(b).

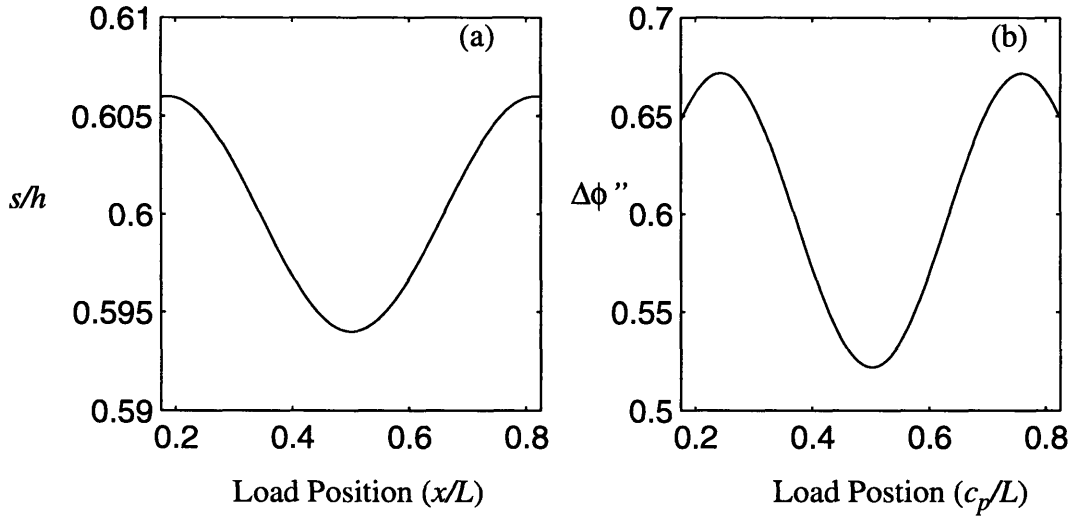

Figure 8.1: (a) A 1% random fluctuation in sensor position, and (b) the corresponding sensor output $\Delta\phi$" for a virgin beam

Differentiation of equation 5.34 with respect to load position includes differentiation of the sensor position variables (s) and beam properties (EI) and can lead to erroneous sensor output. The output of the sensor is strongly dependent on the actual axial variation of the sensor position. Figures 7.4 (a2, b2 and c2), show the output of the sensor to open damage for the simply supported beam that was studied in Section 5.8 for various sensor position distributions as shown in Figures 7.4 (a1, b1 and c1).

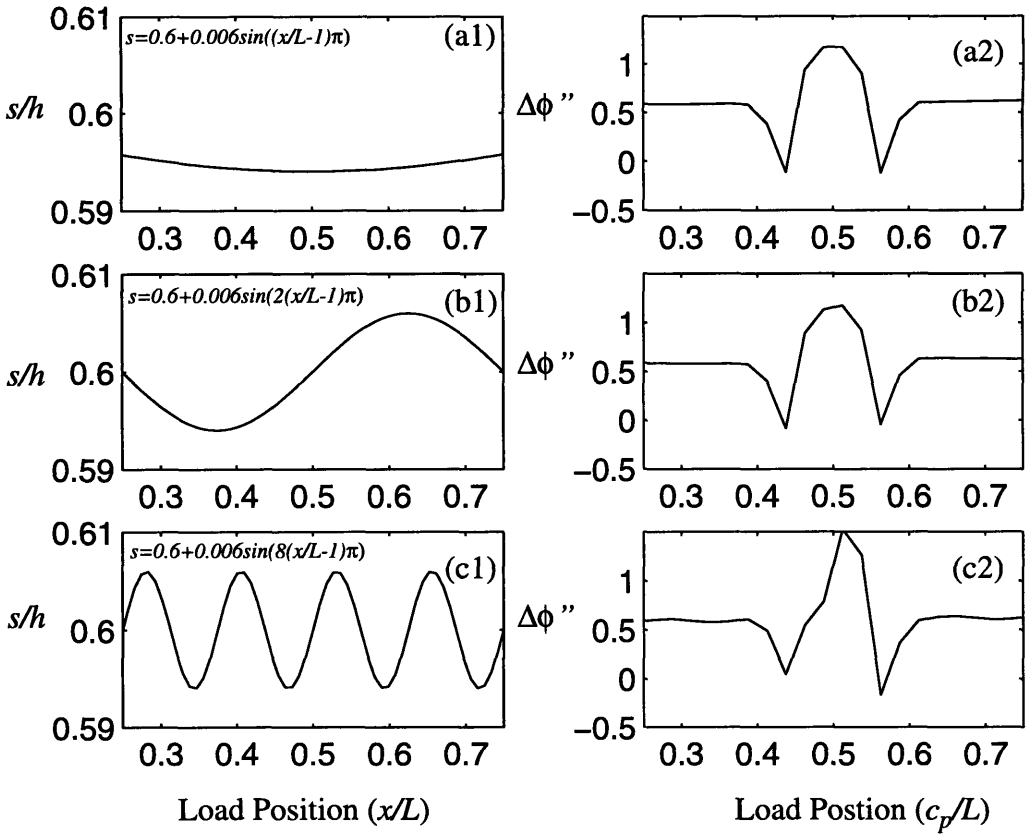

Figure 8.2: (a1, b1, and c1) Various sensor shape variations, and (a2, b2, and c2) $\Delta\phi$" sensor output for corresponding sensor input.

Figure 8.3 shows the $\Delta\phi$" sensor output for the case shown in Figure 8.2(a) but with a 10% amplitude variation in sensor position. Figure 7.5 shows that the position of the damage can still be determined but even with a 10% misalignment of the fiber. Figure 8.2 and 8.3 show that the sensor output is depended on both the transverse shape variation of the sensor position and the actual amplitude of the variation. For practical purposes this means that in order to avoid misinterpretation of the sensor output, the optical fiber should be kept as straight as possible during attachment (either when surface mounted or embedded) to the structure.

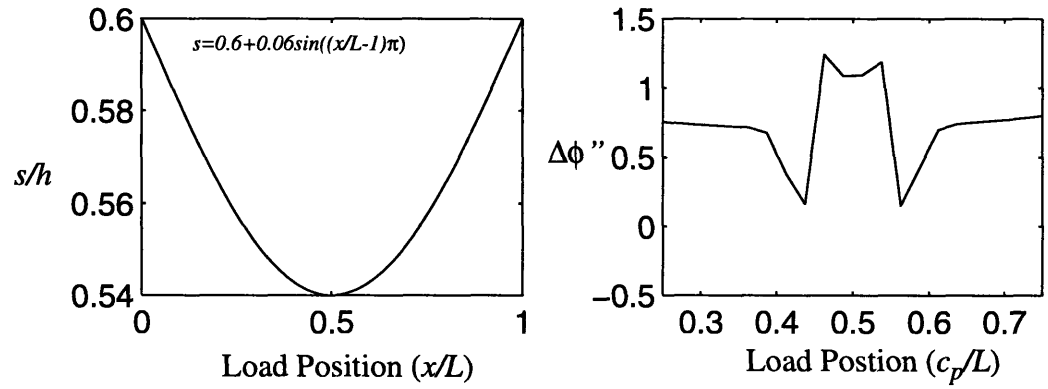

Figure 8.3: $\Delta\phi$" Sensor output for a 10% variation in sensor position (s)

8.2 Mechanical Load Application

For the testing of practical structures, the method of load application is dependent on (1) the type of structure being tested, (2) the length of the tested member, (3) the environmental conditions during testing, (3) the available equipment for load modulation.

In general, the loading frequency and magnitude has to be significantly high to allow for only small errors to be introduced into the measurement from environmental effects. This can be achieved either through load modulation of by moving the load at sufficiently high speeds thus allowing for only small environmental drifts during the testing period. For long structures such as bridges, the testing speed might not be great enough to overcome the environmental drift effects and load modulation might be applicable. For shorter structures such as composite wings, the moving load method might be suitable. In both the moving load and load modulation cases, care must be taken so as to not dynamically excite the structure which may produce erroneous signals in the sensor output. The frequency and magnitude of the load modulation is dependent on the mechanical actuator which provides the load modulation. For example unbalanced rotating machinery might be able to provide relatively high frequencies with relatively low magnitudes while pneumatic actuators can provide large loads at lower frequencies. The designer of the novel fiber-optic technique has to select the correct actuator frequency and load magnitude for the particular structure and environmental conditions under which the structure will be tested.

8.3 Conclusion

This section has shown that the damage resolution ability of the sensor depends on the environmental drift at the modulating load frequency, and on the production control during beam manufacturing (including beam dimensions, material consistency and sensor position). This section has also discussed some practical implications of load application.

Chapter 9

SUMMARY AND FUTURE WORK

9.1 Summary

The work presented in this thesis has concentrated on the development of a novel distributed fiber optic based sensing technique which can unambiguously identify both the location and extent of subsurface structural damage. Theoretical and experimental validation of the proposed method has been presented for the case of open cracks. The focus of this thesis has been on the characterization of the effect of damage position and damage size on sensor performance. The traditional problems of environmentally induced drift associated with all sensors has been overcome through modulated mechanical actuation. Due to the high resolution of phase change detection required by this technique, a closed loop interferometer has been shown to be one of the few viable sensors for distributed damage detection.

The theoretical feasibility of detecting closed cracks by the novel damage detection method is also presented. A computationally efficient iterative boundary element method has been developed for the solution of closed crack problems. This numerical method has been used to characterize the sensitivity of the detection method in locating closed cracks.

Some practical aspects of damage detection such as resolution issues and sources of uncertainties have also been addressed.

9.2 Original Contributions

Several original contributions have been made both in the study of damage and the detection thereof. These contributions include:

(1) The development of a novel integrated interferometric technique for subsurface damage detection. The method relies on monitoring the output of a closed loop interferometer, which measures integrated strains along the whole length of the structure, as a load is moved across the tested component. The method has been shown to accurately and unambiguously predict the extent and location of damage.

(2) The theoretical characterization of the sensor performance to the detection of open and closed subsurface damage of various locations and extent. Theoretical sensor outputs have been calculated for various damage positions, lengths and crack face contact conditions.

(3) The practical incorporation of a sensitive load modulated closed-loop integrated fiber-optic technique for sub-surface damage detection. Experiments performed on open damage beams (both simply and elastically supported) have shown that this novel sensing method can predict the extent and location of damage. A load modulation scheme has been shown to overcome the environmental drift (such as those caused by temperature) in the sensor.

(4) The development of a new efficient iterative boundary element method for the solution of closed crack problems. The method relies on separating the cracked-body problem into two sub-problems. The first sub-problem consisting of the body without the crack, the second sub-problem consisting of the crack in an infinite domain. The two sub-problems are linked through iteration until all boundary conditions of both sub-problems have been satisfied. The new iterative boundary element method has been shown to be on the order of 10 times faster in solving contact problems than the traditional displacement discontinuity boundary element method.

(5) A comparison of the novel technique with traditional point sensing techniques. This comparison shows that the for traditional point sensing techniques to be successful in locating the position and extent of damage, the whole length and height of the tested structure would need to be instrumented. The novel integrated fiber-optic technique allows for damage detections at any position along the fiber and thus significantly reduces the number of sensors needed for damage monitoring.

9.3 Future Work

Realistic subsurface damage in structures tends to occur in relative geometrically complicated three dimensional patches. Subsurface delamination damage is also typical for multi-layer composite structures.

Future theoretical feasibility studies should concentrate on (1) developing models to accurately assess delamination patches in three dimensions, and (2) the study of damaged layered anisotropic materials. The new iterative boundary element method described in Chapter 5 can be readily extended to include the analysis of three dimensional structures. Dislocation density functions have been found for 3-D structures and near 3-D interfaces for different materials (Hills et al. 1996) . Dislocation density function have also been recently found for general layered two dimensional anisotropic materials (Blanco et al. 1995). The problem with the dislocation density and displacement discontinuity methods for layered 3-dimensional anisotropic material is that the influence functions become very complicated. The general method of solving layered 3-dimensional anisotropic material problems is in the FEM framework (see for example the work of Choi and Chang, 1992 that deals with delamination damage in 3-dimensional graphite epoxy plates). As previously stated the problem with the FEM is that the whole domain needs to be discritized and this solutions tend to be slow. It is possible to extend the iterative method discussed in Chapter 5 to solve the global structural problem independently of the crack problem which could lead to considerable improvements in solution speeds since the global problem could be coarsely discritized.

The experimental validation of the proposed sensing method should concentrate on (1) the study of composite materials with typical delamination damage, and (2) the experimental validation of the theoretical results for closed cracks. Experimentally delaminations have been introduced into composites in a variety of ways including (1) low velocity impact (Choi and Chang, 1992), (2) static induced damage (Beard and Chang, 1997), and (3) the inclusion of teflon tape or silicon grease between layers to simulate delaminations (see for example Jian et al. 1997). The problems with the impact and static damage meth-

ods is that the induced damage typically occurs in complicated 3-dimensional geometries which is difficult to categorize and to include into a theoretical model. The problem with the inclusion (teflon for example) is that the formed voids tend to be open which is not characteristic of real delaminations. One experimental method to introduce simplified delaminations into composite structures is to use the silicon grease inclusion method and to apply a static pressure to the structure in order to cause the crack to close.

Appendix A

Quadratic Displacement Discontinuity Influence Functions

The displacement and stresses at a point (x_i, y_i) due to a quadratic displacement discontinuity centered at (xj,yj) with length $(-a,a)$ and nodes at $[-B;0;B]$ where $B=b*a$; are derived from Battacharyya and Wilment (1988) and are given by:

$U_x(x_j,y_j) = {}^{ij}B_{1xx}D_x(-B)+{}^{ij}B_{2xx}D_x(0)+{}^{ij}B_{3xx}(B)+{}^{ij}B_{1xy}D_y(-B)+{}^{ij}B_{2xy}D_y(0)+{}^{ij}B_{3xy}(B)$
$U_y(x_j,y_j) = {}^{ij}B_{1yx}D_x(-B)+{}^{ij}B_{2yx}D_x(0)+{}^{ij}B_{3yx}(B)+{}^{ij}B_{1yy}D_y(-B)+{}^{ij}B_{2yy}D_y(0)+{}^{ij}B_{3yy}(B)$

${}^{ij}B_{1xx}=1/2/B^2(-(3-2\nu)(2x-B)yf_2+(2(1-\nu)x(x-B)-2(2-\nu)y^2)f_3-(2x-B)y^2f_4-(x(x-B)-y^2)yf_5-(3-2\nu)ay/2/\pi/(1-\nu))$
${}^{ij}B_{1xy}=1/2/B^2((-(1-2\nu)x(x-B)+(3-2\nu)y^2)f_2-2(1-\nu)(2x-B)yf_3-(x^2-Bx-y^2)yf_4+(2x-B)y^2f_5-(1-2\nu)a(x-B)2k_1)$
${}^{ij}B_{1yx}=1/2/B^2(-(1-2\nu)(2x-B)yf_2+(2(1-\nu)x(x-B)+2\nu y^2)f_3+(2x-B)y^2f_4+(x(x-B)-y^2)yf_5-(1-2\nu)ay/2/\pi/(1-\nu))$
${}^{ij}B_{1yy}=1/2/B^2(((1-2\nu)x(x-B)+(1+2\nu)y^2)f_2-2\nu(2x-B)yf_3-(x(x-B)-y_2)yf_4+(2x-B)y^2f_5+(1-2\nu)a(x-B)/2/\pi/(1-\nu))$
${}^{ij}B_{2xx}=1/B^2(2(3-2\nu)xyf_2+(2(1-\nu)(B^2-x^2)+2(2-\nu)y^2)f_3+2xy2f_4+(x^2-B^2-y^2)yf_5+(3-2\nu)ay/2/\pi/(1-\nu))$
${}^{ij}B_{2xy}=1/B^2(((1-2\nu)(x^2-B^2)-(3-2\nu)y^2)f_2+4(1-\nu)xyf_3+(x^2-B^2-y^2)yf_4-2xy^2f_5+(1-2\nu)ax/2/\pi/(1-\nu))$
${}^{ij}B_{2yx}=1/B^2(((1-2\nu)(B^2-x^2)-(1+2\nu)y^2)f_2+4\nu xyf_3+(x^2-B^2-y^2)yf_4-2xy^2f_5-(1-2\nu)ax/2/\pi/(1-\nu))$
${}^{ij}B_{2yy}=1/B^2(2(1-2\nu)xyf_2+(2(1-\nu)(B_2-x_2)-2\nu y^2)f_3-2xy^2f_4-(x^2-B^2-y^2)yf_5+(1-2\nu)ay/2/\pi/(1-\nu))$
${}^{ij}B_{3xx}=1/2/B^2(-(3-2\nu)(2x+B)yf_2+(2(1-\nu)x(x+B)-2(2-n)y^2)f_3-(2x+B)y^2f_4-(x(x+B)-y^2)yf_5-(3-2\nu)ay/2/\pi/(1-\nu))$
${}^{ij}B_{3xy}=1/2/B^2((-(1-2\nu)x(x+B)+(3-2\nu)y^2)f_2-2(1-\nu)(2x+B)yf_3-x^2+Bxy^2)yf_4+(2x+B)y^2f_5-(1-2\nu)a(x+B)/2/\pi/(1-\nu))$
${}^{ij}B_{3yx}=1/2/B^2(((1-2\nu)x(x+B)+(1+2\nu)y^2)f_2-2\nu(2x+B)yf_3-(x(x+B)-y^2)yf_4+(2x+B)y^2f_5+(1-2\nu)a(x+B)/2/\pi/(1-\nu))$
${}^{ij}B_{3yy}=1/2/B^2(-(1-2\nu)(2x+B)yf_2+(2(1-\nu)x(x+B)+2\nu y^2)f_3+(2x+B)y^2f_4+(x(x+B)-y^2)yf5-(1-2\nu)ay/2/\pi/(1-\nu))$

$\sigma_x(x_j,y_j) = {}^{ij}A_{1xx}D_x(-B)+{}^{ij}A_{2xx}D_x(0)+{}^{ij}A_{3xx}(B)+{}^{ij}A_{1xy}D_y(-B)+{}^{ij}A_{2xy}D_y(0)+{}^{ij}A_{3xy}(B)$
$\sigma_y(x_j,y_j) = {}^{ij}A_{1yx}D_x(-B)+{}^{ij}A_{2yx}D_x(0)+{}^{ij}A_{3yx}(B)+{}^{ij}A_{1yy}D_y(-B)+{}^{ij}A_{2yy}D_y(0)+{}^{ij}A_{3yy}(B)$
$\sigma_{xy}(x_j,y_j) = {}^{ij}A_{1xyx}D_x(-B)+{}^{ij}A_{2xyx}D_x(0)+{}^{ij}A_{3xyx}(B)+{}^{ij}A_{1xyy}D_y(-B)+{}^{ij}A_{2xyy}D_y(0)+{}^{ij}A_{3xyy}(B)$

${}^{ij}AA_{1xx}=G/B^2(-6yf_2+2(2x-B)f_3+2(x(x-B)-3y^2)f_4-4(2x-B)yf_5+(x(x-B)-y^2)yf_6+(2x-B)y^2f_7)$
${}^{ij}A_{1xy}=G/B^2(-(2x-B)f_2-4yf_3-3(2x-B)yf_4-(x(x-B)-5y^2)f_5-(2x-B)y^2f_6+(x(x-B)-y^2)yf_7-a/\pi/(1-\nu)/2)$
${}^{ij}A_{1yx}= G/B^2(2yf_2+4y^2f4+2(2x-B)yf_5-(x(x-B)-y^2)yf_6-(2x-B)y^2f_7)$
${}^{ij}A_{1yy}=G/B^2(-(2x-B)f2+(2x-B)yf4-(x(x-B)+3y^2)f_5+(2x-B)y^2f_6-(x(x-B)-y^2)yf_7-a/\pi/(1-\nu)/2)$
${}^{ij}A_{1xyx}=G/B^2(-(2x-B)f_2-4yf_3-3(2x-B)yf_4-(x(x-B)-5y^2)f_5-(2x-B)y^2f_6+((x(x-B)-y^2))yf_7-a/\pi/(1-\nu)/2)$
${}^{ij}A_{1xyy}=G/B^2(2yf_2+4y^2f_4+2(2x-B)yf_5-(x(x-B)-y^2)yf_6-(2x-B)y^2f_7)$
${}^{ij}AA_{2xx} = 2G/B^2(6yf_2-4xf_3-2(x^2-B^2-3y^2)f_4+8xyf_5-(x^2-B^2-y^2)yf6-2xy^2f_7)$
${}^{ij}AA_{2xy} = 2G/B^2(2xf_2+4yf_3+6xyf_4+(x^2-B^2-5y^2)f_5+2xy^2f_6-(x^2-B^2-y^2)yf_7+a/\pi\iota/(1-\nu\upsilon)/2);$
${}^{ij}AA_{2yx} = 2G/B^2(-2yf_2-4y^2f_4-4xyf_5+(x^2-B^2-y^2)yf_6+2xy^2f_7)$
${}^{ij}AA_{2yy}=2G/B^2(2xf_2-2xyf_4+(x^2-B^2+3y^2)f_5-2xy^2f_6+(x^2-B^2-y^2)yf_7+a/\pi\iota/(1-\nu\upsilon)/2)$
${}^{ij}AA_{2xyx}=2G/B^2(2xf_2+4yf_3+6xyf_4+(x^2-B^2-5y^2)f_5+2xy^2f_6-(x^2-B^2-y^2)yf_7+a/\pi\iota/(1-\nu\upsilon)/2);$
${}^{ij}AA_{2xyy}=2G/B^2(-2yf_2-4y^2f_4-4xyf_5+(x^2-B^2-y^2)yf_6+2xy^2f_7)$
${}^{ij}AA_{3xx}=G/B^2(-6yf_2+2(2x+B)f_3+2(x(x+B)-3y^2)f_4-4(2x+B)yf_5+(x(x+B)-y^2)yf_6+(2x+B)y^2f_7)$
${}^{ij}AA_{3xy}=G/B^2(-(2x+B)f_2-4yf_3-3(2x+B)yf_4-(x(x+B)-5y^2)f_5-(2x+B)y^2f_6+(x(x+B)-y^2)yf_7-a/\pi/(1-\nu)/2)$
${}^{ij}AA_{3yx}= G/B^2(2yf_2+4y^2f_4+2(2x+B)yf_5-(x(x+B)-y^2)yf_6-(2x+B)y^2f_7)$
${}^{ij}AA_{3yy}=G/B^2(-(2x+B)f_2+(2x+B)yf_4-(x(x+B)+3y^2)f_5+(2x+B)y^2f_6-(x(x+B)-y^2)yf_7-a/\pi/(1-\nu)/2)$
${}^{ij}AA_{3xyx}=G/B^2(-(2x+B)f_2-4yf_3-3(2x+B)yf_4-(x(x+B)-5y^2)f_5-(2x+B)y^2f_6+((x(x+B)-y^2))yf_7-a/\pi/(1-\nu)/2)$
${}^{ij}AA_{3xyy} = G/B^2(2yf_2+4y^2f_4+2(2x+B)yf_5-(x(x+B)-y^2)yf_6-(2x+B)y^2f_7)$

where
$x=x_i-x_j$ and $y=y_i-y_j$
$k_1=1/\pi/(1-\nu)/4;$
$f_2=k_1(\log(r_1)-\log(r_2))$
$f_3=-k_1(-\arctan((x-a)/y)+\arctan((x+a)/y))$
$f_4=k_1(y/r_1\text{^}2-y/r2\text{^}2)$
$f_5=k_1((x-a)/r_1^2-(x+a)/r_2^2)$
$f_6=k_1(((x-a)^2-y^2)/r_1^4-((x+a)^2-y^2)/r_2^4)$
$f_7=2yk_1((x-a)/r_1^4-(x+a)/r_2^4)$

$r1=((x-a)^2+y^2)^{0.5}$ and $r2=((x+a)^2+y^2)^{0.5}$

Appendix B

Dislocation Influence Coefficients

The stress and displacement influence coefficients in Equations 4.6 to 4.9 are given by

$$G_{xxx} = \frac{-\bar{y}}{r^4}(3\bar{x}^2 + \bar{y}^2) \tag{B.1}$$

$$G_{yxx} = \frac{\bar{x}}{r^4}(\bar{x}^2 - \bar{y}^2) \tag{B.2}$$

$$G_{xyy} = \frac{\bar{y}}{r^4}(\bar{x}^2 - \bar{y}^2) \tag{B.3}$$

$$G_{yyy} = \frac{\bar{x}}{r^4}(\bar{x}^2 + 3\bar{y}^2) \tag{B.4}$$

$$G_{xxy} = \frac{\bar{x}}{r^4}(\bar{x}^2 - \bar{y}^2) \tag{B.5}$$

$$G_{yxy} = \frac{\bar{y}}{r^4}(\bar{x}^2 - \bar{y}^2) \tag{B.6}$$

$$U_{xx} = (\kappa + 1)\Theta + \frac{2\bar{x}\bar{y}}{r^2} \tag{B.7}$$

$$U_{xy} = -(\kappa - 1)\log r - \frac{2\bar{x}^2}{r^2} \tag{B.8}$$

$$U_{yx} = -(1 - \kappa)\log r - \frac{2\bar{x}^2}{r^2} \tag{B.9}$$

$$U_{yy} = (\kappa + 1)\Theta - \frac{2\bar{x}\bar{y}}{r^2} \tag{B.10}$$

where $\bar{x} = x - x_d$, $\bar{y} = y - y_d$, $r^2 = (x - x_d)^2 + (y - y_d)^2$ and Θ is the angle shown in Figure 5.3.

REFERENCES

Ameen, M. and Raghuprasad B.K. 'Hybrid technique of modeling of cracks using displacement discontinuity and direct boundary element method', *International Journal of Fracture*, v.67, 343-355. (1994)

Arfken G. *Mathematical Methods for Physicists*, Academic Press Inc, Boston. (1985)

ASCE Key Alert - (1997) - http://www.asce.org/govnpub/issbrfdm.html

Bathe, K.J. *Finite Element Procedures*. Englewood Cliffs, Prentice-Hall, (1996)

Beard, S. and Chang F-K. 'Active damage detection in filament wound composite tubes using built-in sensors and actuators', *Journal of Intelligent Materials Systems and Structures*, v.8 pp891-895 (1997)

Bhattacharyya, P. K. and Willment, T. 'Quadratic approximations in the displacement discontinuity method', *Engineering Analysis*, v.5, 28-35. (1988)

Blanco C., Martinez-Esnaoloa J.M., Atkinson C. and Bastero J.M. 'Coating cracks in materials with general anisotropy', *International Journal of Fracture*, v.71, pp99-130 (1995)

Bray D. E. and Stanley R. K. *Nondestructive Testing - A Tool in Design Manufacturing and Service*. New York, CRC Press. (1997)

Blanford, G.E., Ingraffea, A.R. and Liggett, J.A. 'Two dimensional stress intensity factor computations using the boundary element method.' *International Journal of Numerical Methods in Engineering*, v.17, 387-404. (1981)

Butter C.D. and Hocker G.D. "Fiber Optic Strain Gage" *Applied Optics*, Vol.17, 2867-2869 (1978)

Cawley P. and Alleyne D. "The use of Lamb Waves for the Long Range Inspection of Large Structures" *Ultrasonics*, v.34, 287-290 (1996)

Chang C. C and Sirkis J.S. "Differential-Cross-Multiplier Demodulation of Interferometric Optical Fiber Sensors", *Experimental Techniques* v. 20 no. 3, 29-32 (1996)

Chang, F.K., Comninou, M., Sheppard, S., and Barber, J.R. 'The subsurface crack under conditions of slip and stick caused by a surface normal force.' *Journal of Applied Mechanics*, v.51, 311-316. (1984)

Choi H.Y. and Chang F-K. 'Model for predicting damage in graphite/epoxy laminated composites resulting from low-velocity point impact', *Journal of Composite Materials*, v.26. 2134-2169 (1992)

Cook A.H. *Interference of Electromagnetic Waves*, Claredon Press, Oxford, UK (1971)

Crouch, S.L. 'Solution of plane elasticity problems by the displacement discontinuity method. Part I. Infinite body solution, Part II. Semi-infinite body solution.' *International Journal of Numerical Methods in Engineering*, v.10, 301-343. (1976)

Crouch, S.L. 'Computer simulation of mining in faulted ground.' *Journal of the South African Institute of Mining and Metallurgy*, v.79, 159-173. (1979)

Crouch, S.L and Starfield A.M. *Boundary Element Methods in Solid Mechanics : with Applications in Rock Mechanics and Geological Engineering.* Boston: Alen & Unwin (1983)

Culshaw, B. and Udd, E., First International Workshop on Fiber Optic Sensors for Construction Materials and Bridges, personal communication, (1998).

Culshaw, B. *Optical Fibre Sensing and Signal Processing*, London UK, Peregrinus, (1984)

Desai, C.S. Elementary Finite Element Method. Englewood Cliffs, N.J., Prentice Hall. (1979)

Elvin N. and Leung C. "Feasibility Study of Delamination Detection with Embedded Optical Fibers." *Journal of Intel. Mat. Syst. and Structures*, v. 8, (1997) 824-828.

Ewalds, H.L. and Wanhill, R.J. *Fracture Mechanics*, Edward Arnold, Australia, (1986).

Ezekiel S. (ed) *Fiber Optic Gyros:* 15th Anniversary Conference: 4-6 September 1991, Boston, Massachusetts, SPIE (1992)

Ezekiel S. and Arditty H. J. "Fiber Optic Rotation Sensors: tutorial review" in *Fiber Optic Rotation Sensors and Related Technologies*, Springer Series in Optical Sciences v. 32, S. Ezekiel and H.J. Arditty (ed.) New York: Springer-Verlag. (1982)

Frieble, E.J. ,'Fiber Bragg Grating Strain Sensors: Present and future applications in smart structures.' *Optics and Photonics News,* August 1998 pp 33-37, (1998)

Fowles, G.F. *Introduction to Moden Optics.* Dover Publications Inc. New York (1975)

Hearle, A.D. and Johnson, K.L. 'Mode II stress intensity factors for a crack parallel to the surface of an elastic half-space subjected to a moving point load'. *Journal of the Mechanics and Physics of Solids.* v.33, 61-81. (1985)

Hills, D.A. et al. *Solution of Crack Problems: the Distributed Dislocation Technique.* Kluwer Academic Publishers, Boston, (1996).

Hung, Y.Y. "Shearography versus Holography in Nondestructive Evaluation" *Proceeding of SPIE - Volume 604 Holographic NonDestructive Testing.* Los Angeles, California, pp18-29 (1986)

Jackson D.A., "Monomode Optical Fibre Interferometers for Precision Measurements", *Journal of Physics E: Instruments.* v. 18 , 981-1001 (1985)

Jackson D. A., Priest R., Dandridge A. and Tveten A. B. "Elimination of Drift in Single-Mode Optical Fibre Interferometer Using a Piezoelectrically Stretched Coiled Fibre", *Applied Optics*, v.19, 2926-2929 (1980)

Jian X.H., Tzou H.S., Lissenden C.J. and Penn L.S. "Damage Detection by Piezoelectric Patches in a Free Vibration Method", *Journal of Composite Materials*, Vol. 31, 345-359

(1997)

Kaczmarek H. "Ultrasonic Detection of Damage in CRFPs" *Journal of Composite Materials,* Vol. 29, 59-95 (1995)

Komvopolous, K. 'Subsurface crack mechanisms under indentation loading.' *Wear*, v.199, 9-23. (1996)

Komvopoulos, K. and Cho, S.-S. 'Finite Element Analysis of Subsurface crack propagation in a half-space due to a moving asperity contact,' *Wear*, v.209, 57-68 (1997)

Kundu, T., Maji, A., Ghosh, T. and Maslov, K. 'Detection of kissing bonds by Lamb waves'. *Ultrasonics*, v.35 pp573-580 (1997)

Kuo B. C. *Automatic Control Systems*, Englewood Cliffs, N.J. : Prentice Hall, (1991)

Lahiri J., Siddalingaiah D.L., Kamaraguru P.P. and Reddy K.S. "Non-Destructive Evaluation of Delaminations and Voids in Axi-symmetric CFRP shells: Part A Scope and Limitation of X-ray Radiography" *Non-Destructive Testing '92.* C. Hallai and Kulcsar P. (Ed.), New York, Elsevier, 625-631 (1992)

LeCoeuche V., Fisher N.E., Pannel C.N., Webb D.J. and Jackson D.A. "Developments in Optical Techniques for Point and Distributed Sensing in Large Structures", in *Fiber Optic Sensors for Construction Materials and Bridges*, edited by F. Ansari, pp.65-88 (1998)

Lee, S. S. 'Complementarity problem formulation for the crack closure problem using the dual boundary element'. International Conference on Contact Mechanics. In *Proceedings of the 1997 3rd International Conference on Contact Mechanics*, 1997, 289-299.

Livingston, R.A."Federal Highway Administration Research Program in Fiber Optics for the Infrastructure" in *Fiber Optic Sensors for Construction Materials and Bridges*, edited by F. Ansari, pp.3-13 (1998)

MATLAB Singal Processing Toolbox, The Math Works. Inc. Natick, MA (1992)

Migliori A. and Darling T.W. "Resonant ultrasound spectroscopy for material studies and non-destructive testing" *Ultrasonics*, v. 34, 473-476 (1996)

Oppenheim A.V. *Discrete-Time Signal Processing*, Prentice Hall, Englewood Cliffs, N.J. (1989)

Parthasarathi, S., Aesoph, M.D., Sampath, K. and Tittmann, B.R. 'Thermal wave imaging and ultrasonic characterization of defects in plasma sprayed coatings' *Materials and Manufacturing Processes,* v.10, 1077-1086 (1995)

Saka M. and Abe H., 'Sizing closed cracks by ultrasonics and analysis', *Computational and Experimental Fracture Mechanics.* Nistani H. ed. 165 (1994)

Sirkis J.S. and H.W. Haslach H.W. "Interferometric strain measurement by arbitrarily configured, surface-mounted, optical fibers" *Journal of Lightwave Technology*, Vol.8, 1497-1503 (1990)

Sirkis, J.S. and Haslach H.W. 'Complete Phase-Strain Model for Structurally Embedded Interferometric Optical Fiber Sensor.' *Journal of Intelligent Material Systems and Structures* v.2, .3-24 (1991)

Sturt, A., Nowell, D. and Hills D.A. 'Application of the boundary element and dislocation density methods in plane crack problems', *Engineering Analysis with Boundary Element.*, v.11, 129-135 (1993)

Timoshenko S. *Strength of Materials Vol II.* Huntington, N.Y.: Krieger Pub. Co. (1976)

Tracy J.J., Pardoen G.C. "Effect of Delamination on the Natural Frequencies of Composite Laminates". *Journal of Composite Materials*, Vol. 23. 1200-1215. (1989)

Udd, E. *Fiber optic sensors : an introduction for engineers and scientists.* New York : Wiley (1992).

Ugural A.C. and Fenster S.K. *Advanced Strength and Applied Elasticity.* Englewood Cliffs, N.J. : PTR Prentice Hall, (1987)

Vest, C (ed.) *Proceeding of SPIE - Volume 604 Holographic NonDestructive Testing.* Los Angeles, California, pp18-29 (1986)

Vlasov V.Z. and Leontev U.N. 1960. *Beams, Plates and Shells on Elastic Foundations.* Jerusalem, Israel Program for Scientific Translations. (1960)

Yariv A. *Introduction to Optical Electronics*, Holt, Rinehart and Winston (1976)

Zhang, Daqing; Sandor, Bela I "Advances in thermographic stress analysis and evaluation of damage in composites " *ASTM Special Technical Publication 10th Conference on Composite Materials*, pp428-443, (1992)

Zhang, S., and Leech C.M., 'FEM analysis of mixed mode fracture of CSM-GRP.' *Engineering Fracture Mechanics.*, v.23, 521-535 (1986)